

1 LEVERAGING MULTI-MESSENGER ASTROPHYSICS FOR DARK MATTER SEARCHES

By

Daniel Nicholas Salazar-Gallegos

A DISSERTATION

Submitted to
Michigan State University
in partial fulfillment of the requirements
for the degree of

Physics—Doctor of Philosophy
Computational Mathematics in Science and Engineering—Dual Major

Today

ABSTRACT

3 I did Dark Matter with HAWC and IceCube. I also used Graph Neural Networks

⁴ Copyright by

⁵ DANIEL NICHOLAS SALAZAR-GALLEGOS

⁶ Today

ACKNOWLEDGMENTS

8 I love my friends. Thanks to everyone that helped me figure this out. Amazing thanks to the people
9 at LANL who supported me. Eames, etc Dinner Parties Jenny and her child Kaydince Kirsten, Pat,
10 Andrea Family. You're so far but so critical to my formation. Unconditional love. Roommate

TABLE OF CONTENTS

12	LIST OF TABLES	vii
13	LIST OF FIGURES	viii
14	LIST OF ABBREVIATIONS	xv
15	CHAPTER 1 INTRODUCTION	1
16	CHAPTER 2 DARK MATTER IN THE COSMOS	2
17	2.1 Introduction	2
18	2.2 Dark Matter Basics	3
19	2.3 Evidence for Dark Matter	4
20	2.4 Searching for Dark Matter: Particle DM	11
21	2.5 Sources for Indirect Dark Matter Searches	16
22	2.6 Multi-Messenger Dark Matter	18
23	CHAPTER 3 MULTIMESSENGER ASTROPHYSICS: DETECTING HIGH EN-	
24	ERGY NEUTRAL MESSENGERS	21
25	3.1 Introduction	21
26	3.2 Charged Particles in a Medium	21
27	3.3 Photons (γ)	22
28	3.4 Neutrinos (ν)	22
29	3.5 Opportunities to Combine for Dark Matter	22
30	CHAPTER 4 HIGH ALTITUDE WATER CHERENKOV (HAWC) OBSERVATORY .	24
31	4.1 The Detector	24
32	4.2 Events Reconstruction and Data Acquisition	24
33	4.3 Remote Monitoring	24
34	CHAPTER 5 ICECUBE NEUTRINO OBSERVATORY	25
35	5.1 The Detector	25
36	5.2 Events Reconstruction and Data Acquisition	25
37	5.3 Northern Test Site	25
38	CHAPTER 6 GLORY DUCK: MULTI-WAVELENGTH SEARCH FOR DARK MATT-	
39	TER ANNIHILATION TOWARDS DWARF SPHEROIDAL GALAX-	
40	IES	26
41	6.1 Introduction	26
42	6.2 Dataset and Background	28
43	6.3 Analysis	29
44	6.4 Likelihood Methods	34
45	6.5 HAWC Results	40
46	6.6 Glory Duck Combined Results	43
47	6.7 HAWC Systematics	48

48	6.8 <i>J</i> -factor distributions	49
49	6.9 Discussion and Conclusions	55
50	CHAPTER 7 MULTITHREADING HAWC ANALYSES FOR DARK MATTER	
51	SEARCHES	59
52	7.1 Introduction	59
53	7.2 Dataset and Background	59
54	7.3 Analysis	61
55	7.4 Likelihood Methods	64
56	7.5 Computational Methods: Multithreading	65
57	7.6 Analysis Results	71
58	7.7 Systematics	72
59	7.8 Conclusion and Discussion	73
60	CHAPTER 8 HEAVY DARK MATTER ANNIHILATION SEARCH WITH ICE-	
61	CUBE'S NORTH SKY TRACK DATA	79
62	CHAPTER 9 NU DUCK	80
63	APPENDIX A MULTI-EXPERIMENT SUPPLEMENTARY FIGURES	81
64	APPENDIX B MULTITHREADING SUPPLEMENTARY FIGURES	82
65	B.1 <code>mpu_analysis.py</code>	83
66	BIBLIOGRAPHY	92

LIST OF TABLES

<p>68 Table 6.1 Summary of the relevant properties of the dSphs used in the present work. 69 Column 1 lists the dSphs. Columns 2 and 3 present their heliocentric distance 70 and galactic coordinates, respectively. Columns 4 and 5 report the J-factors of 71 each source given from the \mathcal{GS} and \mathcal{B} independent studies and their estimated 72 $\pm 1\sigma$ uncertainties. The values $\log_{10} J$ (\mathcal{GS} set) [45] correspond to the mean 73 J-factor values for a source extension truncated at the outermost observed star. 74 The values $\log_{10} J$ (\mathcal{B} set) [47] are provided for a source extension at the tidal 75 radius of each dSph. Bolded sources are within HAWC's field of view and 76 provided to the Glory Duck analysis. 34</p> <p>77 Table 6.2 Summary of dSph observations by each experiment used in this work. A 78 ‘-’ indicates the experiment did not observe the dSph for this study. For 79 Fermi-LAT, the exposure at 1 GeV is given. For HAWC, $\Delta\theta$ is the absolute 80 difference between the source declination and HAWC latitude. HAWC is more 81 sensitive to sources with smaller $\Delta\theta$. For IACTs, we show the zenith angle 82 range, the total exposure, the energy range, the angular radius θ of the signal or 83 ON region, the ratio of exposures between the background-control (OFF) and 84 signal (ON) regions (τ), and the significance of gamma-ray excess in standard 85 deviations, σ. 35</p> <p>86 Table 7.1 Summary of the relevant properties of the dSphs used in the present work. 87 Column 1 lists the dSphs. Columns 2 and 3 present their heliocentric distance 88 and galactic coordinates, respectively. Column 4 reports the J-factors of each 89 source given from the \mathcal{LS} studies and estimated $\pm 1\sigma$ uncertainties. The 90 values $\log_{10} J$ (\mathcal{LS} set) [65] correspond to the mean J-factor values for a 91 source extension truncated at 0.5°. 65</p> <p>92 Table 7.2 Timing summaries for analyses for serial and multithreaded processes. M 93 tasks is the number of functional-parallel tasks ran for the computation. $T_{p,c}$ 94 is a single run time in hours:minutes:seconds for runs utilizing p nodes and 95 c threads. Runs are run interactively on the same computer to maximize 96 consistency. Empty entries are indicated with ‘-’. (.) entries are estimated 97 entries extrapolated from data earlier in the column. 69</p> <p>98 Table 7.3 Speed up summaries for analyses for serial and multithreaded processes. M 99 tasks is the number of functional-parallel tasks ran for the computation. $S_{p,c}$ 100 is a single speedup comparison for runs utilizing p nodes and c threads. $[\cdot]$ 101 are the estimated speedups calculated from Tab. 7.2, Eq. (7.10), and Eq. (7.5). 102 Empty entries are indicated with ‘-’. 71</p> <p>103 Proof I know how to include</p>	<p>67</p> <p>34</p> <p>35</p> <p>65</p> <p>69</p> <p>71</p>
--	---

LIST OF FIGURES

105	Figure 2.1	Rotation curve fit to NGC 6503 from [7]. Dashed line is the contribution 106 from visible matter. Dotted curves are from gas. Dash-dot curves are from 107 dark matter (DM). Solid line is the composite contribution from all matter 108 and DM sources. Data are indicated with bold dots with error bars. Data 109 agree strongly with a matter + DM composite prediction.	5
110	Figure 2.2	Light from distant galaxy is bent in unique ways depending on the distribution 111 of mass between the galaxy and Earth. Yellow dashed lines indicate where 112 the light would have gone if the matter were not present [8].	7
113	Figure 2.3	(left) Optical image of galactic cluster 1E0657-558. (right) X-ray image of the 114 cluster with redder meaning hotter and higher baryon density. (both) Green 115 contours are reconstruction of gravity contours from weak lensing. White 116 rings are the best fit mass maxima at 68.3%, 95.5%, and 99.7% confidence. 117 The matter maxima of the clusters are clearly separated from x-ray maxima. [9]	8
118	Figure 2.4	Plank CMB sky. Sky map features small variations in temperature in primor- 119 dial light. These anisotropies are used to make inferences about the universe's 120 energy budget and developmental history. [10]	9
121	Figure 2.5	Observed Cosmic Microwave Background power spectrum as a function of 122 multipole moment from Plank [10]. Blue line is best fit model from Λ CDM. 123 Red points and lines are data and error, respectively.	10
124	Figure 2.6	Predicted power spectra of CMB for different $\Omega_m h^2$ values for fixed baryon 125 density from [11]. (left) Low $\Omega_m h^2$ increases the prominence of first and 126 second peaks. (middle) $\Omega_m h^2$ is most similar to the observed power spectrum. 127 The second and third peaks are similar in height. (right) $\Omega_m h^2$ is large which 128 suppresses the first peak and raises the prominence of the third peak.	10
129	Figure 2.7	The Standard Model (SM) of particle physics. Figure taken from http://www.quantumdiaries.org/2014/03/14/the-standard-model-a-beautiful-but-flawed-theory/	12
132	Figure 2.8	Simplified Feynman diagram demonstrating with different ways DM can 133 interact with SM particles. The 'X's refer to the DM particles whereas the 134 SM refer to fundamental particles in the SM. The large circle in the center 135 indicates the vertex of interaction and is purposely left vague. The colored 136 arrows refer to different directions of time as well as their respective labels. 137 The arrows indicate the initial and final state of the DM -SM interaction in time.	13

138	Figure 2.9 A single jet event in ATLAS detector from 2017 [16]. Jet momentum was 139 observed to be 1.9 TeV. Missing transverse momentum was observed to be 140 1.9 TeV compared to the initial transverse momentum of the event was 0. 141 Implied MET is traced by a red dashed line in event display.	14
142	Figure 2.10 More detailed pseudo-Feynman diagram of particle cascade from dark matter 143 annihilation into 2 quarks. The quarks hadronize and down to stable particles 144 like γ or the anti-proton (p^-). Diagram pulled from ICRC 2021 presentation 145 on DM annihilation search [17].	15
146	Figure 2.11 Dark Matter (DM) decay spectrum for $b\bar{b}$ initial state and γ final state. Redder 147 spectra are for larger DM masses. Bluer spectra are light DM masses. x is a 148 unitless factor defined as the ratio of the mass of DM, m_χ , and the final state 149 particle energy E_γ . Figure from [19].	17
150	Figure 2.12 Different dark matter density profiles compared. Some models produce ex- 151 ceptionally large densities at small r [20].	18
152	Figure 2.13 The Milky Way Galaxy in photons (γ) and neutrinos (ν) [22]. The Galactic 153 center is at $l=0^\circ$ and is the brightest region in all panels. (top) An Optical 154 color image of the Milky Way galaxy seen from Earth. Clouds of gas and dust 155 obscure some light from stars. (2nd down) Integrated flux of γ -rays observed 156 by the Fermi-LAT telescope [23]. (middle) Expected neutrino emission 157 that corresponds with Fermi-LAT observations. (2nd up) Expected neutrino 158 emission profile after considering detector systematics of IceCube. (bottom) 159 Observed neutrino emission from region of the galactic plane. Substantial 160 neutrino emission was detected.	19
161	Figure 2.14 Dark Matter annihilation spectra for different final state particle and standard 162 model annihilation channels [24]. Photons (red), e^\pm (green), \bar{p} (blue), ν (black).	20
163	Figure 3.1 TODO: Show a nuclear reactor with cherenkov radiation[NEEDS A SOURCE][FACT 164 CHECK THIS]	22
165	Figure 3.2 TODO: absorption spectrum of liquid and solid water[NEEDS A SOURCE][FACT 166 CHECK THIS]	23

167	Figure 6.1 Sensitivities of five gamma-ray experiments compared to percentages of the 168 Crab nebula's emission and dark matter annihilation. Solid lines present 169 estimated sensitivities to power law spectra [FACT CHECK THIS]for each 170 experiment. Green lines are Fermi-LAT sensitivities where lighter green is 171 the sensitivity to the galactic center and dark green is its sensitivity to higher 172 declinations. Orange, red, and purple solid lines represent the MAGIC, HESS, 173 and VERITAS 50 hour sensitivities respectively. The maroon and brown lines 174 are the HAWC 1 year and 5 year sensitivities. Across four decades of gamma- 175 ray energy, these experiments have similar sensitivities on the order 10^{-12} 176 erg cm $^{-2}$ s $^{-1}$. The dotted lines are estimated dark matter fluxes assuming 177 $m_\chi = 5$ TeV DM annihilating to bottom quarks (red), tau leptons (blue), 178 and W bosons (green). Faded gray lines outline percentage flux of the Crab 179 nebula. Figure is an augmented version of [25]	27
180	Figure 6.2 Effect of Electroweak (EW) corrections on expected DM annihilation spec- 181 trum for $\chi\chi \rightarrow W^-W^+$. Solid lines are spectral models that consider EW 182 corrections. Dash-dot lines are spectral models without EW corrections. Red 183 lines are models for $M_\chi = 1$ TeV. Blue lines represent models for $M_\chi = 100$ 184 TeV. All models are sourced from the PPPC4DMID [44].	31
185	Figure 6.3 $\frac{dJ}{d\Omega}$ maps for Segue1 (top) and Coma Berenices (bottom). Origin is centered 186 on the specific dwarf spheroidal galaxies (dSph). X and Y axes are the 187 angular separation from the center of the dwarf. Plots of the remaining 11 188 dSph HAWC studied are linked in Fig. A.1.	33
189	Figure 6.4 Illustration of the combination technique showing a comparison between 190 $-2 \ln \lambda$ provided by four instruments (colored lines) from the observation 191 of the same dSph without any J nuisance and their sum, <i>i.e.</i> the resulting 192 combined likelihood (thin black line). According to the test statistics of 193 Equation (6.6), the intersection of the likelihood profiles with the line $-2 \ln \lambda$ 194 = 2.71 indicates the 95% C.L. upper limit on $\langle \sigma v \rangle$. The combined likelihood 195 (thin black line) shows a smaller value of upper limit on $\langle \sigma v \rangle$ than those 196 derived by individual instruments. We also show how the uncertainties on 197 the J factor effects the combined likelihood and degrade the upper limit on 198 $\langle \sigma v \rangle$ (thick black line). All likelihood profiles are normalized so that the global 199 minimum $\widehat{\langle \sigma v \rangle}$ is 0. We note that each profile depends on the observational 200 conditions in which a target object was observed. The sensitivity of a given 201 instrument can be degraded and the upper limits less constraining if the 202 observations are performed in non-optimal conditions such as a high zenith 203 angle or a short exposure time.	38
204	Figure 6.5 HAWC upper limits at 95% confidence level on $\langle \sigma v \rangle$ versus DM mass for 205 seven annihilation channels, using the set of J -factors from Ref. [53] The 206 solid line represents the observed combined limit. Dashed lines represent 207 limits from individual dSphs.	41

208	Figure 6.6 HAWC TS values for best fit $\langle\sigma v\rangle$ versus m_χ for seven SM annihilation channels with J factors from \mathcal{GS} . The solid black line shows the combined best fit TS values. The colored, dashed lines are the TS values for each of the 13 sources HAWC studied.	42
212	Figure 6.7 HAWC Brazil bands at 95% confidence level on $\langle\sigma v\rangle$ versus DM mass for seven annihilation channels with J -factors from \mathcal{GS} [53]. The solid line represents the combined limit from 13 dSphs. The dashed line is the expected limit. The green band is the 68% containment. The yellow band is the 95% containment.	43
217	Figure 6.8 Upper limits at 95% confidence level on $\langle\sigma v\rangle$ in function of the DM mass for eight annihilation channels, using the set of J factors from Ref. [53] (\mathcal{GS} set in Table 6.1). The black solid line represents the observed combined limit, the black dashed line is the median of the null hypothesis corresponding to the expected limit, while the green and yellow bands show the 68% and 95% containment bands. Combined upper limits for each individual detector are also indicated as solid, colored lines. The value of the thermal relic cross-section in function of the DM mass is given as the red dotted-dashed line [54].	44
226	Figure 6.9 Same as Fig. 6.8, using the set of J factors from Ref. [47, 55] (\mathcal{B} set in Table 6.1).	45
227	Figure 6.10 Comparisons of the combined limits at 95% confidence level for each of the eight annihilation channels when using the J factors from Ref. [53] (\mathcal{GS} set in Table 6.1), plain lines, and the J factor from Ref. [47, 55] (\mathcal{B} set in Table 6.1), dashed lines. The cross-section given by the thermal relic is also indicated [54].	47
231	Figure 6.11 Comparisons of the combined limits at 95% confidence level for a point source analysis and extended source using [53] \mathcal{GS} J-factor distributions and PPPC [44] annihilation spectra. Shown are the limits for Segue1 which will have the most significant impact on the combined limit. 6 of the 7 DM annihilation channels are shown. Solid lines are extended source studies. Dashed lines are point source studies. Overall, the extended source analysis improves the limit by a factor of 2.	49
238	Figure 6.12 Same as Fig. 6.11 on Coma Berenices. This dSph also contributes significantly to the limit. The limits are identical in this case.	50
240	Figure 6.13 Comparison of combined limits when correcting for HAWC's pointing systematic. All DM annihilation channels are shown. The solid black line is the ratio between published limit to the declination corrected limit. The blue solid line or "Combined_og" represented the limits computed for Glory Duck. The solid orange line or "Combined_ad" represented the limits computed after correcting for the pointing systematic.	51

246	Figure 6.14 Differential map of dJ/Ω from model built in Section 6.8.1 and profiles provided directly from authors. (Top) Differential from Segue1. (bottom) Differential from Coma Berenices. Note that their scales are not the same. Segue1 shows the deepest discrepancies which is congruent with its large uncertainties. Both models show anuli where unique models become apparent.	52
251	Figure 6.15 HAWC limits for Coma Berenices (top) and Segue1 (bottom) for two different map sets. Blue lines are limits calculated on maps with poor model representation. Orange lines are limits calculated on spatial profiles provided by the authors of [45]. Black line is the ratio of the poor spatial model limits to the corrected spatial models. The left y-axis measures $\langle\sigma v\rangle$ for the blue and orange lines. The right y-axis measures the ratio and is unitless.	53
257	Figure 6.16 Comparisons between the J -factors versus the angular radius for the computation of J factors from Ref. [53] (\mathcal{GS} set in Table 6.1) in blue and for the computation from Ref. [47, 55] (\mathcal{B} set in Tab. 6.1) in orange. The solid lines represent the central value of the J -factors while the shaded regions correspond to the 1σ standard deviation.	56
262	Figure 6.17 Comparisons between the J -factors versus the angular radius for the computation of J factors from Ref. [53] (\mathcal{GS} set in Tab. 6.1) in blue and for the computation from Ref. [47, 55] (\mathcal{B} set in Tab. 6.1) in orange. The solid lines represent the central value of the J -factors while the shaded regions correspond to the 1σ standard deviation.	57
267	Figure 7.1 Difference between spectral hypotheses from PPPC [44] and HDM [64]. Shown is the expected DM annihilation spectrum for $\chi\chi \rightarrow W^-W^+$. Solid lines are spectral models with EW corrections from the PPPC. Dash-dot lines are spectral models from HDM. Red lines are models for $M_\chi = 1$ TeV. Blue lines represent models for $M_\chi = 100$ TeV.	62
272	Figure 7.2 Photon spectra for $\chi\chi \rightarrow \gamma\gamma$ (left) and $\chi\chi \rightarrow ZZ$ (right) after gaussian convolution of line features. Both spectra have δ -features at photon energies equal to the DM mass. Bluer lines are annihilation spectra with lower DM mass. Redder lines are spectra from larger DM mass. All Spectral models are sourced from the Heavy Dark Matter models [64]. Axes are drawn roughly according to the energy sensitivity of HAWC.	63
278	Figure 7.3 $\frac{dJ}{d\Omega}$ maps for Coma Berenices, Draco, Segue1, and Sextans. Columns are divided for the $\pm 1\sigma$ uncertainties in $dJ/d\Omega$ around the mean value from \mathcal{LS} [65]. Origin is centered on the specific dwarf spheroidal galaxies (dSph). θ and ϕ axes are the angular separation from the center of the dwarf	64

282	Figure 7.4	Infographic on how jobs and DM computation was organized in Section 6.3. Jobs were built for each permutation of CHANS and SOURCES shown by the left block in the figure. Each job, which took on the order 2 hrs to compute, had the following work flow: 1. Import HAWC analysis software, 2 min to run. 2. Load HAWC count maps, 5 min to run. 3. Load HAWC energy and spatial resolutions, 4 min. 5. Load DM spatial source templates and spectral models, less than 1 s. 6. Perform likelihood fit on data and model, about 8 min per DM mass. 7. Write results to file, less than 1s.	66
290	Figure 7.5	Graphic of Gustafson parallel coding pattern. f_s is the fraction of a program, in time, spent on serial computation. f_p is the fraction of computing time that is parallelizable. T_p is the total time for a parallel program to run. T_1 is the total time for a parallel program to run if only 1 processor is allocated. P_N is the N -th processor where it's row is the computation the processor performs. The Gustafson pattern is most similar to what is implemented for this analysis. Figure is pulled from [67].	67
297	Figure 7.6	Task chart for one multi-threaded job developed for this project. Green blocks indicate a shared resource across the threads AND computation performed serially. Red blocks indicate functional parallel processing within each thread. 3 threads are represented here, yet many more can be employed during the full analysis. Jobs are defined by the SOURCE as these require unique maps to be loaded into the likelihood estimator. The m_χ , CHAN, and $\langle\sigma v\rangle$ variables are entered into the thread pool and allocated as evenly as possible across the threads.	69
305	Figure 7.7	TODO: fill this out	72
306	Figure 7.8	TODO: fill this out	73
307	Figure 7.9	TODO: fill this out	74
308	Figure 7.10	TODO: fill this out	75
309	Figure 7.11	TODO: Comparison of channels with GD combined results.[NEEDS A SOURCE][FACT CHECK THIS]	76
311	Figure 7.12	TODO: show p1 and m1 limits around[NEEDS A SOURCE][FACT CHECK THIS]	77
313	Figure 7.13	TODO: there will be 2[NEEDS A SOURCE][FACT CHECK THIS]	78
314	Figure A.1	Sister figure to Figure 6.3. Sources in the first row from left to right: Bootes I, Canes Venatici I, II. In second row: Draco, Hercules, Leo I. In the first row: Leo II, Leo IV, Sextans. In the final row: Ursa Major I, Ursa Major II.	81

317	Figure B.1 Sister figure to Figure 7.2 for remaining SM primary annihilation channels	
318	studied for this thesis. These did not require any post generation smoothing	
319	and so are directly pulled from [64] with a binning scheme most helpful for a	
320	HAWC analysis.	82

LIST OF ABBREVIATIONS

- 322 **MSU** Michigan State University
323 **LANL** Los Alamos National Laboratory
324 **DM** Dark Matter
325 **SM** Standard Model
326 **HAWC** High Altitude Water Cherenkov Observatory
327 **dSph** Dwarf Spheroidal Galaxy

CHAPTER 1**INTRODUCTION**

329 Is the text not rendering right? Ah ok it knows im basically drafting the doc still

CHAPTER 2

330

DARK MATTER IN THE COSMOS

331 **2.1 Introduction**

332 The dark matter problem can be summarized in part by the following thought experiment.

333 Let us say you are the teacher for an elementary school classroom. You take them on a field
334 trip to your local science museum and among the exhibits is one for mass and weight. The exhibit
335 has a gigantic scale, and you come up with a fun problem for your class.

336 You ask your class, "What is the total weight of the classroom? Give your best estimation to
337 me in 30 minutes, and then we'll check your guess on the scale. If your guess is within 10% of the
338 right answer, we will stop for ice cream on the way back."

339 The students are ecstatic to hear this, and they get to work. The solution is some variation of
340 the following strategy. The students should give each other their weight or best guess if they do
341 not know. Then, all they must do is add each student's weight and get a grand total for the class.

342 The measurement on the giant scale should show the true weight of the class. When comparing
343 the measured weight to your estimation, multiply the measurement by 1.0 ± 0.1 to get the $\pm 10\%$
344 tolerances for your estimation.

345 Two of your students, Sandra and Mario, return to you with a solution.

346 They say, "We weren't sure of everyone's weight. We used 65 lbs. for the people we didn't
347 know and added everyone who does know. There are 30 of us, and we got 2,000 lbs.! That's a ton!"

348 You estimated 1,900 lbs. assuming the average weight of a student in your class was 60 lbs.
349 So, you are pleased with Sandra's and Mario's answer. You instruct your students to all gather on
350 the giant scale and read off the weight together. To all your surprise, the scale reads *10,000 lbs.*!
351 10,000 is significantly more than a 10% error from 2,000. In fact, it is approximately 5 times more
352 massive than either your or your students' estimates. You think to yourself and conclude there
353 must be something wrong with the scale. You ask an employee to check the scale and verify it is
354 well calibrated. They confirm that the scale is in working order. You weigh a couple of students
355 individually to assess that the scale is well calibrated. Sandra weighs 59 lbs., and Mario weighs

356 62 lbs., typical weights for their age. You then weigh each student individually and see that their
357 weights individually do not deviate greatly from 60 lbs. So, where does all the extra weight come
358 from?

359 This thought experiment serves as an analogy to the Dark Matter problem. The important
360 substitution to make however is to replace the students with stars and the classroom with a galaxy,
361 say the Milky Way. Individually the mass of stars is well measured and defined with the Sun as our
362 nearest test case. However, when we set out to measure the mass of a collection of stars as large as
363 galaxies, our well-motivated estimation is wildly incorrect. There simply is no way to account for
364 this discrepancy except without some unseen, or dark, contribution to mass and matter in galaxies.
365 I set out in my thesis to narrow the possibilities of what this Dark Matter could be.

366 This chapter is organized like the following... **TODO: Text should look like ... Chapter x has**
367 **blah blah blah.**

368 **2.2 Dark Matter Basics**

369 Presently, a more compelling theory of cosmology that includes Dark Matter (DM) in order
370 to explain a variety of observations is Λ Cold Dark Matter, or Λ CDM. I present the evidence
371 supporting Λ CDM in Section 2.3 yet discuss the conclusions of the Λ CDM model here. According
372 to Λ CDM fit to observations on the Cosmic Microwave Background (CMB), DM is 26.8% of the
373 universe's current energy budget. Baryonic matter, stuff like atoms, gas, and stars, contributes to
374 4.9% of the universe's current energy budget [1, 2, 3].

375 DM is dark; it does not interact readily with light at any wavelength. DM also does not interact
376 noticeably with the other standard model forces (Strong and Weak) at a rate that is readily observed
377 [3]. DM is cold, which is to say that the average velocity of DM is below relativistic speeds [1].
378 'Hot' DM would not likely manifest the dense structures we observe like galaxies, and instead
379 would produce much more diffuse galaxies than what is observed [3, 1]. DM is old; it played a
380 critical role in the formation of the universe and the structures within it [1, 2].

381 Observations of DM have so far been only gravitational. The parameter space available to what
382 DM could be therefore is extremely broad. The broad DM parameter space is iteratively tested in

383 DM searches by supposing a hypothesis that has not yet been ruled out and performing observations
384 to test them. When the observations yield a null result, the parameter space is constrained further.
385 I present some approaches for DM searches in Section 2.4.

386 **2.3 Evidence for Dark Matter**

387 Dark Matter (DM) has been a looming problem in physics for almost 100 years. Anomalies
388 have been observed by astrophysicists in galactic dynamics as early as 1933 when Fritz Zwicky
389 noticed unusually large velocity dispersion in the Coma cluster. Zwicky's measurement was the
390 first recorded to use the Virial theorem to measure the mass fraction of visible and invisible matter
391 in celestial bodies [4]. From Zwicky in [5], "*If this would be confirmed, we would get the surprising*
392 *result that dark matter is present in much greater amount than luminous matter.*" Zwicky's and
393 others' observation did not instigate a crisis in astrophysics because the measurements did not
394 entirely conflict with their understanding of galaxies [4]. In 1978, Rubin, Ford, and Norbert
395 measured rotation curves for ten spiral galaxies [6]. Rubin et al.'s 1978 publication presented a
396 major challenge to the conventional understanding of galaxies that could no longer be dismissed by
397 measurement uncertainties. Evidence has been mounting ever since for this exotic form of matter.
398 The following subsections provide three compelling pieces of evidence in support of the existence
399 of DM.

400 **2.3.1 First Clues: Stellar Velocities**

401 Zwicky, and later Rubin, measured the stellar velocities of various galaxies to estimate their
402 virial mass. The Virial Theorem upon which these observations are interpreted is written as

$$2T + V = 0. \quad (2.1)$$

403 Where T is the kinetic energy and V is the potential energy in a self-gravitating system. The
404 classical Newton's law of gravity from stars and gas was used for gravitational potential modeled in
405 the observed galaxies:

$$V = -\frac{1}{2} \sum_i \sum_{j \neq i} \frac{m_i m_j}{r_{ij}}. \quad (2.2)$$

406 Zwicky et al. measured just the velocities of stars apparent in optical wavelengths [5]. Rubin et al.
 407 added by measuring the velocity of the hydrogen gas via the 21 cm emission line of Hydrogen [6].
 408 The velocities of the stars and gas are used to infer the total mass of galaxies and galaxy clusters
 409 via Equation (2.1). An inferred mass is obtained from the luminosity of the selected sources. The
 410 two inferences are compared to each other as a luminosity to mass ratio which typically yielded [1]

$$\frac{M}{L} \sim 400 \frac{M_{\odot}}{L_{\odot}} \quad (2.3)$$

411 M_{\odot} and L_{\odot} referring to stellar mass and stellar luminosity, respectively. These ratios clearly indicate
 412 a discrepancy in apparent light and mass from stars and gas and their velocities.

413 Rubin et al. [6] demonstrated that the discrepancy was unlikely to be an underestimation of
 414 the mass of the stars and gas. The inferred "dark" mass was up to 5 times more than the luminous
 415 mass. This dark mass also needed to extend well beyond the extent of the luminous matter.

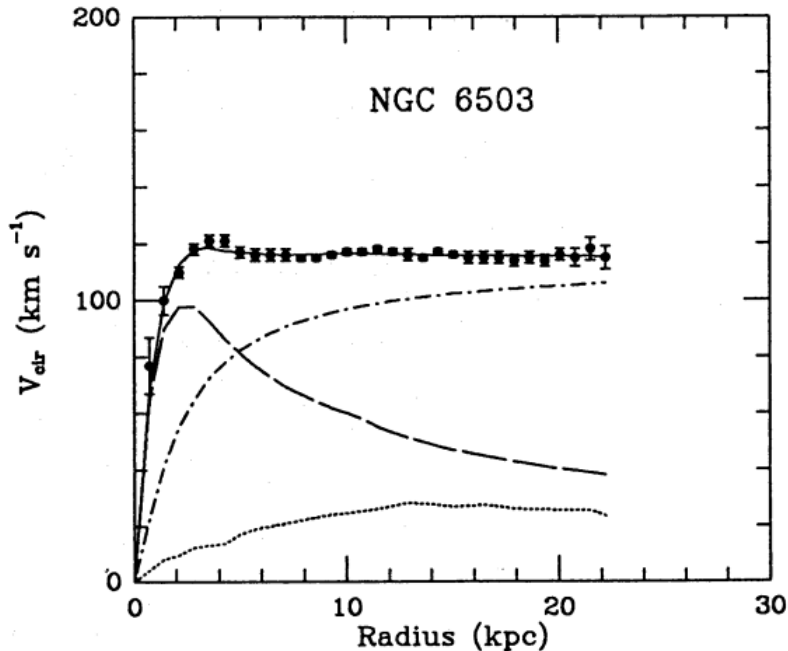


Figure 2.1 Rotation curve fit to NGC 6503 from [7]. Dashed line is the contribution from visible matter. Dotted curves are from gas. Dash-dot curves are from dark matter (DM). Solid line is the composite contribution from all matter and DM sources. Data are indicated with bold dots with error bars. Data agree strongly with a matter + DM composite prediction.

416 Figure 2.1 features one of many rotation curves plotted from the stellar velocities within galaxies.

417 The measured rotation curves mostly feature a flattening of velocities at higher radius which is not
418 expected if the gravity was only coming from gas and luminous matter. The extension of the
419 flat velocity region also indicates that the DM is distributed far from the center of the galaxy.
420 Modern velocity measurements include significantly larger objects, galactic clusters, and smaller
421 objects, dwarf galaxies. Yet, measurements along this regime are leveraging the Virial theorem
422 with Newtonian potential energies. We know Newtonian gravity is not a comprehensive description
423 of gravity. New observational techniques have been developed since 1978, and those are discussed
424 in the following sections.

425 **2.3.2 Evidence for Dark Matter: Gravitational Lensing**

426 Modern evidence for dark matter comes from new avenues beyond stellar velocities. Grav-
427 itational lensing from DM is a new channel from general relativity. General relativity predicts
428 aberrations in light caused by massive objects. In recent decades we have been able to measure the
429 lensing effects from compact objects and DM halos. Figure 2.2 shows how different massive ob-
430 jects change the final image of a faraway galaxy resulting from gravitational lensing. Gravitational
431 lensing developed our understanding of dark matter in two important ways.

432 Gravitational lensing provides additional compelling evidence for DM. The observation of two
433 merging galactic clusters in 2006, shown in Figure 2.3, provided a compelling argument for DM
434 outside the Standard Model. These clusters merged recently in astrophysical time scales. Galaxies
435 and star cluster have mostly passed by each other as the likelihood of their collision is low. Therefore,
436 these massive objects will mostly track the highest mass, dark and/or baryonic, density. Yet, the
437 intergalactic gas is responsible for the majority of the baryonic mass in the systems [4]. These gas
438 bodies will not phase through and will heat up as they collide together. The hot gas is located via
439 x-ray emission from the cluster. Two observations of the clusters were performed independently of
440 each other.

441 The first was the lensing of light around the galaxies due to their gravitational influences.
442 When celestial bodies are large enough, the gravity they exert bends space and time itself. The
443 warped space-time lenses light and will deflect in an analogous way to how glass lenses will bend

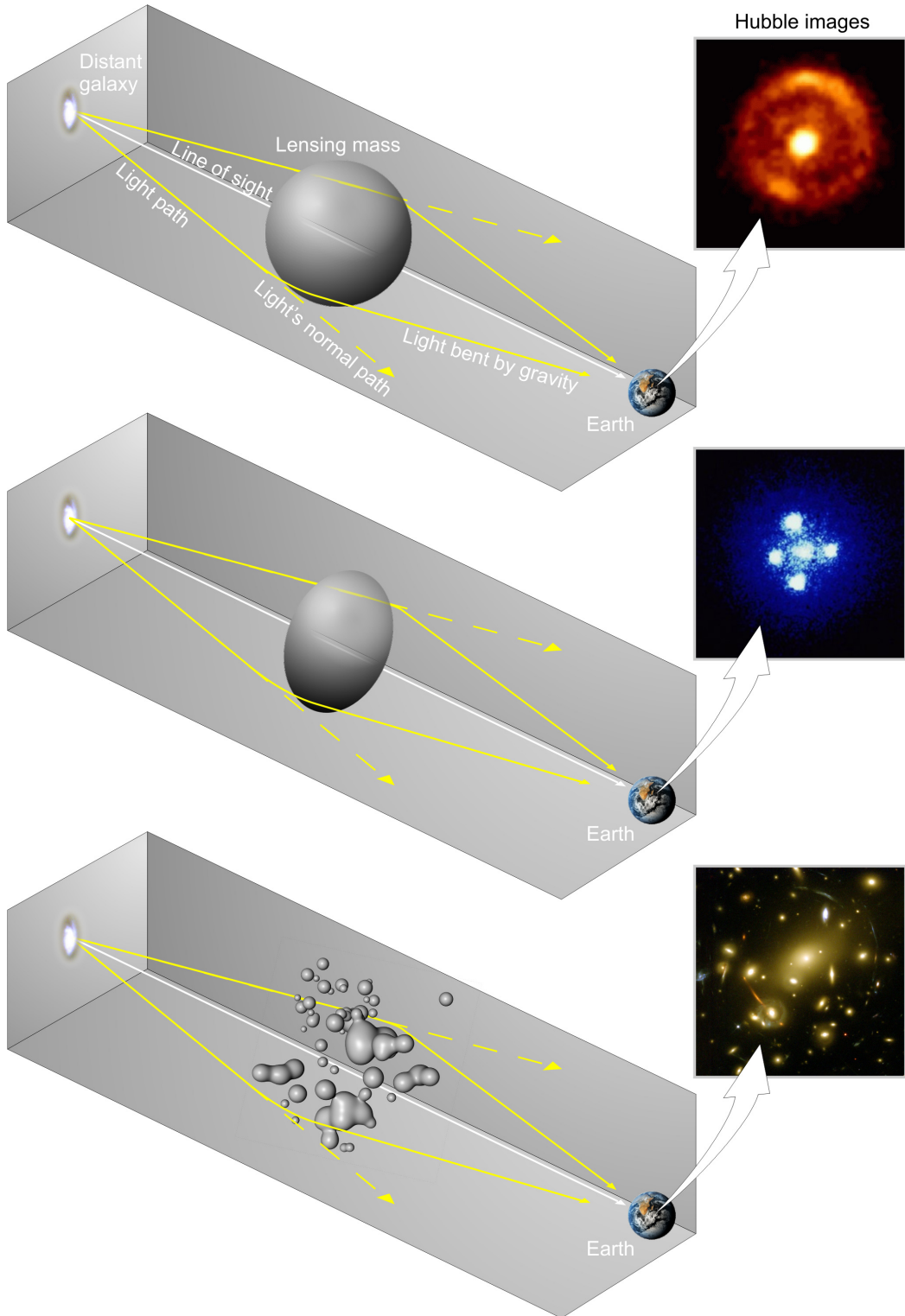


Figure 2.2 Light from distant galaxy is bent in unique ways depending on the distribution of mass between the galaxy and Earth. Yellow dashed lines indicate where the light would have gone if the matter were not present [8].

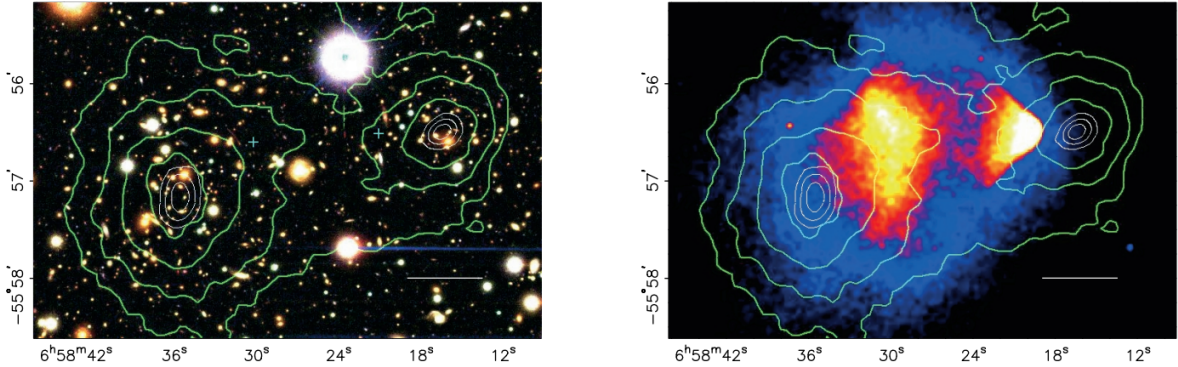


Figure 2.3 (left) Optical image of galactic cluster 1E0657-558. (right) X-ray image of the cluster with redder meaning hotter and higher baryon density. (both) Green contours are reconstruction of gravity contours from weak lensing. White rings are the best fit mass maxima at 68.3%, 95.5%, and 99.7% confidence. The matter maxima of the clusters are clearly separated from x-ray maxima. [9]

444 light, see Figure 2.2. With a sufficient understanding of light sources behind a massive object, we
 445 can reconstruct the contours of the gravitational lenses. The gradient of the contours shown in
 446 Figure 2.3 then indicates how dense the matter is and where it is.

447 The x-ray emission can then be observed from the clusters. Since these galaxies are mostly gas
 448 and are merging, then the gas should be getting hotter. If they are merging, the x-ray emissions
 449 should be the strongest where the gas is mostly moving through each other. Hence, X-ray emission
 450 maps out where the gas is in the merging galaxy cluster.

451 The lensing and x-ray observations were done on the Bullet cluster featured on Figure 2.3.
 452 The x-ray emissions do not align with the gravitational contours from lensing. The incongruence
 453 in mass density and baryon density suggests that there is a lot of matter somewhere that does
 454 not interact with light. Moreover, this dark matter cannot be baryonic [9]. The Bullet Cluster
 455 measurement did not really tell us what DM is exactly, but it did give the clue that DM also does
 456 not interact with itself very strongly. If DM did interact strongly with itself, then it would have been
 457 more aligned with the x-ray emission [9]. There have been follow-up studies of galaxy clusters with
 458 similar results. The Bullet Cluster and others like it provide a persuasive case against something
 459 possibly amiss in our gravitational theories.

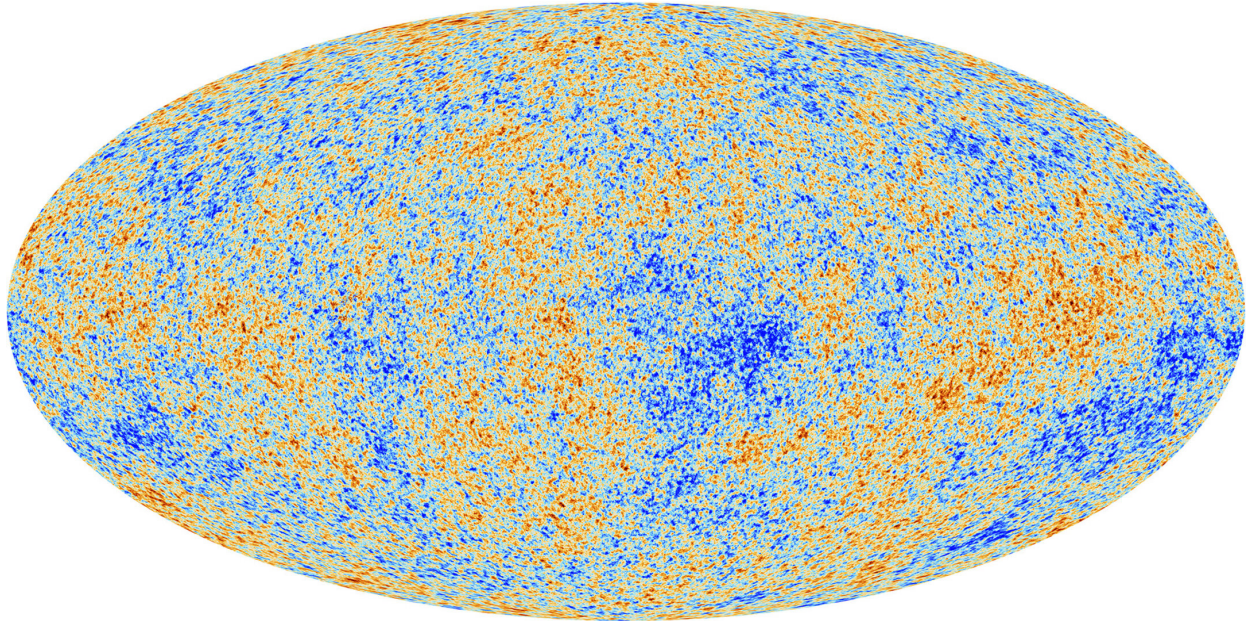


Figure 2.4 Plank CMB sky. Sky map features small variations in temperature in primordial light. These anisotropies are used to make inferences about the universe’s energy budget and developmental history. [10]

460 **2.3.3 Evidence for Dark Matter: Cosmic Microwave Background**

461 The Cosmic Microwave Background (CMB) is the primordial light from the early universe
462 when Hydrogen atoms formed from the free electron and proton soup in the early universe. The
463 CMB is the earliest light we can observe; released when the universe was about 380,000 years old.
464 Then we look at how the simulated universes look like compared to what we see. Figure 2.4 is the
465 most recent CMB image from the Plank satellite after subtracting the average value and masking the
466 galactic plane [10]. Redder regions indicate a slightly hotter region in the CMB, and blue indicates
467 colder. The intensity variations are on the order of 1 in 1000 with respect to the average value.

468 The Cosmic Microwave Background shows that the universe had DM in it from an incredibly
469 early stage. To measure the DM, Dark Energy, and matter fractions of the universe from the CMB,
470 the image is analyzed into a power spectrum, which shows the amplitude of the fluctuations as
471 a function of spherical multipole moments. Λ CDM provides the best fit to the power spectra of
472 the CMB as shown in Figure 2.5. The CMB power spectrum is quite sensitive to the fraction
473 of each energy contribution in the early universe. Low l modes are dominated by variations
474 in gravitational potential. Intermediate l emerge from oscillations in photon-baryon fluid from

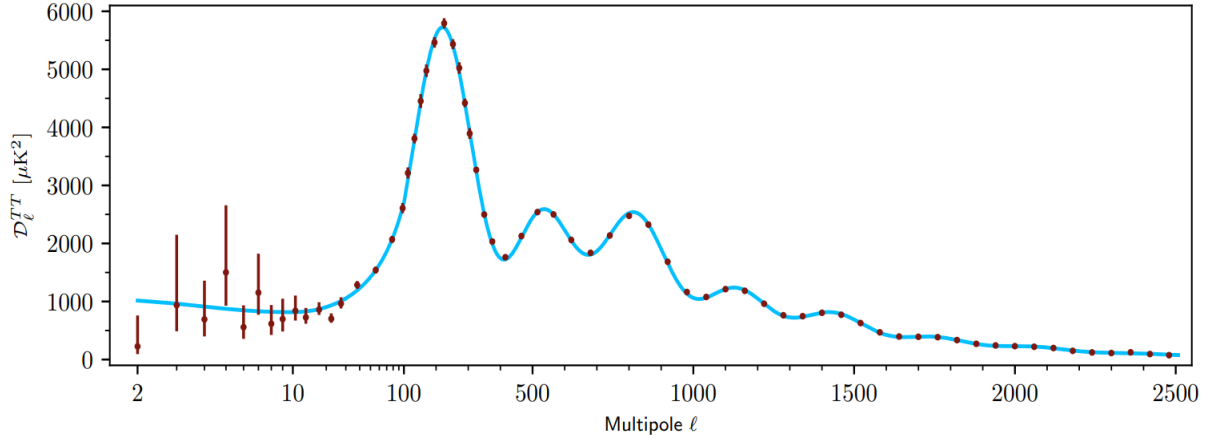


Figure 2.5 Observed Cosmic Microwave Background power spectrum as a function of multipole moment from Plank [10]. Blue line is best fit model from Λ CDM. Red points and lines are data and error, respectively.

475 competing baryon pressures and gravity. High l is a damped region from the diffusion of photons
 476 during electron-proton recombination. [1]

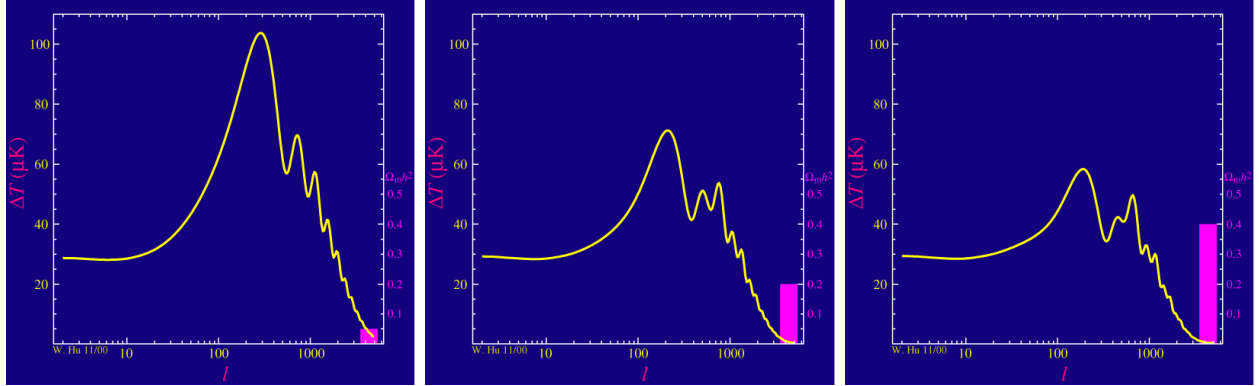


Figure 2.6 Predicted power spectra of CMB for different $\Omega_m h^2$ values for fixed baryon density from [11]. (left) Low $\Omega_m h^2$ increases the prominence of first and second peaks. (middle) $\Omega_m h^2$ is most similar to the observed power spectrum. The second and third peaks are similar in height. (right) $\Omega_m h^2$ is large which suppresses the first peak and raises the prominence of the third peak.

477 The harmonics would look quite different for a universe with less DM. Figure 2.6 demonstrates
 478 the effect $\Omega_m h^2$ has on the expected power spectrum for fixed baryon matter density. [11] Sweeping
 479 $\Omega_m h^2$ in this way clearly shows the effect dark matter has on the CMB power spectrum. The
 480 observations fit well with the Λ CDM model, and the derived fractions are as follows. The matter
 481 fraction: $\Omega_m = 0.3153$; and the baryon fraction: $\Omega_b = 0.04936$ [10]. Plank's observations also
 482 provide a measure of the Hubble constant, H_0 . H_0 especially has seen a growing tension in the

483 past decade that continues to deepened with observations from instruments like the James Webb
484 Telescope [12, 13]. As Hubble tensions deepen, we may find that perhaps Λ **CDM**, despite its
485 successes, is missing some critical physics.

486 Overall, the Newtonian motion of stars in galaxies, weak lensing from galactic clusters, and
487 power spectra from primordial light form a compelling body of research in favor of dark matter.
488 It takes another leap of theory and experimentation to make observations of DM that are non-
489 gravitational in nature. In Section 2.3, the evidence for DM implies strongly that the DM is matter
490 and not a lost parameter in the gravitational fields between massive objects. Finally, if we take one
491 axiom: that this matter has quantum behavior, such as being described by some Bohr wavelength
492 and abiding by some fermion or boson statistics; then we arrive at particle dark matter. One particle
493 DM hypothesis is the Weakly Interacting Massive Particle (WIMP). This DM candidate theory is
494 discussed further in the next section and is the focus of this thesis.

495 **2.4 Searching for Dark Matter: Particle DM**

496 Section 2.4 shows the Standard Model of particle physics and is currently the most accurate
497 model for the dynamics of fundamental particles like electrons and photons. The current status
498 of the SM does not have a viable DM candidate. When looking at the standard model, we can
499 immediately exclude any charged particle because charged particles interact strongly with light.
500 Specifically, this will rule out the following charged, fundamental particles: $e, \mu, \tau, W, u, d, s, c, t, b$
501 and their corresponding antiparticles. Recalling from Section 2.2 that DM must be long-lived and
502 stable over the age of the universe which excludes all SM particles with decay half-lives at or shorter
503 than the age of the universe. The lifetime constraint additionally eliminates the Z and H bosons.
504 Finally, the candidate DM needs to be somewhat massive. Recall from Section 2.2 that DM is cold
505 or not relativistic through the universe. This eliminates the remaining SM particles: $\nu_{e,\mu,\tau}, g, \gamma$ as
506 DM candidates. Because there are no DM candidates within the SM, the DM problem strongly
507 hints to physics beyond the SM (BSM).

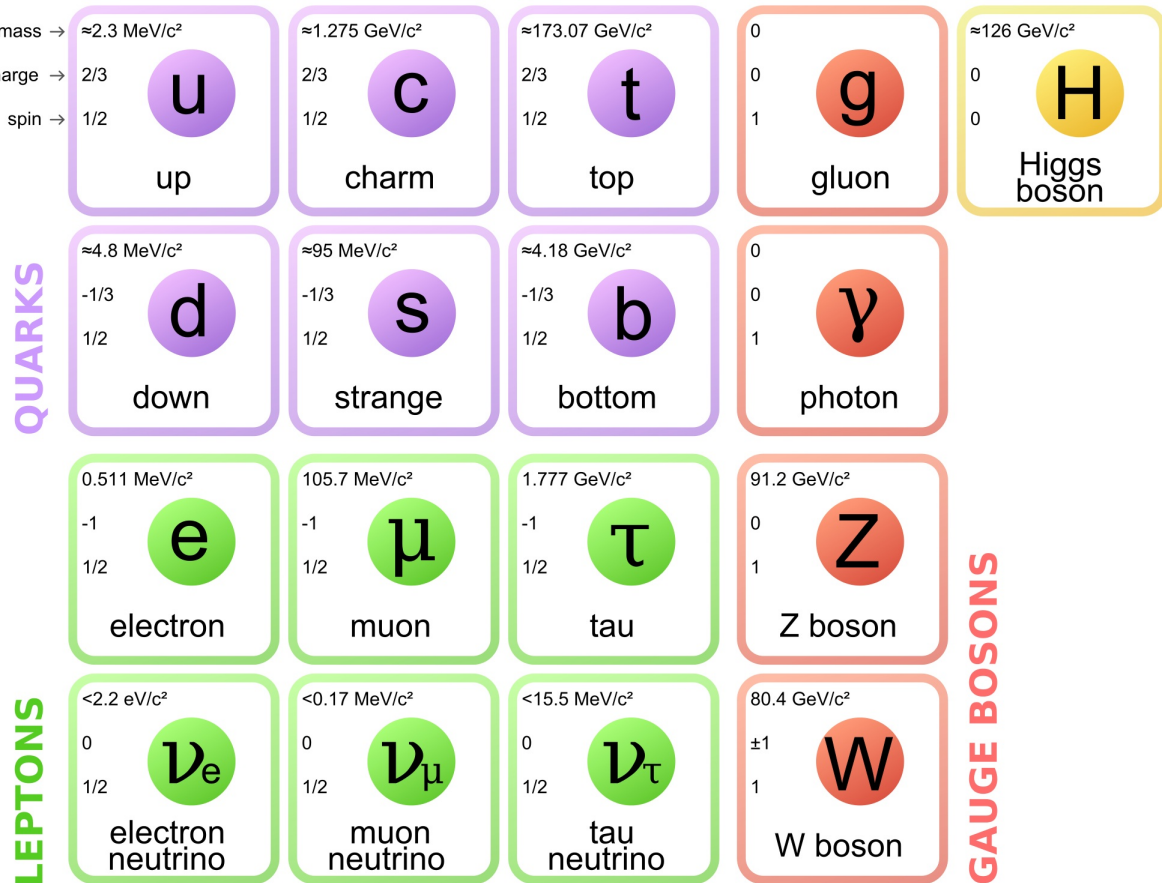


Figure 2.7 The Standard Model (SM) of particle physics. Figure taken from <http://www.quantumdiaries.org/2014/03/14/the-standard-model-a-beautiful-but-flawed-theory/>

508 2.4.1 Shake it, Break it, Make it

509 When considering DM that couples in some way with the SM, the interactions are roughly
 510 demonstrated by interaction demonstrated in Figure 2.8. The figure is a simplified Feynman
 511 diagram where the arrow of time represents the interaction modes of: **Shake it, Break it, Make it**.
 512 **Shake it** refers to the direct detection of dark matter. Direct detection interactions start with
 513 a free DM particle and an SM particle. The DM and SM interact via elastic or inelastic collision
 514 and recoil away from each other. The DM remains in the dark sector and imparts some momentum
 515 onto the SM particle. The hope is that the momentum imparted onto the SM particle is sufficiently
 516 high enough to pick up with extremely sensitive instruments. Because we cannot create the DM in
 517 the lab, a direct detection experiment must wait until DM is incident on the detector. Most direct
 518 detection experiments are therefore placed in low-background environments with inert detection

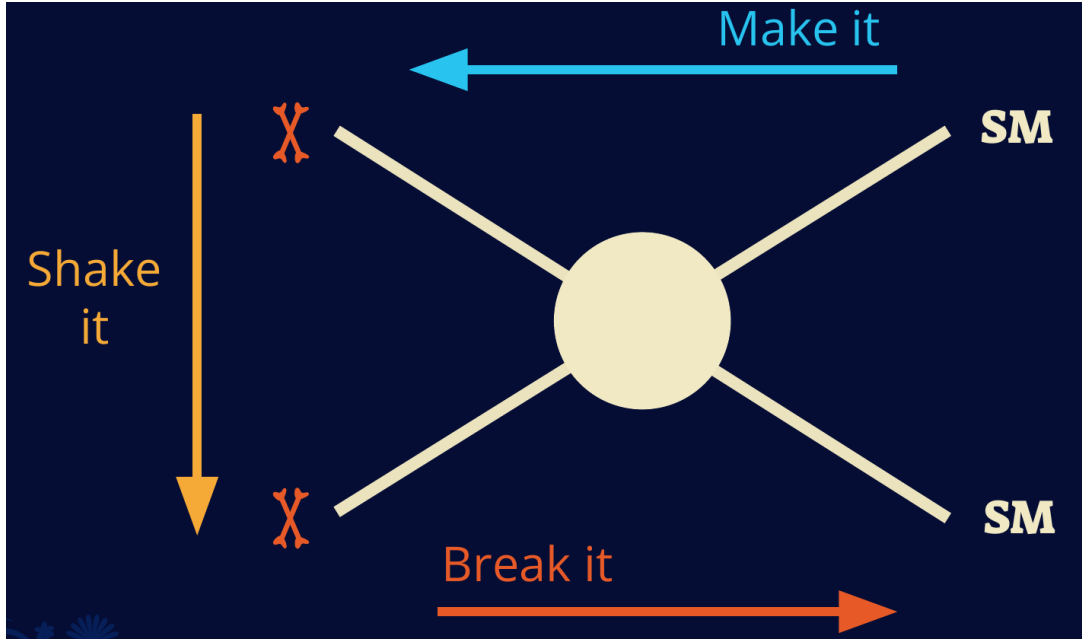


Figure 2.8 Simplified Feynman diagram demonstrating different ways DM can interact with SM particles. The 'X's refer to the DM particles whereas the SM refer to fundamental particles in the SM. The large circle in the center indicates the vertex of interaction and is purposely left vague. The colored arrows refer to different directions of time as well as their respective labels. The arrows indicate the initial and final state of the DM -SM interaction in time.

519 media like the noble gas Xenon. [14]

520 **Make it** refers to the production of DM from SM initial states. The experiment starts with
 521 particles in the SM. These SM particles are accelerated to incredibly high energies and then collide
 522 with each other. In the confluence of energy, DM hopefully emerges as a byproduct of the SM
 523 annihilation. Often it is the collider experiments that are energetic enough to hypothetically produce
 524 DM. These experiments include the world-wide collaborations ATLAS and CMS at CERN where
 525 proton collide together at extreme energies. The DM searches, however, are complex. DM likely
 526 does not interact with the detectors and lives long enough to escape the detection apparatus of
 527 CERN's colliders. This means any DM production experiment searches for an excess of events
 528 with missing momentum or energy in the events. An example event with missing transverse
 529 momentum is shown in Figure 2.9. The missing momentum with no particle tracks implies a
 530 neutral particle carried the energy out of the detector. However, there are other neutral particles
 531 in the SM, like neutrons or neutrinos, so any analysis has to account for SM signatures of missing

532 momentum. [15]

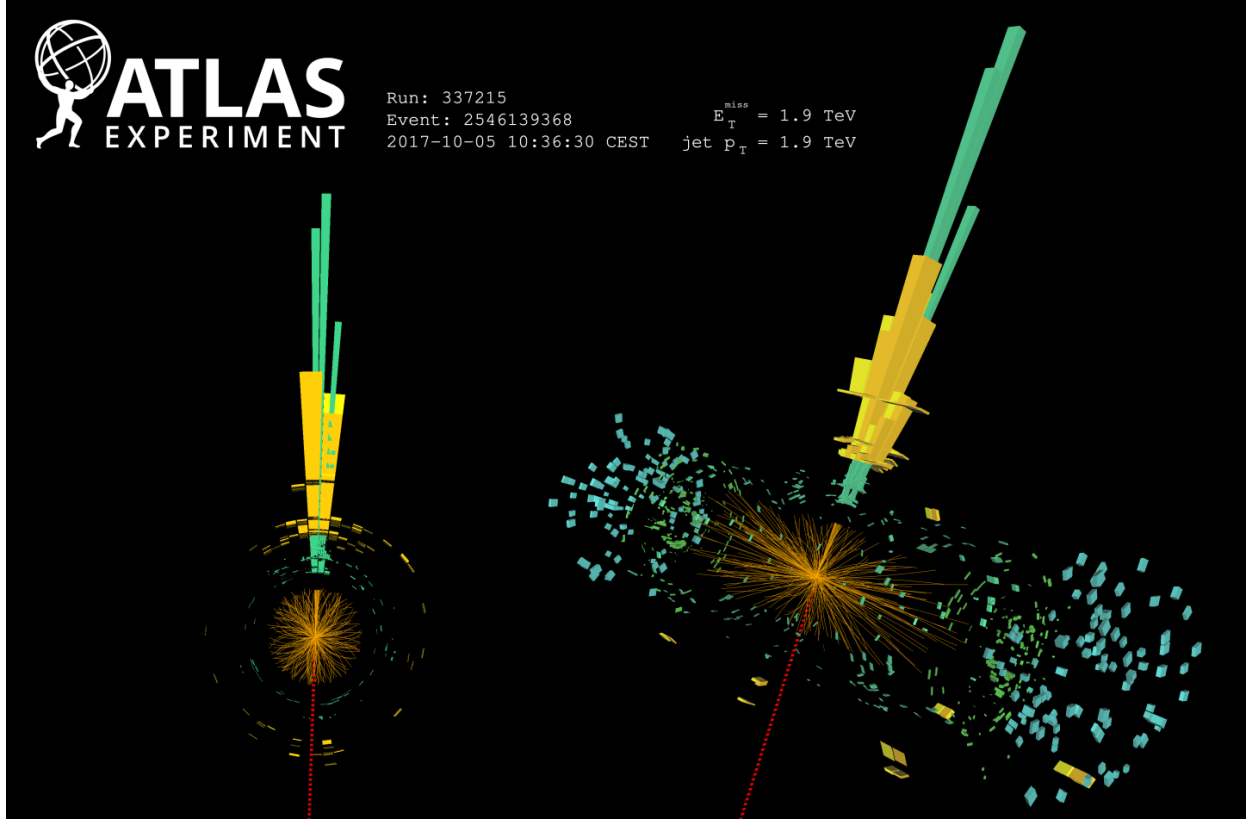


Figure 2.9 A single jet event in ATLAS detector from 2017 [16]. Jet momentum was observed to be 1.9 TeV. Missing transverse momentum was observed to be 1.9 TeV compared to the initial transverse momentum of the event was 0. Implied MET is traced by a red dashed line in event display.

533 2.4.2 Break it: Standard Model Signatures of Dark Matter through Indirect Searches

534 **Break it** refers to the creation of SM particles from the dark sector, and it is the primary focus
535 of this thesis. The interaction begins with DM or in the dark sector. The hypothesis is that this
536 DM will either annihilate with itself or decay and produce an SM byproduct. This method is
537 often referred to as the Indirect Detection of DM because we have no lab to directly control or
538 manipulate the DM. Therefore, most indirect DM searches are performed using observations of
539 known DM densities among the astrophysical sources. The strength is that we have the whole of the
540 universe and its 13.6-billion-year lifespan to use as a detector and particle accelerator. Additionally,
541 locations of dark matter are well cataloged since it was astrophysical observations that presented

542 the problem of DM in the first place.

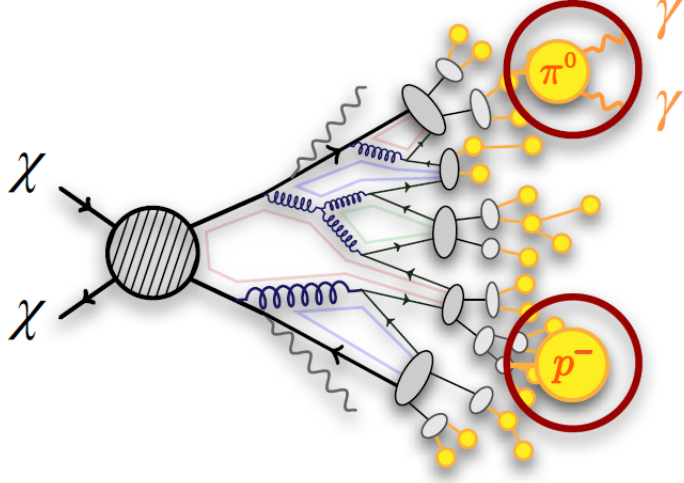


Figure 2.10 More detailed pseudo-Feynman diagram of particle cascade from dark matter annihilation into 2 quarks. The quarks hadronize and down to stable particles like γ or the anti-proton (p^-). Diagram pulled from ICRC 2021 presentation on DM annihilation search [17].

543 However, anything can happen in the universe. There are many difficult to deconvolve back-
544 grounds when searching for DM. One prominent example is the galactic center. We know the
545 galactic center has a large DM content because of stellar kinematics in our Milky Way and DM halo
546 simulations. Yet, any signal from the galactic center is challenging to parse apart from the extreme
547 environment of our supermassive black hole, unresolved sources, and diffuse emission from the
548 interstellar medium [18]. Despite the challenges, any DM model that yields evidence in the other
549 two observation methods, **Shake it or Make it** must be corroborated with indirect observations of
550 the known DM sources. Without corroborating evidence, DM observation in the lab is hard-pressed
551 to demonstrate that it is the model contributing to the DM seen at the universal scale.

552 In the case of WIMP DM, signals are described in terms of primary SM particles produced
553 from DM decay or annihilation. The SM initial state particles are then simulated down to stable
554 final states such as the γ , ν , p , or e which can traverse galactic lengths to reach Earth.

555 Figure 2.10 shows the quagmire of SM particles that emerges from SM initial states that are not
556 stable [17]. There are many SM particles with varying energies that can be produced in such an

557 interaction. For any arbitrary DM source and stable SM particle, the SM flux from DM annihilating
 558 to a neutral particle in the SM, ϕ , from a region in the sky is described by the following.

$$\frac{d\Phi_\phi}{dE_\phi} = \frac{\langle\sigma v\rangle}{8\pi m_\chi^2} \frac{dN_\phi}{dE_\phi} \times \int_{\text{source}} d\Omega \int_{l.o.s} \rho_\chi^2 dl(r, \theta') \quad (2.4)$$

559 In Equation (6.1), $\langle\sigma v\rangle$ is the velocity-weighted annihilation cross-section of DM to the SM. m_χ
 560 refers to the mass of DM, noted with Greek letter χ . $\frac{dN_\phi}{dE_\phi}$ is the N particle flux weighted by the
 561 particle energy. An example is provided in Figure 2.11 for the γ final state. The integrated terms
 562 are performed over the solid angle, $d\Omega$, and line of sight, l.o.s. ρ is the density of DM for a
 563 location (r, θ') in the sky. The terms left of the ' \times ' are often referred to as the particle physics
 564 component. The terms on the right are referred to as the astrophysical component. For decaying
 565 DM, the equation changes to...

$$\frac{d\Phi_\phi}{dE_\phi} = \frac{1}{4\pi\tau m_\chi} \frac{dN_\phi}{dE_\phi} \times \int_{\text{source}} d\Omega \int_{l.o.s} \rho_\chi dl(r, \theta') \quad (2.5)$$

566 In Equation (7.1), τ is the decay lifetime of the DM. Just as in Equation (6.1), the left and right
 567 terms are the particle physics and the astrophysical components respectively. The integrated
 568 astrophysical component of Equation (6.1) is often called the J-Factor. Whereas the integrated
 569 astrophysical component of Equation (7.1) is often called the D-Factor.

570 Exact DM $\text{DM} \rightarrow \text{SM SM}$ branching ratios are not known, so it is usually assumed to go 100%
 571 into an SM particle/anti-particle. Additionally, when a DM annihilation or decay produces one of
 572 the neutral, long-lived SM particles (ν or γ), the particle is traced back to a DM source. For DM
 573 above GeV energies, there are very few SM processes that can produce particles with such a high
 574 energy. Seeing such a signal would almost certainly be an indication of the presence of dark matter.
 575 Fortunately, the universe provides us with the largest volume and lifetime ever for a particle physics
 576 experiment.

577 2.5 Sources for Indirect Dark Matter Searches

578 The first detection of DM relied on optical observations. Since then, we have developed new
 579 techniques to find DM dense regions. As described in Section 2.3.1, many DM dense regions were
 580 through observing galactic rotation curves. Our Milky Way galaxy is among DM dense regions

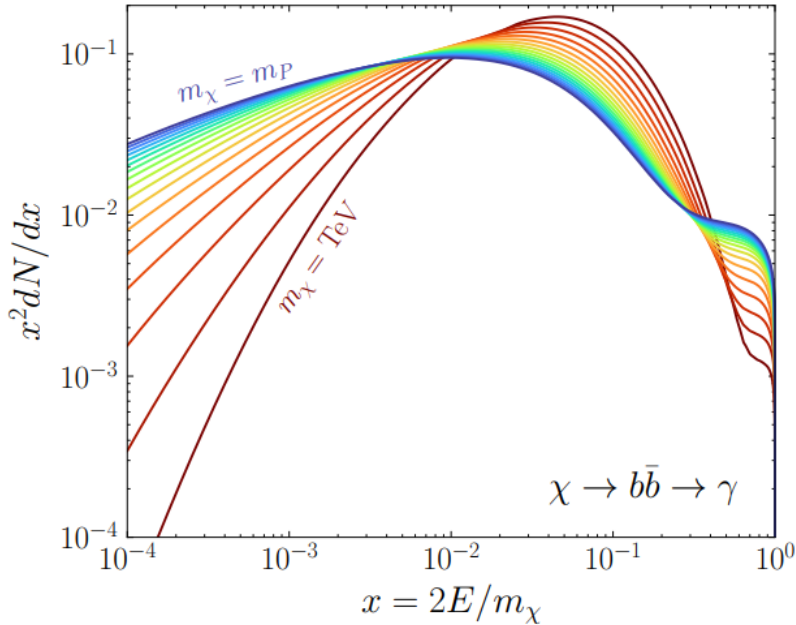


Figure 2.11 Dark Matter (DM) decay spectrum for $b\bar{b}$ initial state and γ final state. Redder spectra are for larger DM masses. Bluer spectra are light DM masses. x is a unitless factor defined as the ratio of the mass of DM, m_χ , and the final state particle energy E_γ . Figure from [19].

discovered, and it is the largest nearby DM dense region to look at. Additionally, the DM halo surrounding the Milky Way is clumpy [18]. There are regions in the DM halo of the Milky Way that have more DM than others that have captured gas over time. These sub-halos were dense enough to collapse gas and form stars. These apparent sub galaxies are known as dwarf spheroidal galaxies and are the main sources studied in this thesis. Each source type comes with different trade-offs. Galactic Center studies will be very sensitive to the assumed distribution of DM. The central DM density can vary substantially as demonstrated in Figure 2.12. At distances close to the center of the galaxy, or small r , the differences in DM densities can be 3-4 orders of magnitude. Searches toward the galactic center will therefore be quite sensitive to the assumed DM distribution.

Searches toward Dwarf Spheroidal Galaxies (dSph's) suffer from uncertainties in the DM density less than the galactic center studies. This is mostly from their diminutive size being smaller than the angular resolution of most γ -ray observatories [18]. The DM content dSph's are typically determined with the Virial theorem, Equation (2.1), and are usually majority DM [18] in mass. DSph's tend to be ideal sources to look at for DM searches. Their environments are quiet with little

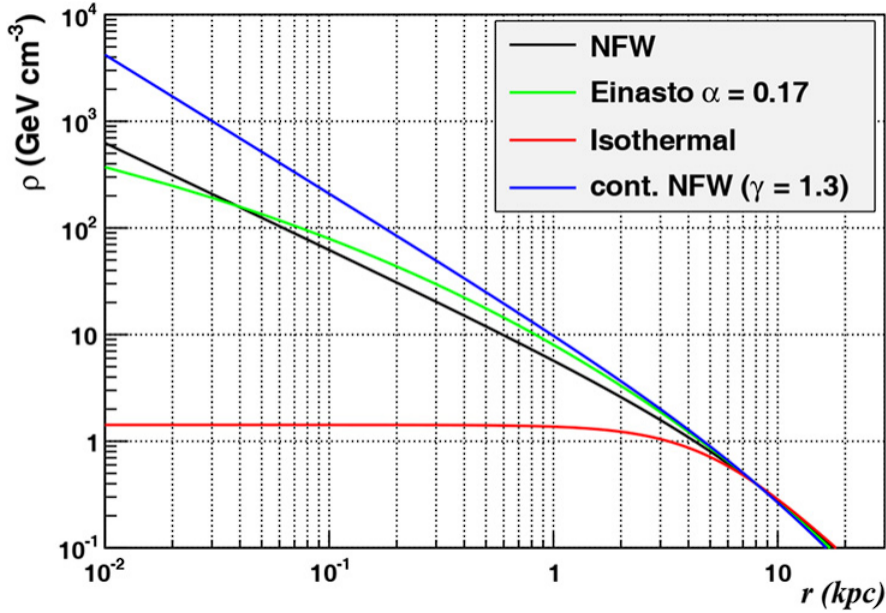


Figure 2.12 Different dark matter density profiles compared. Some models produce exceptionally large densities at small r [20].

595 astrophysical background. Unlike the galactic center, the most active components of dSph's are the
 596 stars within them versus a violent accretion disc around a black hole. All this together means that
 597 dSph's are among the best sources to look at for indirect DM searches. dSph's are the targets of
 598 focus for this thesis.

599 2.6 Multi-Messenger Dark Matter

600 Astrophysics entered a new phase in the past few decades that leverages our increasing sensitivity
 601 to SM channels and general relativity (GR). Up until the 21st century, astrophysical observations
 602 were performed with photons (γ) only. Astrophysics with this 'messenger' is fairly mature now.
 603 Novel observations of the universe have since only adjusted the sensitivity of the wavelength of
 604 light that is observed except at MeV energies. Gems like the CMB [10], and more have ultimately
 605 been observations of different wavelengths of light. Multi-messenger astrophysics proposes using
 606 other SM particles such the p^{+-} , or ν or gravitation waves predicted by general relativity.

607 The experiment LIGO had a revolutionary discovery in 2016 with the first detection of a binary
 608 black hole merger [21]. This opened the collective imagination to observing the universe through
 609 gravitational waves. There has also been a surge of interest in the neutrino (ν) sector. IceCube

610 demonstrated that we are sensitive to neutrinos in regions that correlate with significant photon
 611 emission like the galactic plane [22]. Neutrinos, like gravitational waves and light, travel mostly
 612 unimpeded from their source to our observatories. This makes pointing to the originating source
 613 of these messengers much easier than it is for cosmic rays which are deflected from their source by
 614 magnetic fields.

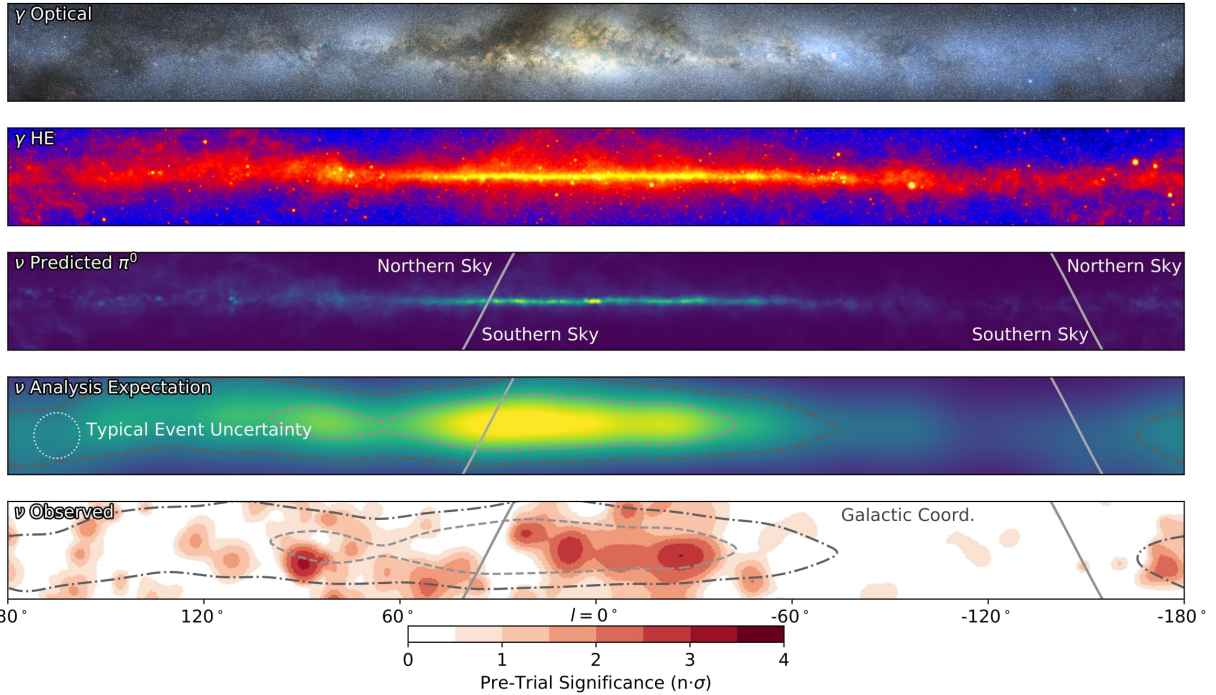


Figure 2.13 The Milky Way Galaxy in photons (γ) and neutrinos (ν) [22]. The Galactic center is at $l=0^\circ$ and is the brightest region in all panels. (top) An Optical color image of the Milky Way galaxy seen from Earth. Clouds of gas and dust obscure some light from stars. (2nd down) Integrated flux of γ -rays observed by the Fermi-LAT telescope [23]. (middle) Expected neutrino emission that corresponds with Fermi-LAT observations. (2nd up) Expected neutrino emission profile after considering detector systematics of IceCube. (bottom) Observed neutrino emission from region of the galactic plane. Substantial neutrino emission was detected.

615 The IceCube collaboration recently published a groundbreaking result of the Milky Way in
 616 neutrinos. The recent result from IceCube, shown in Figure 2.13, proves that we can make
 617 observations under different messenger regimes. The top two panels show the appearance of the
 618 galactic plane to different wavelengths of light. Some sources are more apparent in some panels,
 619 while others are not. This new channel is powerful because neutrinos are readily able to penetrate
 620 through gas and dust in the Milky Way. This new image also refines our understanding of how high

621 energy particles are produced. For example, the fit to IceCube data prefers neutrino production
 622 from the decay of π^0 [22].

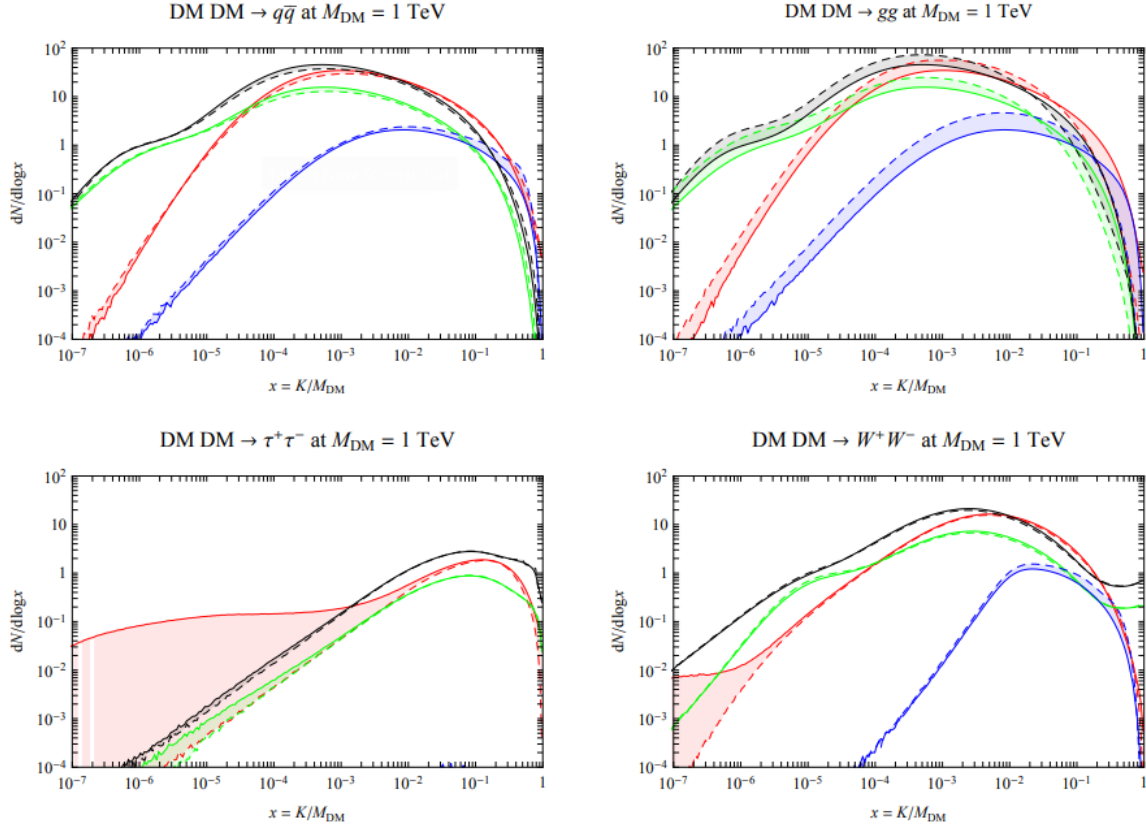


Figure 2.14 Dark Matter annihilation spectra for different final state particle and standard model annihilation channels [24]. Photons (red), e^\pm (green), \bar{p} (blue), ν (black).

623 Exposing our observations to more cosmic messengers greatly increases our sensitivity to
 624 rare processes. In the case of DM, Figure 2.14, there are many SM particles produced in DM
 625 annihilation. Among the final state fluxes are gammas and neutrinos. Charged particles are also
 626 produced however they would not likely make it to Earth since they will be deflected by magnetic
 627 fields between the source and Earth. This means observatories that can see the neutral messengers
 628 are especially good for DM searches and for combining data for a multi-messenger DM search.

CHAPTER 3

629 MULTIMESSENGER ASTROPHYSICS: DETECTING HIGH ENERGY NEUTRAL 630 MESSENGERS

631 3.1 Introduction

632 Before the 20th century, all astrophysics observations were optical in nature. We literally only
633 saw things with highly magnified optical observations. Then we discovered cosmic rays. cosmic
634 rays are charged particles, typically naked protons or H+. This was seen by Victor Hess in 19??.
635 Around the same time we discovered neutrinos from beta decay. Sometime around 1950 we started
636 to build neutrino detectors which were mostly sensitive to neutrinos from the sun. Finally, it was
637 theorized that compact objects like black holes and neutron stars would create waves in space-time
638 when they experience mergers or collisions.

639 In the 21st century, we have developed new observation techniques and detectors that are no only
640 sensitive to these four messengers - photons ([TODO: photon](#)), neutrinos ([TODO: nu](#)), Cosmic
641 Rays (CR), and Gravitational Wave (WV) - we're collect high energy versions of these events.
642 For the standad model particles, we're now sensitive to all messengers above the MeV eneryg
643 range. Additionally, the GW's were sensitive to are in the stellar mass black hole region and above
644 within our galactic neighborhood. This means were becoming sensitive to the fundamental physics
645 occuring within the universe and we can rely on the universe as a TeV+ particle accelerator. We
646 also have the abaility to correlate high energy events across messengers and gain new insights on
647 the processes that occur in our universe.

648 This thesis focuses on very high energy (VHE) gamma rays and neutrinos. These can both be
649 observed through the water cherenkov detection technique altho not exclusively. Methods on how
650 to detect and observe these neutral messengers are discussed Section 3.3 and Section 3.4

651 3.2 Charged Particles in a Medium

652 For high enery gamma-rays and neutrinos, we can exploit the same effect that charged particles
653 have with water. This effect is known as Cherenkov radiation. Cherenkov Radiation occurs when a
654 charged particle, usually electrons (e) or muons (μ), traverse a medium, like water, faster than the

655 speed of light in that medium. This is similar to sonic boom where an object moves through air
656 faster than the speed of sound in air. Cherenkov radiation can therefore be thought of as an 'optic
657 boom'. Many astro-particle physics experiments will use water as the medium as because water
658 has a unique set of properties ideal for charged particle tracking.



Figure 3.1 TODO: Show a nuclear reactor with cherenkov radiation[NEEDS A SOURCE][FACT CHECK THIS]

659 The frequency of light emitted due to cherenkov radiation follows the equation:

$$INSERT\ Cherenkov\ wavelength\ calc\ HERE. \quad (3.1)$$

660 The absorption spectra is shown in the following figure:

661 **3.3 Photons (γ)**

662 **3.4 Neutrinos (ν)**

663 **3.5 Opportunities to Combine for Dark Matter**



Figure 3.2 TODO: absorption spectrum of liquid and solid water[NEEDS A SOURCE][FACT CHECK THIS]

CHAPTER 4

664 **HIGH ALTITUDE WATER CHERENKOV (HAWC) OBSERVATORY**

665 **4.1 The Detector**

666 **4.2 Events Reconstruction and Data Acquisition**

667 **4.2.1 G/H Discrimination**

668 **4.2.2 Angle**

669 **4.2.3 Energy**

670 **4.3 Remote Monitoring**

671 **4.3.1 ATHENA Database**

672 **4.3.2 HOMER**

673

CHAPTER 5

ICECUBE NEUTRINO OBSERVATORY

674 **5.1 The Detector**

675 **5.2 Events Reconstruction and Data Acquisition**

676 **5.2.1 Angle**

677 **5.2.2 Energy**

678 **5.3 Northern Test Site**

679 **5.3.1 PIgeon remote dark rate testing**

680 **5.3.2 Bulkhead Construction**

CHAPTER 6

GLORY DUCK: MULTI-WAVELENGTH SEARCH FOR DARK MATTTER ANNIHILATION TOWARDS DWARF SPHEROIDAL GALAXIES

6.1 Introduction

The field of astrophysics now has several instruments and observatories sensitive to high energy gamma-rays. The energy sensitivity for the modern gamma-ray program spans many orders of magnitude. Figure 6.1 demonstrates these similar sensitivities across energies for the five experiments: Fermi-LAT, HAWC, HESS, MAGIC, and VERITAS.

Each of the five experiments featured in Figure 6.1 have independently searched for DM annihilation from dwarf spheroidal galaxies (dSph) and set limits. Intriguingly, there are regions of substantial overlap in their energy sensitivities. This clearly motivates an analysis that combines data from these five. Each experiment has unique gamma-ray detection methods and their weaknesses and strengths can be leveraged with each other. The HAWC gamma-ray observatory is extensively introduced in chapter 4, so it is not introduced here. A brief description of the remaining experiments are in the following paragraphs.

The Large Area Telescope (LAT) is a pair conversion telescope mounted on the NASA Fermi satellite in orbit \sim 550 km above the Earth [26]. LAT's field of view covers about 20% of the whole sky, and it sweeps the whole sky approximately every 3 hours. LAT's gamma-ray energy sensitivity ranges from 20 MeV up to 1 TeV. Previous DM searches towards dSphs using Fermi-LAT are published in [27] and [28]

The High Energy Spectroscopic System (HESS), Major Atmospheric Gamma Imaging Cherenkov (MAGIC), and Very Energetic Radiation Imaging Telescope Array System (VERITAS) are arrays of Imaging Atmospheric Cherenkov Telescopes (IACT). These telescopes observe the Cherenkov light emitted from gamma-ray showers in the Earth's atmosphere. The field of view for these telescopes is no larger than 5° with energy sensitivities ranging from 30 GeV up to 100 TeV [29, 30, 31]. IACTs are able to make precise observations in selected regions of the sky, however can only be operated in ideal dark conditions. HESS's observations of the dwarves

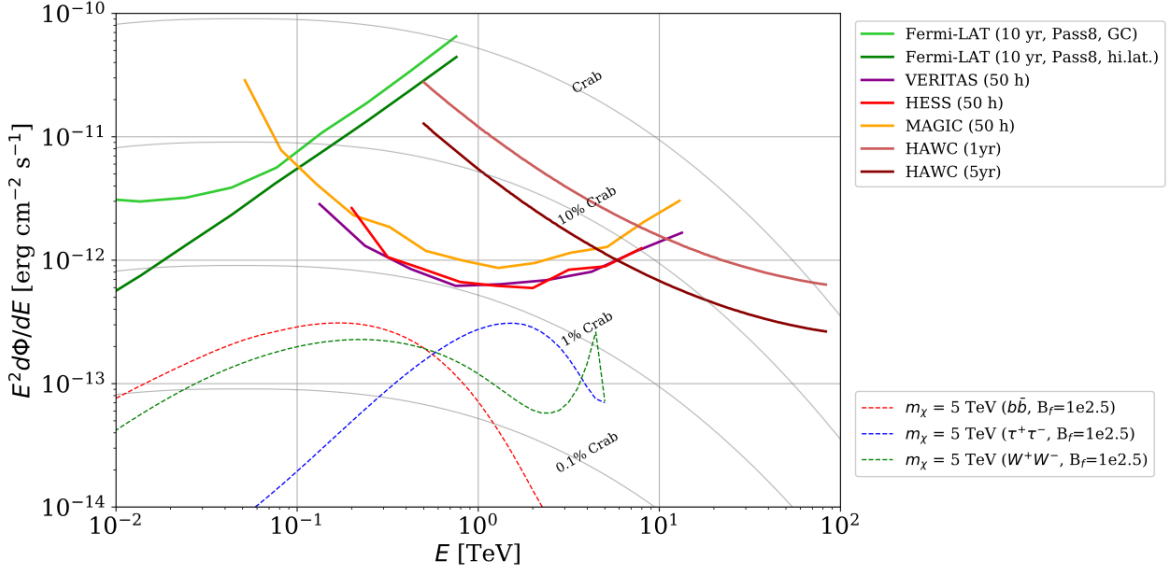


Figure 6.1 Sensitivities of five gamma-ray experiments compared to percentages of the Crab nebula’s emission and dark matter annihilation. Solid lines present estimated sensitivities to power law spectra [FACT CHECK THIS] for each experiment. Green lines are Fermi-LAT sensitivities where lighter green is the sensitivity to the galactic center and dark green is its sensitivity to higher declinations. Orange, red, and purple solid lines represent the MAGIC, HESS, and VERITAS 50 hour sensitivities respectively. The maroon and brown lines are the HAWC 1 year and 5 year sensitivities. Across four decades of gamma-ray energy, these experiments have similar sensitivities on the order 10^{-12} erg $\text{cm}^{-2}\text{s}^{-1}$. The dotted lines are estimated dark matter fluxes assuming $m_\chi = 5$ TeV DM annihilating to bottom quarks (red), tau leptons (blue), and W bosons (green). Faded gray lines outline percentage flux of the Crab nebula. Figure is an augmented version of [25]

707 Sculptor and Carina were between January 2008 and December 2009. HESS’s observations of
 708 Coma Berenices were from 2010 to 2013, and Fornax was observed in 2010 [32, 33, 34]. MAGIC
 709 provided deep observations of Segue1 between 2011 and 2013 [35]. MAGIC also provides data
 710 for three dwarves: Coma Berenices, Draco, and Ursa Major II where observations were made
 711 in: January - June 2019 [36], March - September 2018 [36], and 2014 - 2016 [37] respectively.
 712 VERITAS provided data for Boötes I, Draco, Segue 1, and Ursa Minor from 2009 to 2016 [38].

713 This chapter presents the Glory Duck analysis, the name given for the search for dark matter
 714 annihilation from dSph by combining data from the five gamma-ray observatories: Fermi-LAT,
 715 HAWC, HESS, MAGIC, and VERITAS. Specifically, the methods in analysis and modeling are
 716 presented for the HAWC gamma-ray observatory. This work was published to the Journal of
 717 Cosmology and Astroparticle Physics and presented at the International Cosmic Ray Conference

718 in 2019, 2021, and 2023 [39, 40, 41] and others.

719 **6.2 Dataset and Background**

720 This section enumerates the data and background methods used for HAWC’s study of dSphs.
721 Section 6.2.1 and Section 6.2.2 are most useful for fellow HAWC collaborators looking to replicate
722 the Glory Duck analysis.

723 **6.2.1 Itemized HAWC files**

- 724 • Detector Resolution: `response_aerie_svn_27754_systematics_best_mc_test_no`
725 `broadpulse_10pctlogchargesmearing_0.63qe_25kHzNoise_run5481_curvatu`
726 `re0_index3.root`
- 727 • Data Map: `maps-20180119/liff/maptree_1024.root`
- 728 • Spectral Dictionary: `DM_CirrelliSpectrum_dict_gammas.npy`
- 729 • Analysis wiki: https://private.hawc-observatory.org/wiki/index.php/Glory_Duck_Multi-Experiment_Dark_Matter_Search

731 **6.2.2 Software Tools and Development**

732 This analysis was performed using HAL and 3ML [42, 43] in Python version 2. I built software
733 to implement the *A Poor Particle Physicist Cookbook for Dark Matter Indirect Detection* (PPPC)
734 [44] DM spectral model and dSphs spatial model from [45] for HAWC analysis. A NumPy version
735 of this dictionary was made for both Py2 and Py3. The code base for creating this dictionary is
736 linked on my GitLab sandbox:

- 737 • Py2: [Dictionary Generator \(Deprecated\)](#)
- 738 • Py3: [PPPC2Dict](#)

739 The analysis was performed using the f_{hit} framework performed in the HAWC Crab paper
740 [42]. The Python2 NumPy dictionary file for gamma-ray final states is `dmCirSpecDict.npy`. The
741 corresponding Python3 file is `DM_CirrelliSpectrum_dict_gammas.npy`. These files can also

742 be used for decay channels and the PPPC describes how [44]. All other software used for data
743 analysis, DM profile generation, and job submission to SLURM are also kept in my sandbox for
744 [the Glory Duck](#) project.

745 **6.2.3 Data Set and Background Description**

746 The HAWC data maps used for this analysis contain 1017 days of data between runs 2104
747 (2014-11-26) and 7476 (2017-12-20). They were generated from pass 4.0 reconstruction. The
748 analysis is performed using the f_{hit} energy binning scheme with bins (1-9) similar to what was done
749 for the Crab and previous HAWC dSph analysis [42, 46]. Bin 0 was excluded as it has substantial
750 hadronic contamination and poor angular resolution.

751 This analysis was done on dSphs because of their large DM mass content relative to baryonic
752 mass. We consider the following to estimate the background to this study.

- 753 • The dSphs are small in HAWC’s field of view, so the analysis is not sensitive to large or small
754 scale anisotropies.
- 755 • The dSphs used in this analysis are off the galactic plane.
- 756 • The dSphs are baryonically faint relative to their expected dark matter content and are not
757 expected to contain high energy gamma-ray sources.

758 Therefor we make no additional assumptions on the background from our sources and use
759 HAWC’s standard direct integration method for background estimation [42]. It is possible for
760 gamma rays from DM annihilation to scatter in transit to HAWC via Inverse Compton Scattering
761 (ICS). This was investigated and its impact on the flux is basically zero. Supporting information
762 on this is in Section 6.7.1

763 **6.3 Analysis**

764 The expected differential photon flux from DM-DM annihilation to standard model particles,
765 $d\Phi_\gamma/dE_\gamma$, over solid angle, Ω is described by the familiar equation.

$$\frac{d\Phi_\gamma}{dE_\gamma} = \frac{\langle\sigma v\rangle}{8\pi m_\chi^2} \frac{dN_\gamma}{dE_\gamma} \times \int_{\text{source}} d\Omega \int_{l.o.s} \rho_\chi^2 dl(r, \theta') \quad (6.1)$$

766 Where $\langle \sigma v \rangle$ is the velocity weighted annihilation cross-section. $\frac{dN}{dE}$ is the expected differential
 767 number of photons produced at each energy per annihilation. m_χ is the rest mass of the supposed
 768 DM particle. ρ_χ is the DM density. J is the astrophysical J-factor and is defined as

$$J = \int d\Omega \int_{l.o.s} dl \rho_\chi^2(r, \theta') \quad (6.2)$$

769 l is the distance to the source from Earth. r is the radial distance from the center of the source. θ' is
 770 the half angle defining a cone containing the DM source. How each component is synthesized and
 771 considered for HAWC's analysis is presented in the following sections. Section 6.3.1 presents the
 772 particle physics model for DM annihilation. Section 6.3.2 presents the spatial distributions built
 773 for each dSph.

774 6.3.1 $\frac{dN_\gamma}{dE_\gamma}$ - Particle Physics Component

775 For these spectra, we import the PPPC with Electroweak (EW) corrections [44]. The spectrum
 776 is implemented as a model script in astromodels for 3ML. The EW corrections were previously not
 777 considered for HAWC and are significant for DM annihilating to EW coupled SM particles such
 778 as all leptons, and the γ , Z , and W bosons [46]. Figure 6.2 demonstrates the significance of EW
 779 corrections for W boson annihilation. Across EW SM channels, the gamma-ray spectra become
 780 harder than spectra without EW corrections. Tables from the PPPC were reformatted into Python
 781 NumPy dictionaries for collaboration-wide use. A class in astromodels was developed to include
 782 the EW correction from the PPPC and is aptly named `PPPCSpectra` within `DM_models.py`.

783 6.3.2 J - Astrophysical Component

784 The J-factor profiles for each source are imported from Geringer-Sameth (referred to with \mathcal{GS})
 785 [45]. These were pulled from the publication as $J(\theta)$, where θ is the angular separation from the
 786 center of the source. HAWC requires maps in terms of $\frac{dJ}{d\Omega}$, so the conversion from the maps was
 787 done in the following way...

788 First, convert the angular distances to solid angles

$$\Omega = 2 \cdot \pi(1 - \cos(\theta)) \quad (6.3)$$

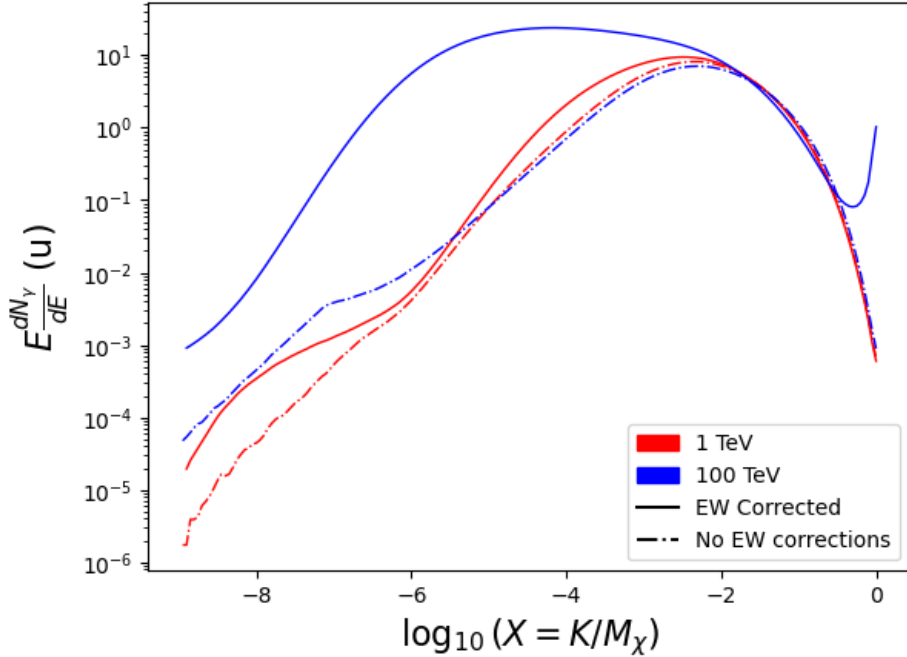


Figure 6.2 Effect of Electroweak (EW) corrections on expected DM annihilation spectrum for $\chi\chi \rightarrow W^-W^+$. Solid lines are spectral models that consider EW corrections. Dash-dot lines are spectral models without EW corrections. Red lines are models for $M_\chi = 1$ TeV. Blue lines represent models for $M_\chi = 100$ TeV. All models are sourced from the PPPC4DMID [44].

789 which reduces with a small angle approximation to $\pi\theta^2$. Next, the central difference for both the
 790 ΔJ and $\Delta\Omega$ value were calculated from the discretized $J(\theta)$ with the central difference stencil:

$$\Delta\phi_i = \phi_{i+1} - \phi_{i-1} \quad (6.4)$$

791 Where ϕ is either Ω or J . These were done separately in case the grid spacing in θ was not uniform.
 792 Finally, these lists are divided so that we are left with an approximation of the $dJ/d\Omega$ profile that
 793 is a function of θ . Admittedly, this is an approximation method for the map which introduces small
 794 errors compared to the true profile estimate. This was checked as a systematic against the author's
 795 profiling of the spatial distribution and is documented in Section 6.8.1.

796 With $\frac{dJ}{d\Omega}(\theta)$, a map is generated, first by filling in the north-east quadrant of the map. This
 797 quadrant is then reflected twice, vertically then horizontally, to fill the full map. Maps are then
 798 normalized by dividing the discrete 2D integral of the map. The 2D integral was a simple height

799 of bins, Newton's integral:

$$p^2 \cdot \sum_{i,j=0}^{N,M} \frac{dJ}{d\Omega}(\theta_{i,j}, \phi_{i,j}) \quad (6.5)$$

800 These maps are HEALpix maps with NSIDE 16384 and saved in the `.fits` format.

801 Another DM spatial distribution model from Bonnivard (\mathcal{B}) [47] was used for the Glory Duck
802 study. However, to save computational time, limits from \mathcal{GS} were scaled to \mathcal{B} instead of each
803 experiment performing a full study a second time. How these models compare is demonstrated
804 for each dSph in Figure 6.16 and Figure 6.17 Plots of these maps are provided for each source
805 in chapter A Examples of the two most impactful dSphs derived from \mathcal{GS} , Segue1 and Coma
806 Berenices are featured in Figure 6.3

807 6.3.3 Source Selection and Annihilation Channels

808 We use many of the dSphs presented in HAWC's previous dSph DM search [46]. HAWC's
809 sources for Glory Duck include Boötes I, Coma Berenices, Canes Venatici I + II, Draco, Hercules,
810 Leo I, II, + IV, Segue 1, Sextans, and Ursa Major I + II. A full description of all sources used
811 in Glory Duck is found in Table 6.1. Triangulum II was excluded from the Glory Duck analysis
812 because of large uncertainties in its J factor. Ursa Minor was excluded from HAWC's contribution
813 to the combination because the source extension model extended Ursa Minor beyond HAWC's field
814 of view. Ursa Minor was not expected to contribute significantly to the combined limit, so work
815 was not invested in a solution to include Ursa Minor.

816 This analysis improves on the previous HAWC dSph paper [46] in the following ways. Pre-
817 viously, the dSphs were treated and implemented as point sources. For this analysis, dSphs are
818 modeled and treated as extended source. The impact of this change with respect to the upper limit
819 is source dependent and is explored in Section 6.7.2. Previously, the particle physics model used for
820 gamma-ray spectra from DM annihilation did not have EW corrections where the PPPC includes
821 them. Finally, the gamma-ray ray dataset is much larger. The study performed here analyzes over
822 1000 days of data compared to 507.

823 The SM annihilation channels probed for the Glory Duck combination include $b\bar{b}$, $e\bar{e}$, $\mu\bar{\mu}$, $\tau\bar{\tau}$,
824 $t\bar{t}$, W^+W^- , and ZZ . A summary of all sources, with a description of each experiments' sensitivity

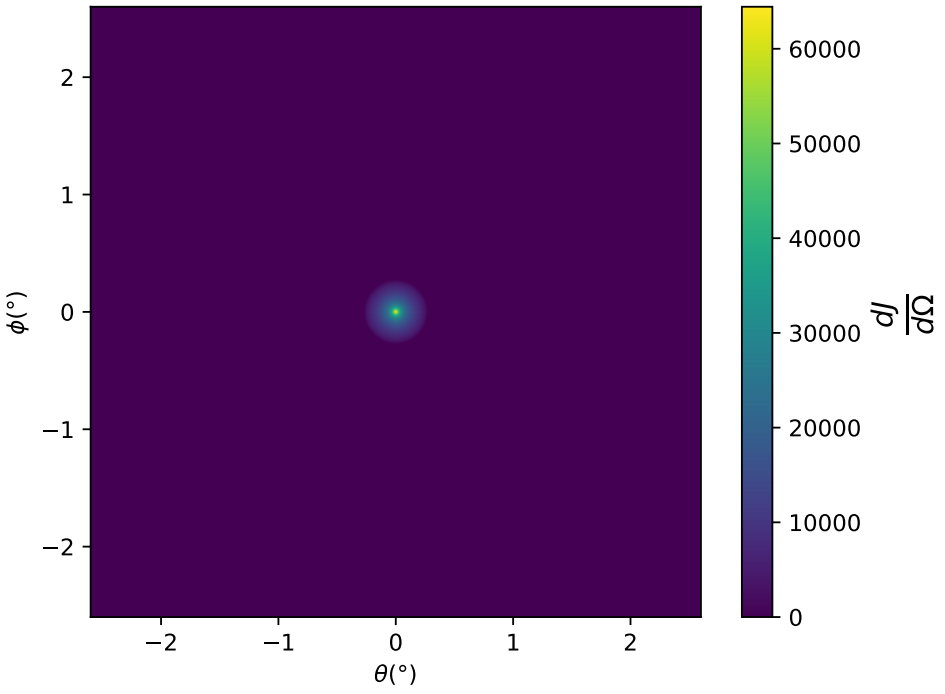
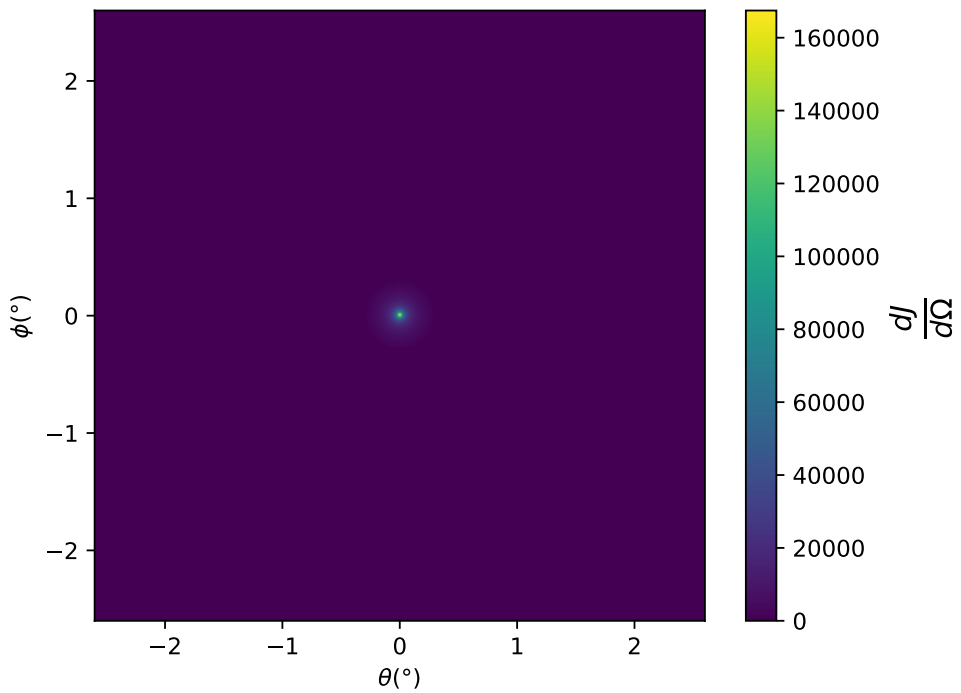


Figure 6.3 $\frac{dJ}{d\Omega}$ maps for Segue1 (top) and Coma Berenices (bottom). Origin is centered on the specific dwarf spheroidal galaxies (dSph). X and Y axes are the angular separation from the center of the dwarf. Plots of the remaining 11 dSph HAWC studied are linked in Fig. A.1.

Table 6.1 Summary of the relevant properties of the dSphs used in the present work. Column 1 lists the dSphs. Columns 2 and 3 present their heliocentric distance and galactic coordinates, respectively. Columns 4 and 5 report the J -factors of each source given from the \mathcal{GS} and \mathcal{B} independent studies and their estimated $\pm 1\sigma$ uncertainties. The values $\log_{10} J$ (\mathcal{GS} set) [45] correspond to the mean J -factor values for a source extension truncated at the outermost observed star. The values $\log_{10} J$ (\mathcal{B} set) [47] are provided for a source extension at the tidal radius of each dSph. **Bolded sources are within HAWC's field of view and provided to the Glory Duck analysis.**

Name	Distance (kpc)	l, b ($^{\circ}$)	$\log_{10} J$ (\mathcal{GS} set) $\log_{10}(\text{GeV}^2 \text{cm}^{-5} \text{sr})$	$\log_{10} J$ (\mathcal{B} set) $\log_{10}(\text{GeV}^2 \text{cm}^{-5} \text{sr})$
Boötes I	66	358.08, 69.62	$18.24^{+0.40}_{-0.37}$	$18.85^{+1.10}_{-0.61}$
Canes Venatici I	218	74.31, 79.82	$17.44^{+0.37}_{-0.28}$	$17.63^{+0.50}_{-0.20}$
Canes Venatici II	160	113.58, 82.70	$17.65^{+0.45}_{-0.43}$	$18.67^{+1.54}_{-0.97}$
Carina	105	260.11, -22.22	$17.92^{+0.19}_{-0.11}$	$18.02^{+0.36}_{-0.15}$
Coma Berenices	44	241.89, 83.61	$19.02^{+0.37}_{-0.41}$	$20.13^{+1.56}_{-1.08}$
Draco	76	86.37, 34.72	$19.05^{+0.22}_{-0.21}$	$19.42^{+0.92}_{-0.47}$
Fornax	147	237.10, -65.65	$17.84^{+0.11}_{-0.06}$	$17.85^{+0.11}_{-0.08}$
Hercules	132	28.73, 36.87	$16.86^{+0.74}_{-0.68}$	$17.70^{+1.08}_{-0.73}$
Leo I	254	225.99, 49.11	$17.84^{+0.20}_{-0.16}$	$17.93^{+0.65}_{-0.25}$
Leo II	233	220.17, 67.23	$17.97^{+0.20}_{-0.18}$	$18.11^{+0.71}_{-0.25}$
Leo IV	154	265.44, 56.51	$16.32^{+1.06}_{-1.70}$	$16.36^{+1.44}_{-1.65}$
Leo V	178	261.86, 58.54	$16.37^{+0.94}_{-0.87}$	$16.30^{+1.33}_{-1.16}$
Leo T	417	214.85, 43.66	$17.11^{+0.44}_{-0.39}$	$17.67^{+1.01}_{-0.56}$
Sculptor	86	287.53, -83.16	$18.57^{+0.07}_{-0.05}$	$18.63^{+0.14}_{-0.08}$
Segue I	23	220.48, 50.43	$19.36^{+0.32}_{-0.35}$	$17.52^{+2.54}_{-2.65}$
Segue II	35	149.43, -38.14	$16.21^{+1.06}_{-0.98}$	$19.50^{+1.82}_{-1.48}$
Sextans	86	243.50, 42.27	$17.92^{+0.35}_{-0.29}$	$18.04^{+0.50}_{-0.28}$
Ursa Major I	97	159.43, 54.41	$17.87^{+0.56}_{-0.33}$	$18.84^{+0.97}_{-0.43}$
Ursa Major II	32	152.46, 37.44	$19.42^{+0.44}_{-0.42}$	$20.60^{+1.46}_{-0.95}$
Ursa Minor	76	104.97, 44.80	$18.95^{+0.26}_{-0.18}$	$19.08^{+0.21}_{-0.13}$

825 to the source, is provided in Table 6.2.

826 6.4 Likelihood Methods

827 6.4.1 HAWC Likelihoods

828 For every analysis bin in energy, f_{hit} bins (1-9), and location, we can expect N signal events and
829 B background events. The expected number of excess signal events from dark matter annihilation,

Table 6.2 Summary of dSph observations by each experiment used in this work. A ‘-’ indicates the experiment did not observe the dSph for this study. For Fermi-LAT, the exposure at 1 GeV is given. For HAWC, $|\Delta\theta|$ is the absolute difference between the source declination and HAWC latitude. HAWC is more sensitive to sources with smaller $|\Delta\theta|$. For IACTs, we show the zenith angle range, the total exposure, the energy range, the angular radius θ of the signal or ON region, the ratio of exposures between the background-control (OFF) and signal (ON) regions (τ), and the significance of gamma-ray excess in standard deviations, σ .

Source name	Fermi-LAT	HAWC	H.E.S.S, MAGIC, VERITAS						
	Exposure (10^{11} s m 2)	$ \Delta\theta $ ($^\circ$)	IACT	Zenith ($^\circ$)	Exposure (h)	Energy range (GeV)	θ ($^\circ$)	τ	S (σ)
Boötes I	2.6	4.5	VERITAS	15 – 30	14.0	100–41000	0.10	8.6	-1.0
Canes Venatici I	2.9	14.6	–	–	–	–	–	–	–
Canes Venatici II	2.9	15.3	–	–	–	–	–	–	–
Carina	3.1	–	H.E.S.S.	27 – 46	23.7	310 – 70000	0.10	18.0	-0.3
Coma Berenices	2.7	4.9	H.E.S.S.	47 – 49	11.4	550 – 70000	0.10	14.4	-0.4
Draco	3.8	38.1	MAGIC	5 – 37	49.5	60 – 10000	0.17	1.0	–
			MAGIC	29 – 45	52.1	70 – 10000	0.22	1.0	–
			VERITAS	25 – 40	49.8	120 – 70000	0.10	9.0	-1.0
Fornax	2.7	–	H.E.S.S.	11 – 25	6.8	230 – 70000	0.10	45.5	-1.5
Hercules	2.8	6.3	–	–	–	–	–	–	–
Leo I	2.5	6.7	–	–	–	–	–	–	–
Leo II	2.6	3.1	–	–	–	–	–	–	–
Leo IV	2.4	19.5	–	–	–	–	–	–	–
Leo V	2.4	–	–	–	–	–	–	–	–
Leo T	2.6	–	–	–	–	–	–	–	–
Sculptor	2.7	–	H.E.S.S.	10 – 46	11.8	200 – 70000	0.10	19.8	-2.2
Segue I	2.5	2.9	MAGIC	13 – 37	158.0	60 – 10000	0.12	1.0	-0.5
			VERITAS	15 – 35	92.0	80 – 50000	0.10	7.6	0.7
Segue II	2.7	–	–	–	–	–	–	–	–
Sextans	2.4	20.6	–	–	–	–	–	–	–
Ursa Major I	3.4	32.9	–	–	–	–	–	–	–
Ursa Major II	4.0	44.1	MAGIC	35 – 45	94.8	120 – 10000	0.30	1.0	-2.1
Ursa Minor	4.1	–	VERITAS	35 – 45	60.4	160 – 93000	0.10	8.4	-0.1

830 S , is estimated by convolving Equation (6.1) with HAWC's energy response and pixel point spread
 832 functions. I then compute the test statistic (TS) with the log-likelihood ratio test,

$$\text{TS} = -2 \ln \left(\frac{\mathcal{L}_0}{\mathcal{L}^{\max}} \right) \quad (6.6)$$

833 where \mathcal{L}_0 is the null hypothesis, or no DM emission, likelihood. \mathcal{L}^{\max} is the best fit signal
 834 hypothesis where $\langle \sigma v \rangle$ maximizes the likelihood. We calculate the likelihood of each source and
 835 model, assuming events are Poisson distributed, with

$$\mathcal{L} = \prod_i \frac{(B_i + S_i)^{N_i} e^{-(B_i + S_i)}}{N_i!} \quad (6.7)$$

836 where S_i is the sum of expected number of signal counts. B_i is the number of background counts
 837 observed. N_i is the total number of counts.

838 I also calculate an upper limit on $\langle \sigma v \rangle$ by calculating the 95% confidence level (CL). For the
 839 CL, we define a parameter, TS_{95} , as

$$\text{TS}_{95} \equiv \sum_{\text{bins}} \left[2N \ln \left(1 + \frac{\epsilon S_{\text{ref}}}{B} \right) - 2\epsilon S_{\text{ref}} \right] \quad (6.8)$$

840 where the expected signal counts from a dSph is scaled by ϵ . S_{ref} is the expected number of excess
 841 counts in a bin from DM emission from a dSph with a corresponding annihilation cross-section,
 842 $\langle \sigma v \rangle$. We scan ϵ such that

$$2.71 = \text{TS}_{\max} - \text{TS}_{95} \quad (6.9)$$

843 6.4.2 Glory Duck Joint Likelihood

844 The joint likelihood for the 5-experiment combination was done similarly as Section 6.4.1. We
 845 calculate upper limits on $\langle \sigma v \rangle$ from the TS, Eq. (6.6), and define the likelihood ratio more generally

$$\lambda(\langle \sigma v \rangle | \mathcal{D}_{\text{dSphs}}) = \frac{\mathcal{L}(\langle \sigma v \rangle; \hat{\nu} | \mathcal{D}_{\text{dSphs}})}{\mathcal{L}(\widehat{\langle \sigma v \rangle}; \hat{\nu} | \mathcal{D}_{\text{dSphs}})} \quad (6.10)$$

846 $\mathcal{D}_{\text{dSphs}}$ is the totality of observations across experiments and dSphs. ν are the nuisance parameters
 847 which are the J factors in this study. $\widehat{\langle \sigma v \rangle}$ and $\hat{\nu}$ are the respective estimate that maximize \mathcal{L}
 848 globally. Finally, $\hat{\nu}$ is the set of nuisance parameters that maximize \mathcal{L} for a fixed value of $\langle \sigma v \rangle$.

849 The *complete* joint likelihood, \mathcal{L} that encompasses all observations from all instruments and
 850 dSphs can be factorized into *partial* functions for each dSph l (with $\mathcal{L}_{\text{dSph},l}$) and its J factor (\mathcal{J}_l):

$$\mathcal{L} (\langle \sigma v \rangle; \nu | \mathcal{D}_{\text{dSphs}}) = \prod_{l=1}^{N_{\text{dSphs}}} \mathcal{L}_{\text{dSph},l} (\langle \sigma v \rangle; J_l, \nu_l | \mathcal{D}_l) \times \mathcal{J}_l (J_l | J_{l,\text{obs}}, \sigma_{\log J_l}). \quad (6.11)$$

851 For this study, $N_{\text{dSphs}} = 20$ is the number of dSphs studied. \mathcal{D}_l are the gamma-ray observations
 852 of dSph, l . ν_l are the nuisance parameters modifying the gamma-ray observations of dSph, l ,
 853 but excludes \mathcal{J}_l . \mathcal{J}_l is the J factor for dSph, l , as defined in Equation (6.2), and it is a nuisance
 854 parameter whose value is unknown. $\log_{10} J_{l,\text{obs}}$ and $\sigma_{\log J_l}$ are obtained from fitting a log-normal
 855 function of $J_{l,\text{obs}}$ to the posterior distribution of J_l [48]. $\log_{10} J_{l,\text{obs}}$ and $\sigma_{\log J_l}$ values are provided
 856 in Table 6.1. The term \mathcal{J}_l constraining J_l is written as:

$$\mathcal{J}_l (J_l | J_{l,\text{obs}}, \sigma_{\log J_l}) = \frac{1}{\ln(10) J_{l,\text{obs}} \sqrt{2\pi} \sigma_{\log J_l}} \exp\left(-\frac{(\log_{10} J_l - \log_{10} J_{l,\text{obs}})^2}{2\sigma_{\log J_l}^2}\right). \quad (6.12)$$

857 Both the \mathcal{GS} and \mathcal{B} , displayed in Table 6.1, sets of J factors are used in this analysis. Equation (6.12)
 858 is also normalized, so it can also be interpreted as a probability density function (PDF) for $J_{l,\text{obs}}$.
 859 From Equation (6.1), we can also see that $\langle \sigma v \rangle$ and J_l are degenerate when computing $\mathcal{L}_{\text{dSph},l}$.
 860 Therefore, as noted in [49], it is sufficient to compute $\mathcal{L}_{\text{dSph},l}$ versus $\langle \sigma v \rangle$ for a fixed value of J_l .
 861 We used $J_{l,\text{obs}}(\mathcal{GS})$ reported in Tab. 6.1, in order to perform the profile of \mathcal{L} with respect to J_l .
 862 The degeneracy implies that for any $J'_l \neq J_{l,\text{obs}}$ (in practice in our case we used $J'_l = J_{l,\text{obs}}(\mathcal{B})$ to
 863 compute results from a different set of J factors):

$$\mathcal{L}_{\text{dSph},l} (\langle \sigma v \rangle; J'_l, \nu_l | \mathcal{D}_l) = \mathcal{L}_{\text{dSph},l} \left(\frac{J'_l}{J_{l,\text{obs}}} \langle \sigma v \rangle; J_{l,\text{obs}}, \nu_l | \mathcal{D}_l \right), \quad (6.13)$$

864 which is a straightforward rescaling operation that reduces the computational needs of the profiling
 865 operation since:

$$\mathcal{L} (\langle \sigma v \rangle; \hat{\nu} | \mathcal{D}_{\text{dSphs}}) = \prod_{l=1}^{N_{\text{dSphs}}} \max_{J_l} \left[\mathcal{L}_{\text{dSph},l} (\langle \sigma v \rangle; J_l, \hat{\nu}_l | \mathcal{D}_l) \times \mathcal{J}_l (J_l | J_{l,\text{obs}}, \sigma_{\log J_l}) \right]. \quad (6.14)$$

866 In addition, Eq. (6.13) enables the combination of data from different gamma-ray instruments and
 867 observed dSphs via tabulated values of $\mathcal{L}_{\text{dSph},l}$, or equivalently of λ from Eq. (6.10) as was done in

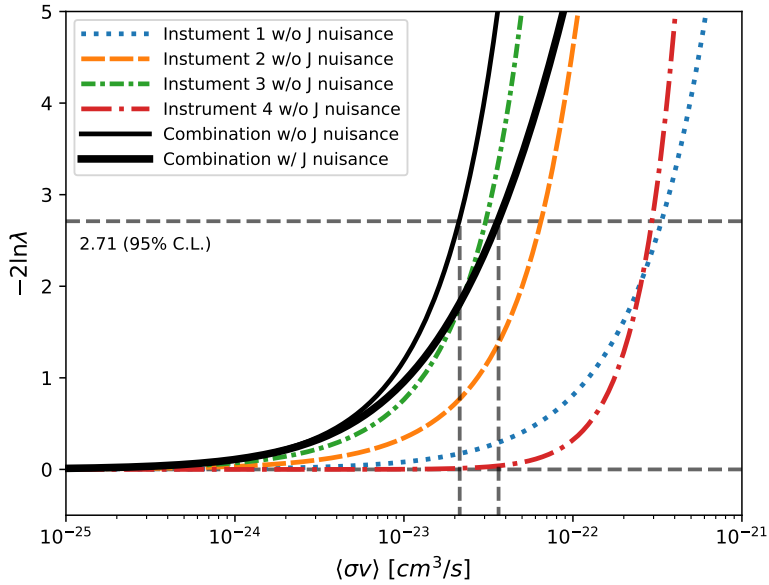


Figure 6.4 Illustration of the combination technique showing a comparison between $-2 \ln \lambda$ provided by four instruments (colored lines) from the observation of the same dSph without any J nuisance and their sum, *i.e.* the resulting combined likelihood (thin black line). According to the test statistics of Equation (6.6), the intersection of the likelihood profiles with the line $-2 \ln \lambda = 2.71$ indicates the 95% C.L. upper limit on $\langle \sigma v \rangle$. The combined likelihood (thin black line) shows a smaller value of upper limit on $\langle \sigma v \rangle$ than those derived by individual instruments. We also show how the uncertainties on the J factor effects the combined likelihood and degrade the upper limit on $\langle \sigma v \rangle$ (thick black line). All likelihood profiles are normalized so that the global minimum $\widehat{\langle \sigma v \rangle}$ is 0. We note that each profile depends on the observational conditions in which a target object was observed. The sensitivity of a given instrument can be degraded and the upper limits less constraining if the observations are performed in non-optimal conditions such as a high zenith angle or a short exposure time.

868 this work, versus $\langle \sigma v \rangle$. $\mathcal{L}_{dSph,l}$ is computed for a fixed value of J_l and profiled with respect to all
 869 instrumental nuisance parameters ν_l , these nuisance parameters are discussed in more detail below.
 870 These values are produced by each detector independently and therefore there is no need to share
 871 sensitive low-level information used to produce them, such as event lists. Figure 6.4 illustrates the
 872 multi-instrument combination technique used in this study with a comparison of the upper limit
 873 on $\langle \sigma v \rangle$ obtained from the combination of the observations of four experiments towards one dSph
 874 versus the upper limit from individual instruments. It also shows graphically the effect of the
 875 J -factor uncertainty on the combined observations.

876 The *partial* joint likelihood function for gamma-ray observations of each dSph ($\mathcal{L}_{dSph,l}$) is

written as the product of the likelihood terms describing the $N_{\text{exp},l}$ observations performed with any of our observatories:

$$\mathcal{L}_{\text{dSph},l} (\langle \sigma v \rangle; J_l, \nu_l | \mathcal{D}_l) = \prod_{k=1}^{N_{\text{exp},l}} \mathcal{L}_{lk} (\langle \sigma v \rangle; J_l, \nu_{lk} | \mathcal{D}_{lk}), \quad (6.15)$$

where each \mathcal{L}_{lk} term refers to an observation of the l -th dSph with associated k -th instrument responses. $N_{\text{exp},l}$ varies from dSph to dSph and can be inferred from Table 6.2.

Each collaboration separately analyzes their data for \mathcal{D}_{lk} corresponding to dSph l and gamma-ray detector k , using as many common assumptions as possible in the analysis. HAWC’s treatment was described earlier in Section 6.4.1 whereas the specifics of the remaining experiments is left to the publication. We compute the values for the likelihood functions \mathcal{L}_{lk} (see Eq. (6.15)) for a fixed value of J_l and profile over the rest of the nuisance parameters ν_{lk} . Then, values of λ from Eq. (6.10) are computed as a function of $\langle \sigma v \rangle$, and shared using a common format. Results are computed for seven annihilation channels, W^+W^- , ZZ , $b\bar{b}$, $t\bar{t}$, e^+e^- , $\mu^+\mu^-$, and $\tau^+\tau^-$ over 62 m_χ values between 5 GeV and 100 TeV provided in [44]. The $\langle \sigma v \rangle$ range is defined between 10^{-28} and $10^{-18} \text{cm}^3 \cdot \text{s}^{-1}$, with 1001 logarithmically spaced values. The likelihood combination, i.e. Equation (6.11), and profile over the J -factor to compute the profile likelihood ratio λ , Equation (6.10), are carried out with two different public analysis software packages, namely `gLike` [50] and `LklCom` [51], that provide the same results [52].

As mentioned previously, each experiment computes the \mathcal{L}_{lk} from Equation (6.10) differently. The remainder of this section highlights the differences in this calculation across the experiments. Four experiments, namely *Fermi*-LAT, H.E.S.S., HAWC and MAGIC, use a binned likelihood to compute the \mathcal{L}_{lk} . For these experiments, for each observation \mathcal{D}_{lk} of a given dSph l carried out using a given gamma-ray detector k , the binned likelihood function is:

$$\mathcal{L}_{lk} (\langle \sigma v \rangle; J_l, \nu_{lk} | \mathcal{D}_{lk}) = \prod_{i=1}^{N_E} \prod_{j=1}^{N_P} \left[\mathcal{P}(s_{lk,ij}(\langle \sigma v \rangle, J_l, \nu_{lk}) + b_{lk,ij}(\nu_{lk}) | N_{lk,ij}) \right] \times \mathcal{L}_{lk,\nu} (\nu_{lk} | \mathcal{D}_{\nu_{lk}}) \quad (6.16)$$

where N_E and N_P are the number of considered bins in reconstructed energy and arrival direction, respectively; \mathcal{P} represents a Poisson PDF for the number of gamma-ray candidate events $N_{lk,ij}$

900 observed in the i -th bin in energy and j -th bin in arrival direction, when the expected number is
 901 the sum of the expected mean number of signal events s_{ij} (produced by DM annihilation) and of
 902 background events b_{ij} ; $\mathcal{L}_{lk,\nu}$ is the likelihood term for the extra ν_{lk} nuisance parameters that vary
 903 from one instrument k to another. The expected counts for signal events s_{ij} for a given dSph l and
 904 detector k is given by:

$$s_{ij}(\langle\sigma\nu\rangle, J) = \int_{E'_{\min,i}}^{E'_{\max,i}} dE' \int_{P'_{\min,j}}^{P'_{\max,j}} d\Omega' \int_0^\infty dE \int_{\Delta\Omega_{tot}} d\Omega \int_0^{T_{\text{obs}}} dt \frac{d^2\Phi(\langle\sigma\nu\rangle, J)}{dEd\Omega} \text{IRF}(E', P' | E, P, t) \quad (6.17)$$

905 where E' and E are the reconstructed and true energies, P' and P the reconstructed and true
 906 arrival directions; $E'_{\min,i}$, $P'_{\min,j}$, $E'_{\max,i}$, and $P'_{\max,j}$ are their lower and upper limits of the i -th
 907 energy bin and the j -th arrival direction bin; T_{obs} is the (dead-time corrected) total observation
 908 time; t is the time along the observations; $d^2\Phi/dEd\Omega$ is the DM flux in the source region (see
 909 Equation (6.1)); and $\text{IRF}(E', P' | E, P, t)$ is the IRF, which can be factorized as the product of the
 910 effective collection area of the detector $A_{\text{eff}}(E, P, t)$, the PDFs for the energy estimator $f_E(E' | E, t)$,
 911 and arrival direction $f_P(P' | E, P, t)$ estimators. Note that for Fermi-LAT, HAWC, MAGIC, and
 912 VERITAS the effect of the finite angular resolution is taken into account through the convolution
 913 of $d\Phi/dEd\Omega$ with f_P in Equation (6.17), whereas in the cases of H.E.S.S. f_P is approximated by a
 914 delta function. This approximation has been made in order to maintain compatibility of the result
 915 with what has been previously published. The difference introduced by this approximation is $< 5\%$
 916 for all considered dSphs. A more comprehensive review of the differences between the analyses of
 917 different instruments can be found in [25].

918 6.5 HAWC Results

919 13 of the 20 dSphs considered for the Glory Duck analysis are within HAWC's field of view.
 920 These dSph are analyzed for emission from DM annihilation according to the likelihood method
 921 described in Section 6.4. The 13 likelihood profiles are then stacked to synthesize a combined
 922 limit on the dark matter cross-section, $\langle\sigma\nu\rangle$. This combination is done for the 7 SM annihilation
 923 channels used in the Glory Duck analysis. Figure 6.5 shows the combined limit for all annihilation
 924 channels with HAWC only observations. We also perform 300 studies of Poisson trials on the

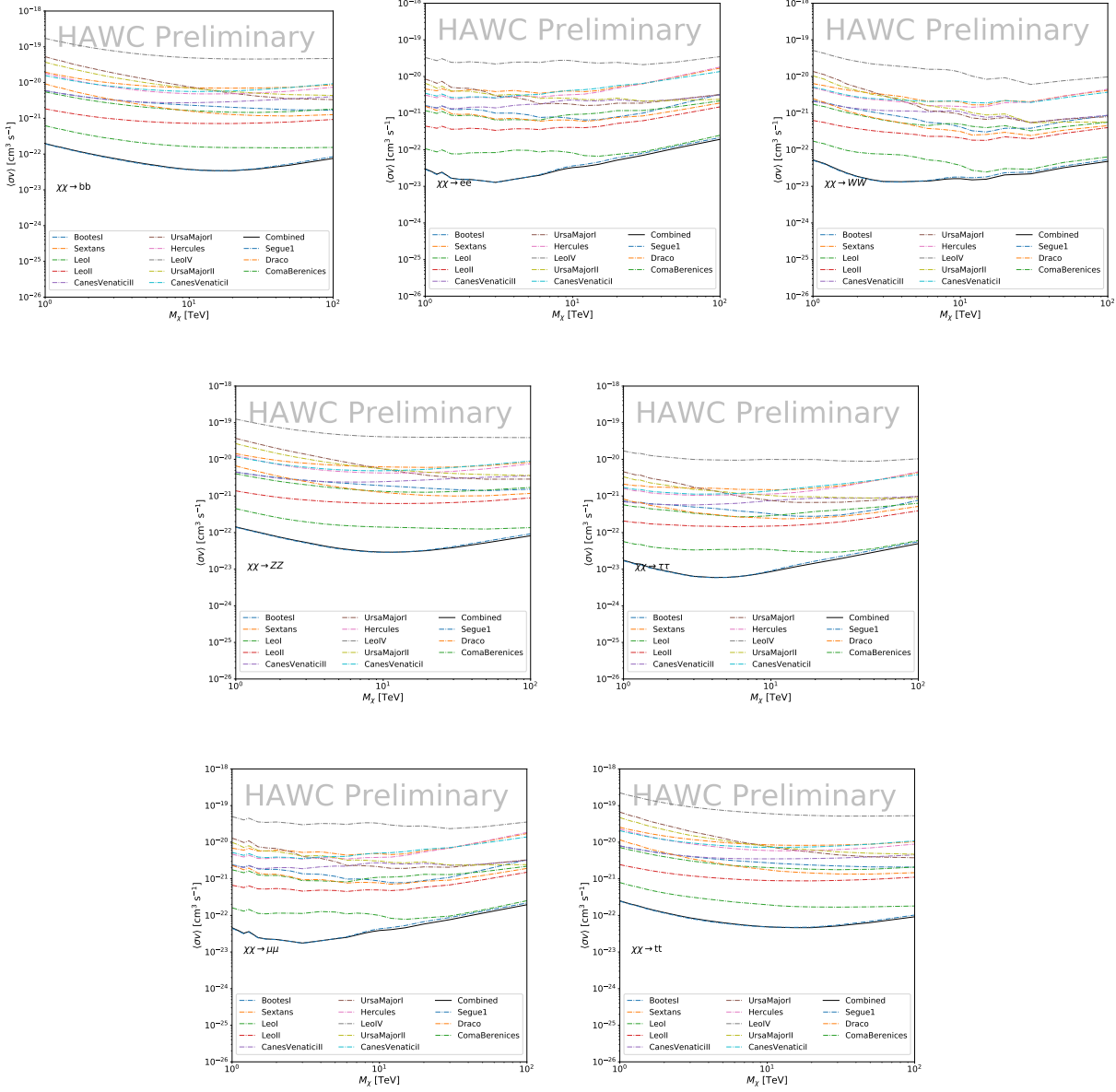


Figure 6.5 HAWC upper limits at 95% confidence level on $\langle\sigma v\rangle$ versus DM mass for seven annihilation channels, using the set of J -factors from Ref. [53]. The solid line represents the observed combined limit. Dashed lines represent limits from individual dSphs.

background. These trials are used to produce HAWC Brazil bands which were shared with the other collaborators for combined Brazil Bands. The results on fitting to HAWC's Poisson trials of the DM hypothesis is shown in Figure 6.7 for all the DM annihilation channels studied for Glory Duck.

No DM was found in HAWC observations. HAWC's limits are dominated by the dSphs Segue1

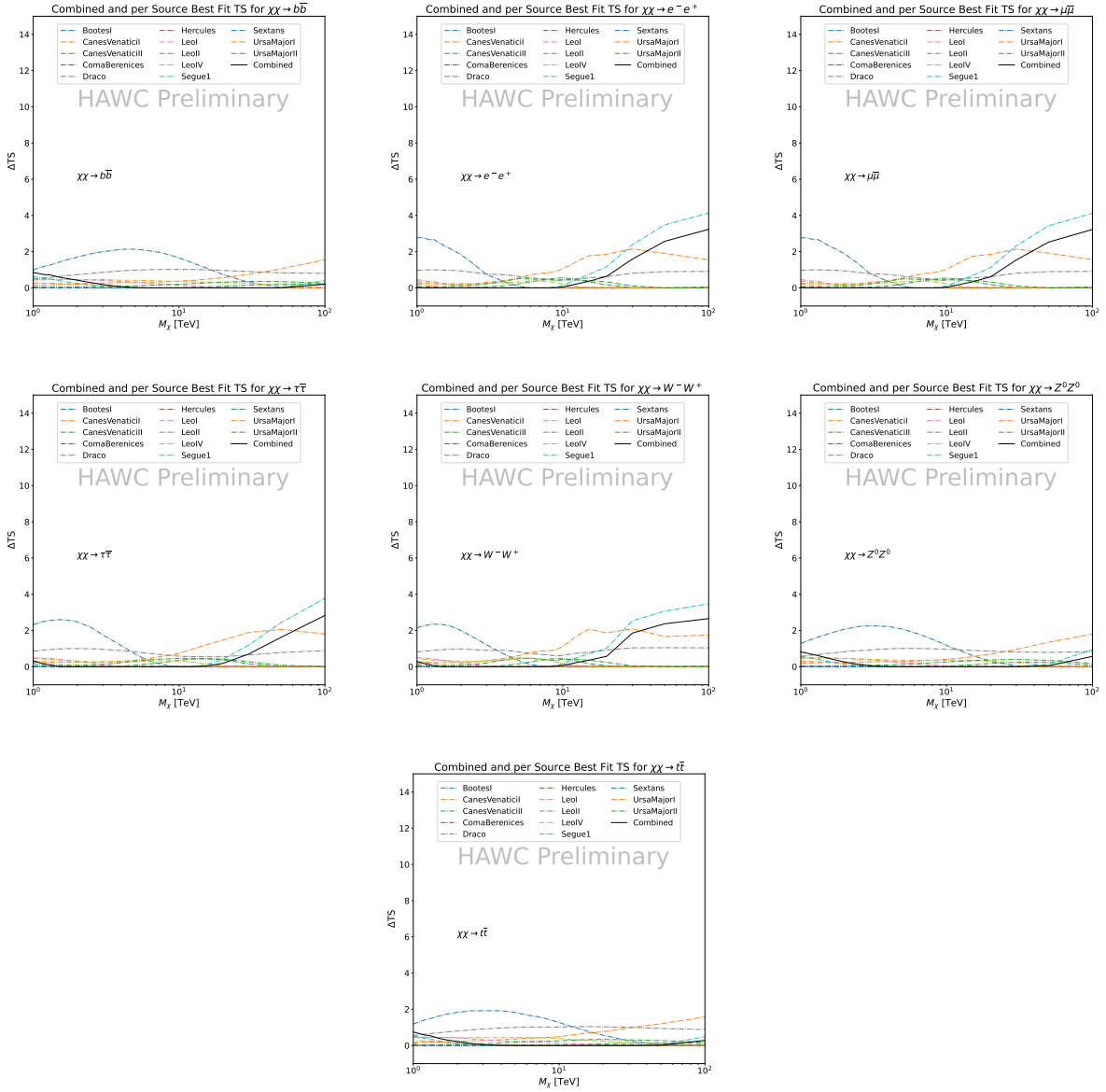


Figure 6.6 HAWC TS values for best fit $\langle \sigma v \rangle$ versus m_χ for seven SM annihilation channels with J factors from \mathcal{GS} . The solid black line shows the combined best fit TS values. The colored, dashed lines are the TS values for each of the 13 sources HAWC studied.

and Coma Berenices. The remaining 11 dSphs do not contribute significantly to the limit because they are at high zenith and/or have much smaller J factors. Even though some remaining dSphs have large J factors, they are towards the edge of HAWC's field of view where HAWC analysis is less sensitive.

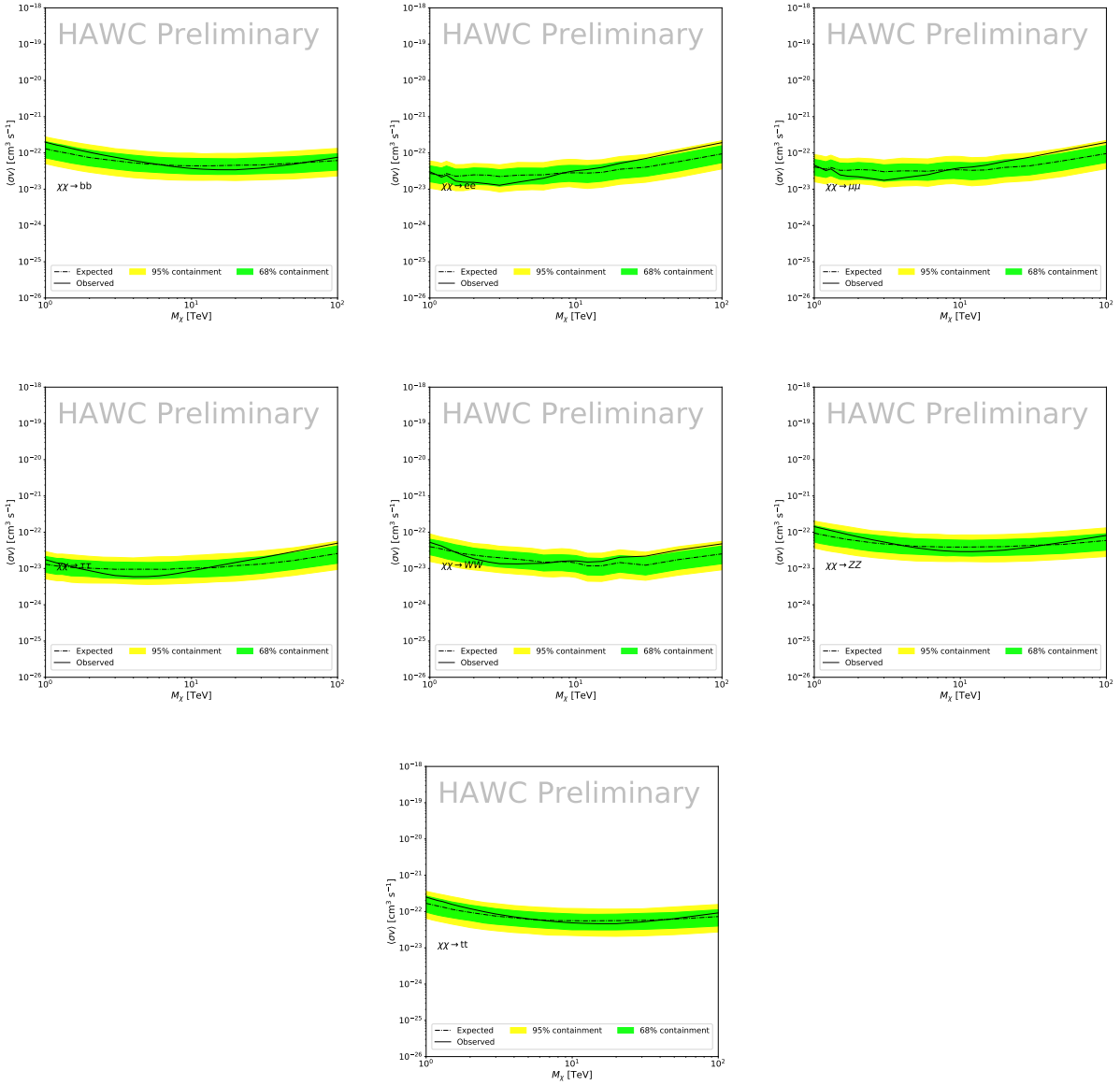


Figure 6.7 HAWC Brazil bands at 95% confidence level on $\langle\sigma v\rangle$ versus DM mass for seven annihilation channels with J -factors from \mathcal{GS} [53]. The solid line represents the combined limit from 13 dSphs. The dashed line is the expected limit. The green band is the 68% containment. The yellow band is the 95% containment.

934 6.6 Glory Duck Combined Results

935 The crux of this analysis is that HAWC's results are combined with 4 other gamma-ray observa-
 936 tories: Fermi-LAT, H.E.S.S., MAGIC, and VERITAS. No significant DM emission was observed
 937 by any of the five instruments. We present the upper limits on $\langle\sigma v\rangle$ assuming seven independent
 938 DM self annihilation channels, namely W^+W^- , Z^+Z^- , $b\bar{b}$, $t\bar{t}$, e^+e^- , $\mu^+\mu^-$, and $\tau^+\tau^-$. The 68%

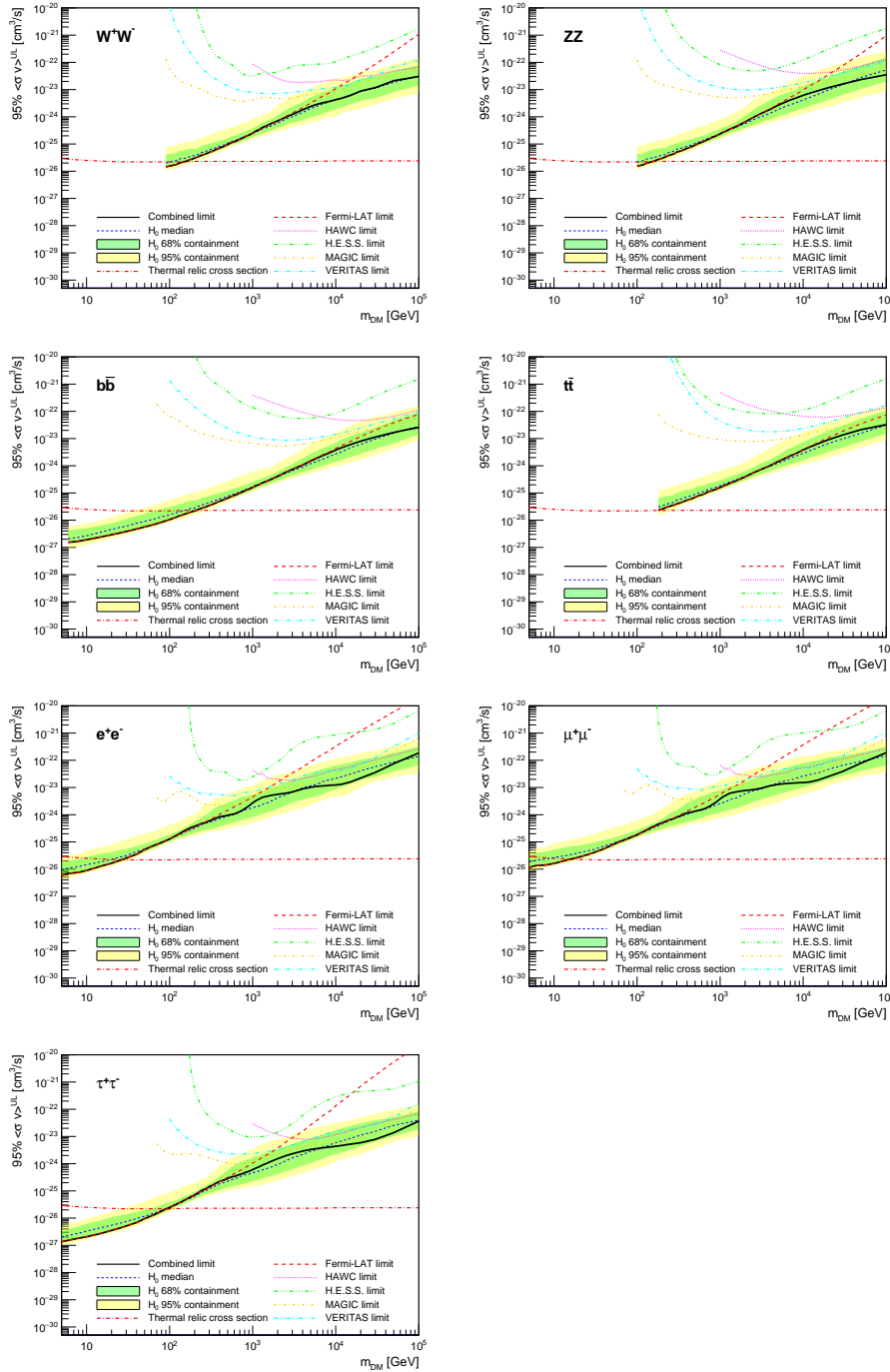


Figure 6.8 Upper limits at 95% confidence level on $\langle\sigma v\rangle$ in function of the DM mass for eight annihilation channels, using the set of J factors from Ref. [53] (\mathcal{GS} set in Table 6.1). The black solid line represents the observed combined limit, the black dashed line is the median of the null hypothesis corresponding to the expected limit, while the green and yellow bands show the 68% and 95% containment bands. Combined upper limits for each individual detector are also indicated as solid, colored lines. The value of the thermal relic cross-section in function of the DM mass is given as the red dotted-dashed line [54].

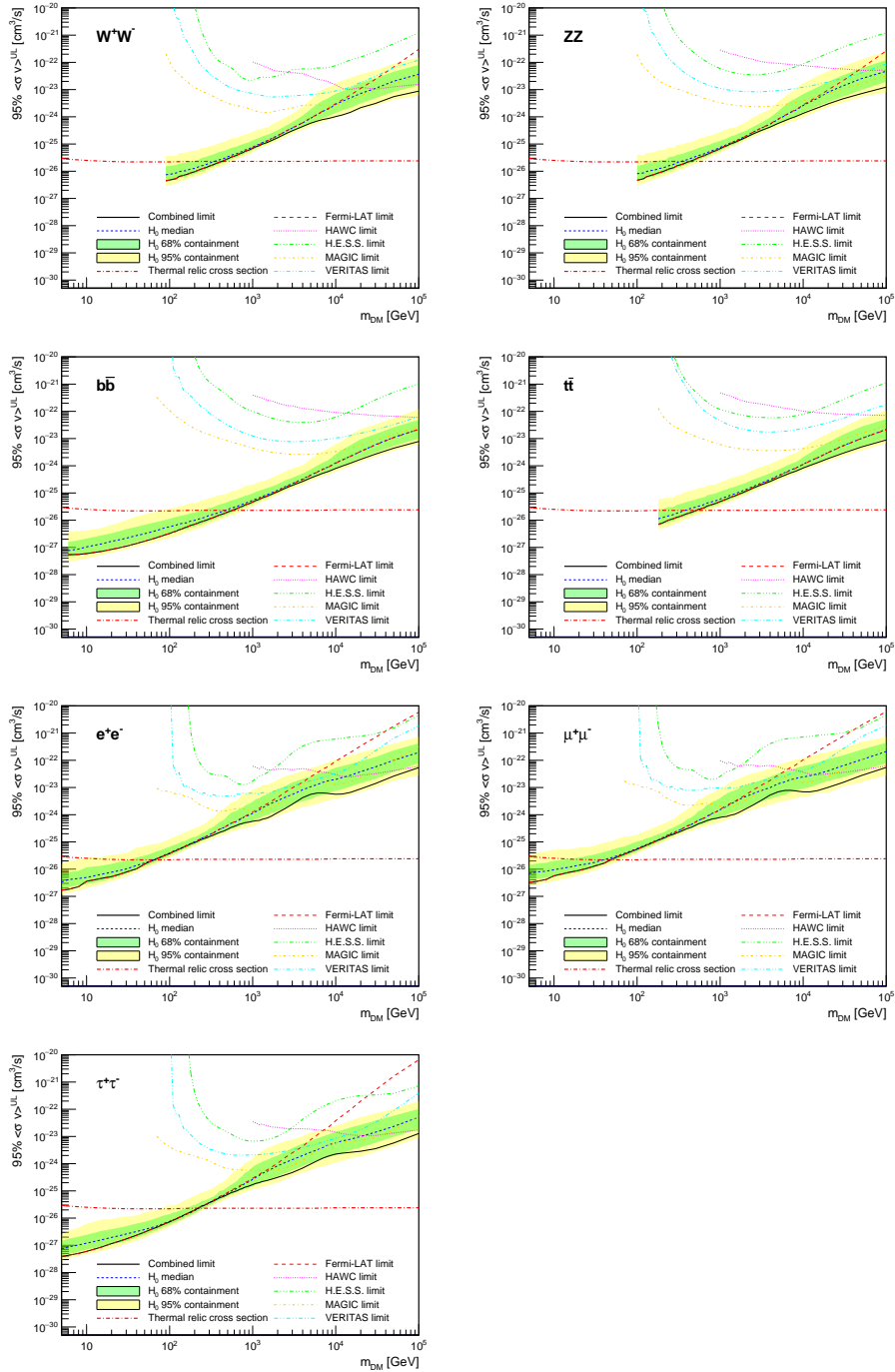


Figure 6.9 Same as Fig. 6.8, using the set of J factors from Ref. [47, 55] (\mathcal{B} set in Table 6.1).

and 95% containment bands are produced from 300 Poisson realizations of the null hypothesis corresponding to each of the combined datasets. These 300 realizations are combined identically to dSph observations. The containment bands and the median are extracted from the distribution of resulting limits on the null hypothesis. These 300 realizations are obtained either by fast simu-

943 lations of the OFF observations, for H.E.S.S., MAGIC, VERITAS, and HAWC, or taken from real
944 observations of empty fields of view in the case of Fermi-LAT [48, 56, 57].

945 The obtained limits are shown in Figure 6.8 for the $\mathcal{G}\mathcal{S}$ set of J -factors [53] and in Figure 6.9
946 for the \mathcal{B} set of J -factors [47, 55]. The combined limits are presented with their 68% and 95%
947 containment bands, and are expected to be close to the median limit when no signal is present.
948 We observe agreement with the null hypothesis for all channels, within 2σ standard deviations,
949 between the observed limits and the expectations given by the median limits. Limits obtained from
950 each detector are also indicated in the figures, where limits for all dSphs observed by the specific
951 instrument have been combined.

952 Below ~ 300 GeV, the *Fermi*-LAT dominates the DM limits for all annihilation channels. From
953 ~ 300 GeV to ~ 2 TeV, *Fermi*-LAT continues to dominate for the hadronic and bosonic DM channels,
954 yet the IACTs (H.E.S.S., MAGIC, and VERITAS) and *Fermi*-LAT all contribute to the limit for
955 leptonic DM channels. For DM masses between ~ 2 TeV to ~ 10 TeV, the IACTs dominate leptonic
956 DM annihilation channels, whereas both the *Fermi*-LAT and the IACTs dominate bosonic and
957 hadronic DM annihilation channels. From ~ 10 TeV to ~ 100 TeV, both the IACTs and HAWC
958 contribute significantly to the leptonic DM limit. For hadronic and bosonic DM, the IACTs and
959 *Fermi*-LAT both contribute strongly.

960 We notice that the limits computed using the \mathcal{B} set of J -factor are always better compared to the
961 ones calculated with the $\mathcal{G}\mathcal{S}$ set. For the W^+W^- , Z^+Z^- , $b\bar{b}$, and $t\bar{t}$ channels, the ratio between the
962 limits computed with the two sets of J -factor is varying between a factor of ~ 3 and ~ 5 depending
963 on the energy, with the largest ratio around 10 TeV. For the channels e^+e^- , $\mu^+\mu^-$, and $\tau^+\tau^-$, the
964 ratio lies between ~ 2 to ~ 6 , being maximum around 1 TeV. Examining Figure 6.16 and Figure 6.17
965 in Section 6.8, these differences are explained by the fact that the \mathcal{B} set provides higher J -factors
966 for the majority of the studied dSphs, with the notable exception of Segue I. The variation on the
967 ratio of the limits for the two sets is due to different dSph dominating the limits depending on the
968 energy. This pushes the range of thermal cross-section which can be excluded to higher mass. This
969 comparison demonstrates the magnitude of systematic uncertainties associated with the choice of

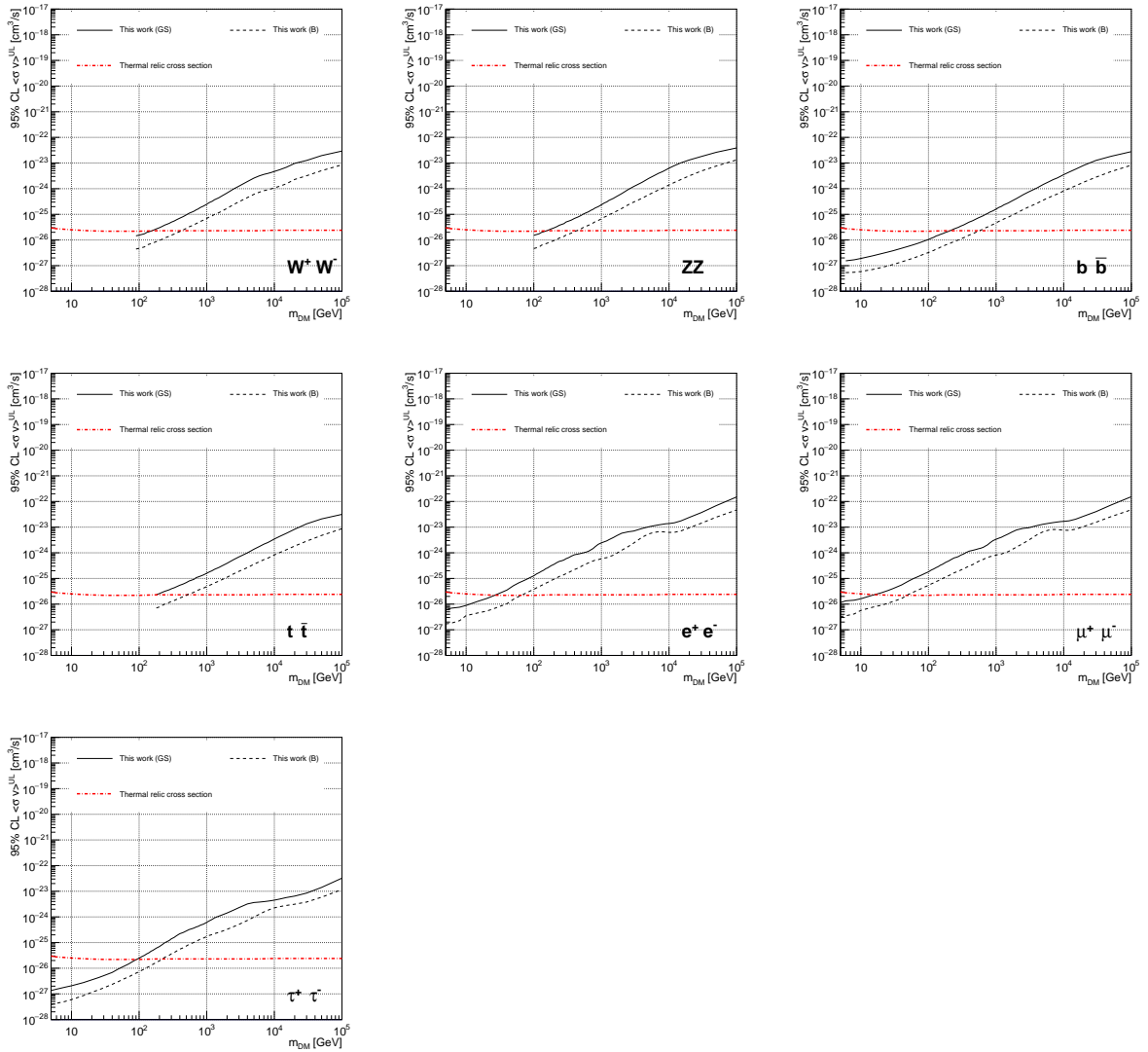


Figure 6.10 Comparisons of the combined limits at 95% confidence level for each of the eight annihilation channels when using the J factors from Ref. [53] (\mathcal{GS} set in Table 6.1), plain lines, and the J factor from Ref. [47, 55] (\mathcal{B} set in Table 6.1), dashed lines. The cross-section given by the thermal relic is also indicated [54].

970 the J -factor

971 This comparison demonstrates the magnitude of systematic uncertainties associated with the
 972 choice of the J -factor calculation. The \mathcal{GS} and \mathcal{B} sets present a difference in the limits for all
 973 channels of about This difference is explained, see Figure 6.16 and Figure 6.17 in Appendix, by the
 974 fact that the \mathcal{B} set provides higher J factors for all dSph except for Segue I. This pushes the range
 975 of thermal cross-section which can be excluded to higher mass.

976 **6.7 HAWC Systematics**

977 **6.7.1 Inverse Compton Scattering**

978 The DM-DM annihilation channels produce many high energy electrons regardless of the
979 primary annihilation channel. These high energy electrons can produce high energy gamma-rays
980 through Inverse Compton Scattering (ICS). If this effect is strong, it would change the morphology
981 of the source and increase the total expected gamma-ray counts from any source. The PPPC [44]
982 provides tools in Mathematica for calculating the impact of ICS for an arbitrary location in the
983 sky for a specified annihilation channel. We calculated the change in gamma-ray counts for DM
984 annihilation to primary $e\bar{e}$ for RA and Dec corresponding to Segue1 and Coma Berenices. These
985 dSphs were chosen because they are the strongest contributors to the limit. $e\bar{e}$ was selected because
986 it would have the largest number of high energy electrons. The effect was found to be on the order
987 of 10^{-7} on the gamma-ray spectrum. As a result, this systematic is not considered in our analysis.

988 **6.7.2 Point Source Versus Extended Source Limits**

989 The previous DM search toward dSph approximated the dSphs as point sources [46]. In
990 this analysis, the dSphs are implemented as extended with J-factor distributions following those
991 produced by [53]. The resolution of the cited map is much finer than HAWC's angular resolution.
992 The vast majority of the J-factor distribution is represented on the central HAWC pixel of the dSph
993 spatial map. However, the neighboring 8 pixels are not negligible and contribute to our limit.

994 Figure 6.11 shows a substantial improvement to the limit for Segue1. Fig. 6.12 however showed
995 identical limits. These disparities are best explained by the relative difference in their J-Factors.
996 Both dSphs pass almost overhead the HAWC detector, however Segue1 has the larger J-Factor
997 between the two. Adjacent pixels to the central pixel will therefore contribute to the limits. This is
998 the case for other dSph that are closer to overhead the HAWC detector.

999 Comparison plots for all sources and the combined limit can be found in the sandbox for the
1000 Glory Duck project.

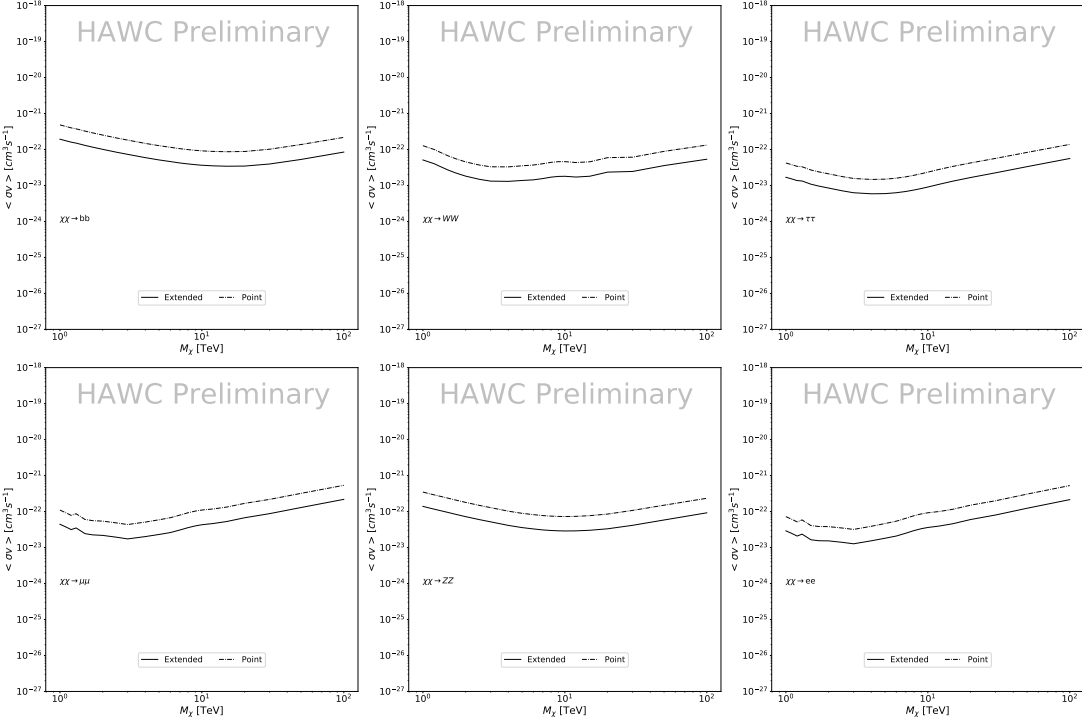


Figure 6.11 Comparisons of the combined limits at 95% confidence level for a point source analysis and extended source using [53] \mathcal{GS} J-factor distributions and PPPC [44] annihilation spectra. Shown are the limits for Segue1 which will have the most significant impact on the combined limit. 6 of the 7 DM annihilation channels are shown. Solid lines are extended source studies. Dashed lines are point source studies. Overall, the extended source analysis improves the limit by a factor of 2.

1001 6.7.3 Impact of Pointing Systematic

1002 During the analysis it was discovered that reconstruction of gamma-rays. Slides describing this
 1003 systematic can be found [here](#). Shown on the presentation is dependence on the pointing systematic
 1004 on declination. New spatial profiles were generated for every dSph and limits were computed for
 1005 the adjusted declination.

1006 Section 6.7.3 demonstrates the impact of this systematic for all DM annihilation channels
 1007 studied by HAWC. The impact is a tiny improvement, yet mostly identical, to the combined limits.

1008 6.8 J-factor distributions

1009 6.8.1 Numerical integration of \mathcal{GS} maps

1010 It was discovered well after the HAWC analysis was completed that the published tables from
 1011 \mathcal{GS} [45] quoted median J-factors were computed in a non-trivial manner. The assumption myself

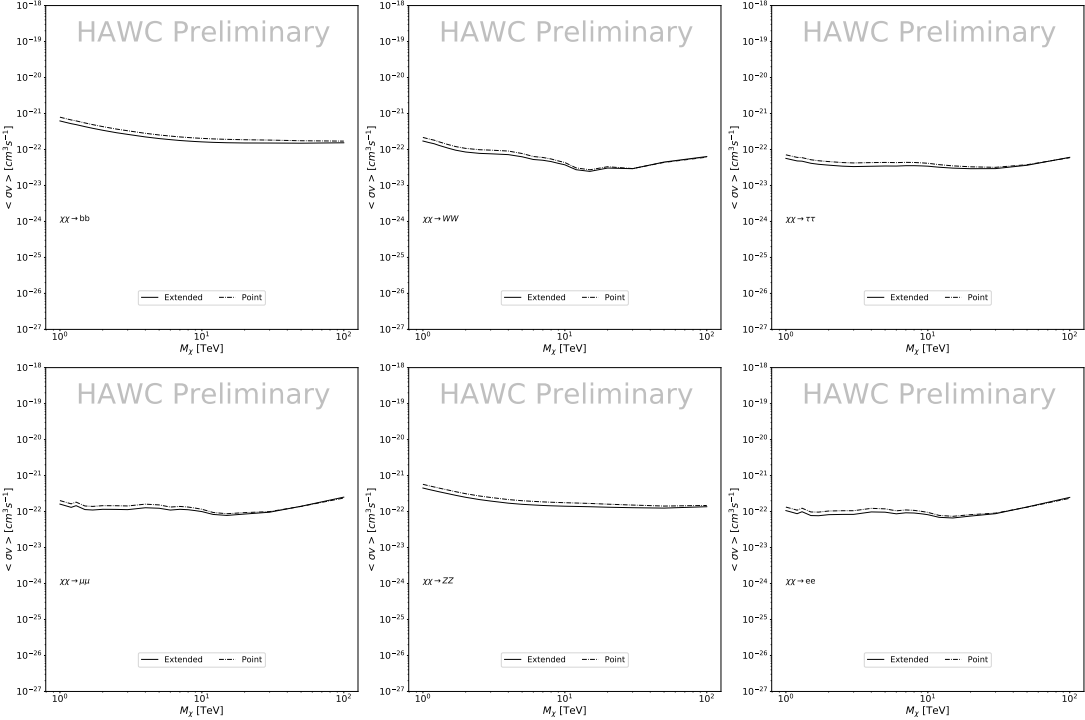


Figure 6.12 Same as Fig. 6.11 on Coma Berenices. This dSph also contributes significantly to the limit. The limits are identical in this case.

and collaborators had been that the published tables represented the J -factor as a function of θ for the best global fit model on a per-source basis. However, this is not the case. Instead, what is published are the best fit model for each dwarf that only considers stars up to the angular separation θ . Therefore, the model is changing for each value of θ for each dwarf. Yet, the introduced features from unique models at each θ are much smaller than the angular resolution of HAWC. It is not expected for these effects to impact the limits and TS greatly as a result.

Median J -factor model profiles were provided by the authors. New maps were generated and analyzed for Segue1 and Coma Berenices. Figure 6.14 shows the differential between maps generated with the method from Section 6.8.1 and from the authors of [45]. These maps were reanalyzed for all SM DM annihilation channels. Upper limits for these channels are shown in Figure 6.15

From Figure 6.15, we can see that the impact of these model difference was no substantial. The observed impact was a fractional effect which is much smaller than the impact from selecting another DM spatial distribution model as was shown in Figure 6.10.

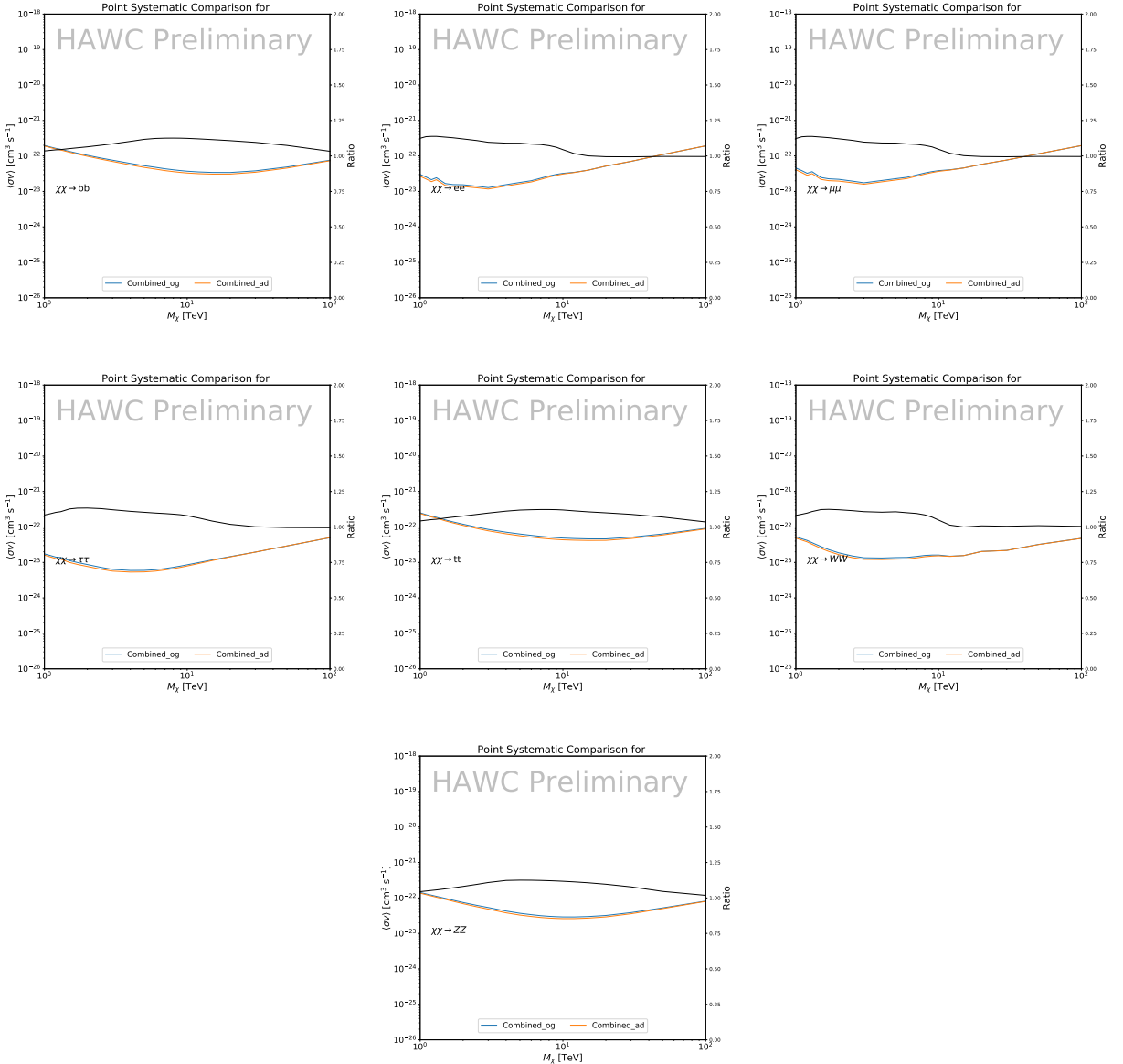


Figure 6.13 Comparison of combined limits when correcting for HAWC's pointing systematic. All DM annihilation channels are shown. The solid black line is the ratio between published limit to the declination corrected limit. The blue solid line or "Combined_og" represented the limits computed for Glory Duck. The solid orange line or "Combined_ad" represented the limits computed after correcting for the pointing systematic.

1026 6.8.2 $\mathcal{G}\mathcal{S}$ Versus \mathcal{B} spatial models

1027 We show in this appendix a comparison between the J -factors computed by Geringer-Sameth
 1028 *et al.* [53] (the $\mathcal{G}\mathcal{S}$ set) and the ones computed by Bonnivard *et al.* [47, 55] (the \mathcal{B} set). The
 1029 $\mathcal{G}\mathcal{S}$ J -factors are computed through a Jeans analysis of the kinematic stellar data of the selected

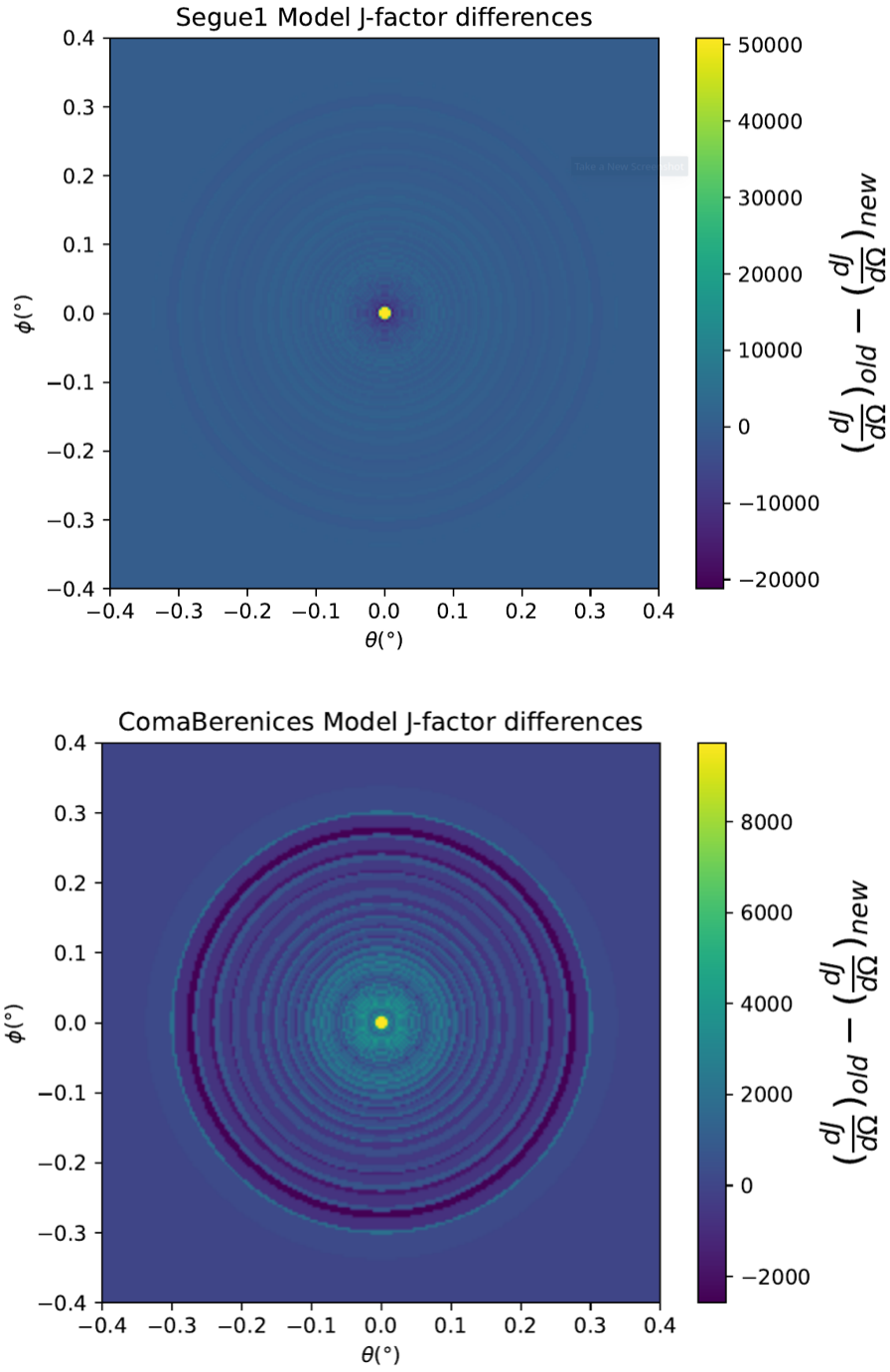


Figure 6.14 Differential map of dJ/Ω from model built in Section 6.8.1 and profiles provided directly from authors. (Top) Differential from Segue1. (bottom) Differential from Coma Berenices. Note that their scales are not the same. Segue1 shows the deepest discrepancies which is congruent with its large uncertainties. Both models show anuli where unique models become apparent.

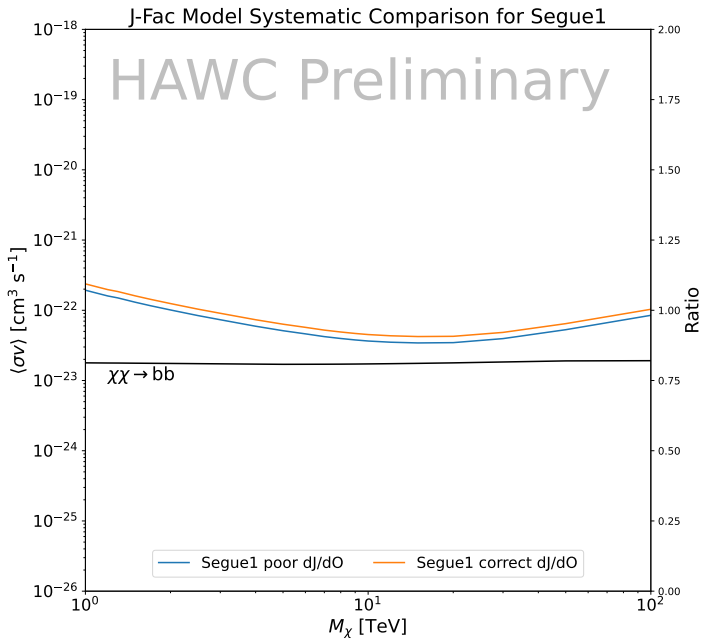
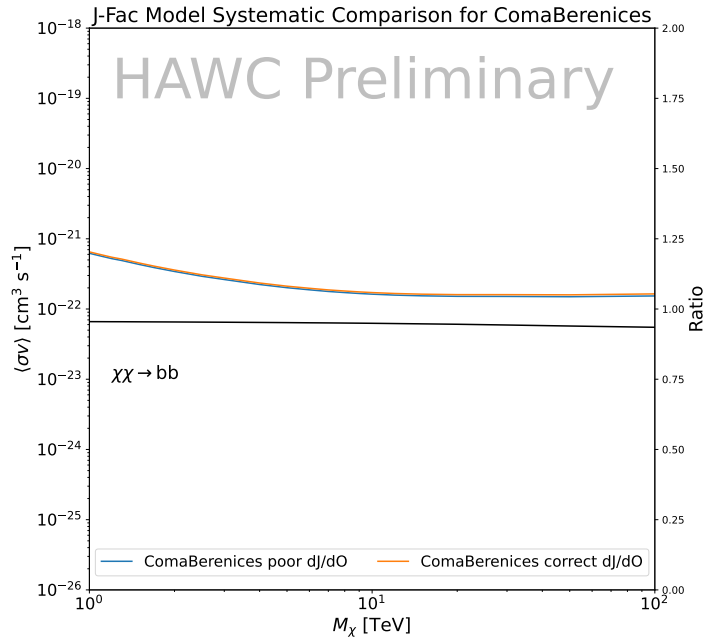


Figure 6.15 HAWC limits for Coma Berenices (top) and Segue1 (bottom) for two different map sets. Blue lines are limits calculated on maps with poor model representation. Orange lines are limits calculated on spatial profiles provided by the authors of [45]. Black line is the ratio of the poor spatial model limits to the corrected spatial models. The left y-axis measures $\langle \sigma v \rangle$ for the blue and orange lines. The right y-axis measures the ratio and is unitless.

1030 dSphs, assuming a dynamic equilibrium and a spherical symmetry for the dSphs. They adopted
1031 the generalized DM density distribution, known as Zhao-Hernquist, introduced by [58], carrying
1032 three additional index parameters to describe the inner and outer slopes, and the break of the
1033 density profile. Such a profile parametrization allows the reduction of the theoretical bias from
1034 the choice of a specific radial dependency on the kinematic data. In other words, the increase of
1035 free parameters with the use of the Zhao-Hernquist profile allows a better description of the mass
1036 density distribution of dark matter.

1037 In addition, a constant velocity anisotropy profile and a Plummer light profile [59] for the stellar
1038 distribution were assumed. The velocity anisotropy profile depends on the radial and tangential
1039 velocity dispersion. However, its determination remains challenging since only the line-of-sight
1040 velocity dispersion can be derived from velocity measurements. Therefore, the parametrization of
1041 the anisotropy profile is obtained from simulated halos (see [60] for more details). They provide the
1042 values of the J -factors of regions extending to various angular radius up to the outermost member
1043 star.

1044 The \mathcal{B} J -factors were computed through a Jeans analysis taking into account the systematic
1045 uncertainties induced by the DM profile parametrization, the radial velocity anisotropy profile, and
1046 the triaxiality of the halo of the dwarf galaxies. They performed a more complete study of the dSph
1047 kinematics and dynamics than \mathcal{GS} for the determination of the J -factor. Conservative values of the
1048 J -factors where obtained using an Einasto DM density profile [61], a realistic anisotropy profile
1049 known as the Baes & Van Hese profile [62] which takes into account that the inner regions can be
1050 significantly non-isotropic, and a Zhao-Hernquist light profile [58].

1051 For both sets, J -factor values are provided for all dSphs as a function of the radius of the
1052 integration region [53, 47, 55]. Table 6.1 shows the heliocentric distance and Galactic coordinates
1053 of the twenty dSphs, together with the two sets of J -factor values integrated up to the outermost
1054 observed star for \mathcal{GS} and the tidal radius for \mathcal{B} . Both J -factor sets were derived through a Jeans
1055 analysis based on the same kinematic data, except for Draco where the measurements of [63] have
1056 been adopted in the computation of the \mathcal{B} value. The computations for producing the \mathcal{GS} and \mathcal{B}

1057 samples differ in the choice of the DM density, velocity anisotropy, and light profiles, for which the
1058 set \mathcal{B} takes into account some sources of systematic uncertainties.

1059 Figure 6.16 and Figure 6.17 show the comparisons for the J -factor versus the angular radius
1060 for each of the 20 dSphs used in this study. The uncertainties provided by the authors are also
1061 indicated in the figures. For the \mathcal{GS} set, the computation stops at the angular radius corresponding
1062 to the outermost observed star, while for the \mathcal{B} set, the computation stops at the angular radius
1063 corresponding to the tidal radius.

1064 6.9 Discussion and Conclusions

1065 In this multi-instrument analysis, we have used observations of 20 dSphs from the gamma-ray
1066 telescopes Fermi-LAT, H.E.S.S., MAGIC, VERITAS, and HAWC to perform a collective DM
1067 search annihilation signals. The data were combined across sources and detectors to significantly
1068 increase the sensitivity of the search. We have observed no significant deviation from the null, no
1069 DM hypothesis, and so present our results in terms of upper limits on the annihilation cross-section
1070 for seven potential DM annihilation channels.

1071 Fermi-LAT brings the most stringent constraints for continuum channels below approximately
1072 1 TeV. The remaining detectors dominate at higher energies. Overall, for multi-TeV DM mass,
1073 the combined DM constraints from all five telescopes are 2-3 times stronger than any individual
1074 telescope for multi-TeV DM.

1075 Derived from observations of many dSphs, our results produce robust limits given the DM
1076 content of the dSphs is relatively well constrained. The obtained limits span the largest mass
1077 range of any WIMP DM search. Our combined analysis improves the sensitivity over previously
1078 published results from each detector which produces the most stringent limits on DM annihilation
1079 from dSphs. These results are based on deep exposures of the most promising known dSphs with
1080 the currently most sensitive gamma-ray instruments. Therefore, our results constitute a legacy of
1081 a generation of gamma-ray instruments on WIMP DM searches towards dSphs. Our results will
1082 remain the reference in the field until a new generation of more sensitive gamma-ray instruments
1083 begin operations, or until new dSphs with higher J -factors are discovered.

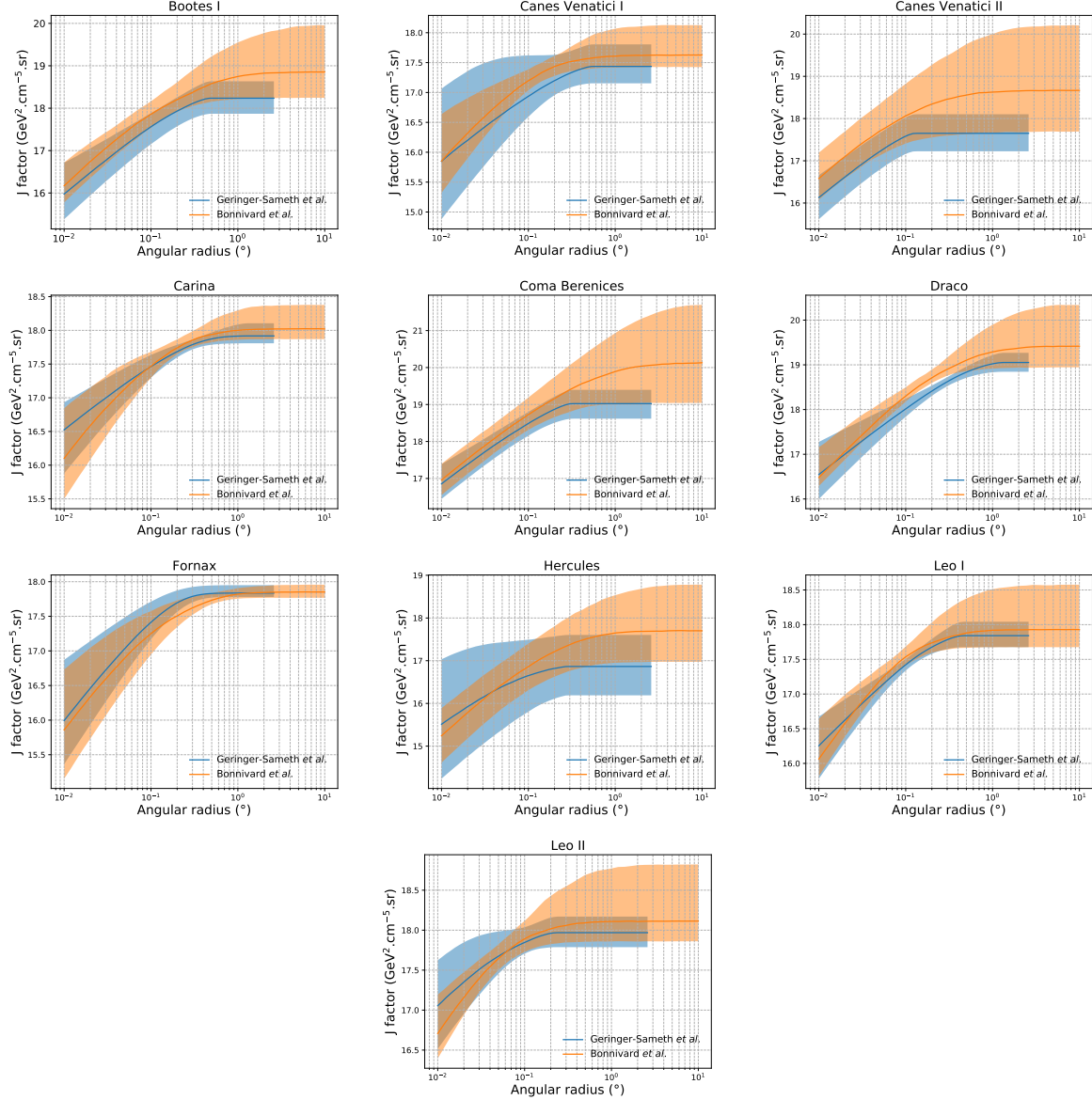


Figure 6.16 Comparisons between the J -factors versus the angular radius for the computation of J factors from Ref. [53] (\mathcal{GS} set in Table 6.1) in blue and for the computation from Ref. [47, 55] (\mathcal{B} set in Tab. 6.1) in orange. The solid lines represent the central value of the J -factors while the shaded regions correspond to the 1σ standard deviation.

This analysis serves as a proof of concept for future multi-instrument and multi-messenger combination analyses. With this collaborative effort, we have managed to sample over four orders in magnitude in gamma-ray energies with distinct observational techniques. Determining the nature of DM continues to be an elusive and difficult problem. Larger datasets with diverse measurement techniques could be essential to tackling the DM problem. A future collaboration using similar

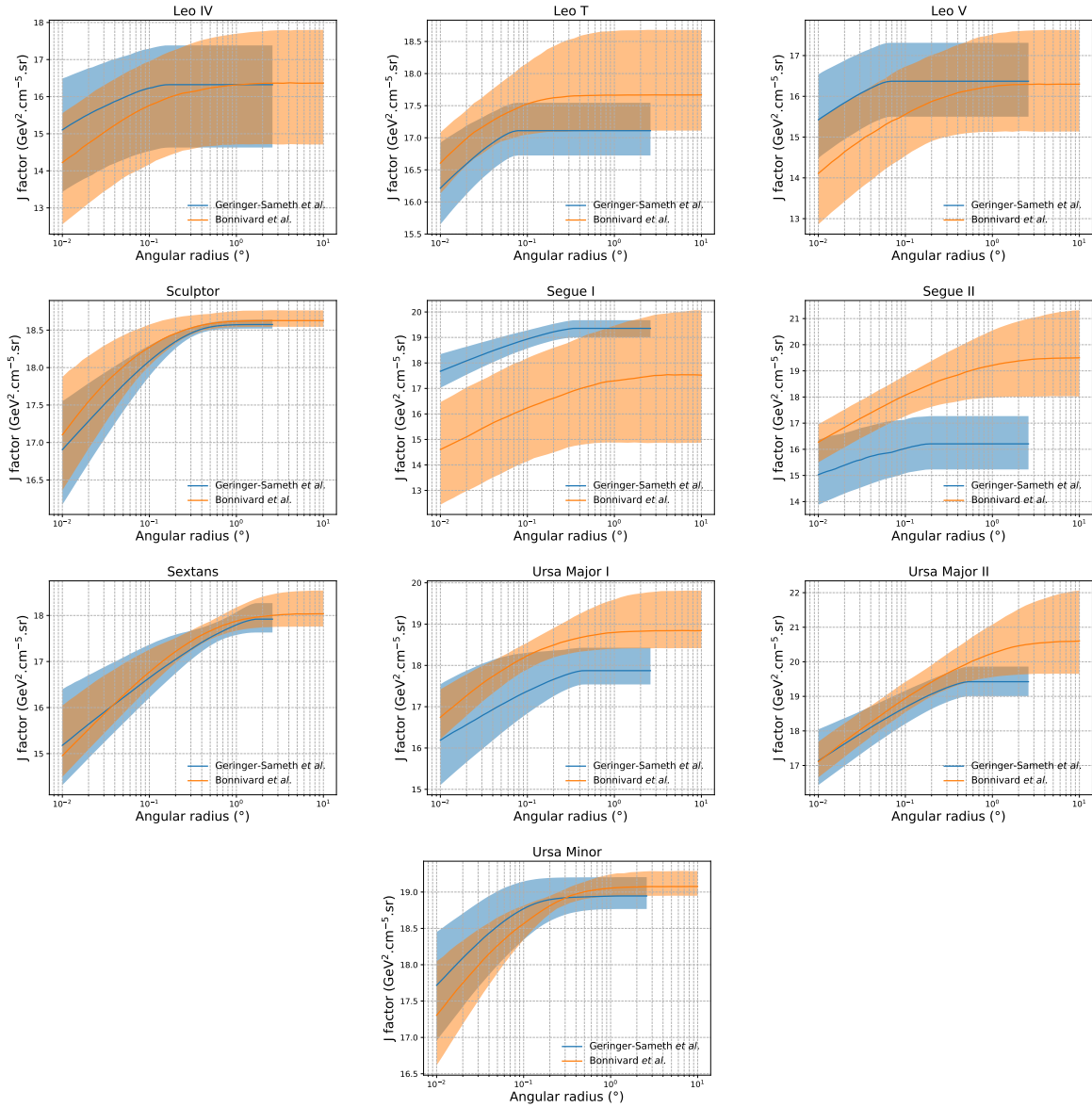


Figure 6.17 Comparisons between the J -factors versus the angular radius for the computation of J factors from Ref. [53] (\mathcal{GS} set in Tab. 6.1) in blue and for the computation from Ref. [47, 55] (\mathcal{B} set in Tab. 6.1) in orange. The solid lines represent the central value of the J -factors while the shaded regions correspond to the 1σ standard deviation.

1089 techniques as the ones described in this paper could grow even beyond gamma rays. The models we
 1090 used for this study include annihilation channels with neutrinos in the final state. Advanced studies
 1091 could aim to merge our results with those from neutrino observatories with large data sets. Efforts
 1092 are already underway to add data from the IceCube, ANTARES, and KM3NeT observatories to
 1093 these gamma-ray results.

1094 From this work, a selection of the best candidates for observations, according to the latest
1095 knowledge on stellar dynamics and modelling techniques for the derivation of the J -factors on
1096 the potential dSphs targets, is highly desirable at the time that new experiments are starting their
1097 dark matter programs using dSphs. Given the systematic uncertainty inherent to the derivation of
1098 the J -factors, an informed observational strategy would be to select both objects with the highest
1099 J -factors that could lead to DM signal detection, and objects with robust J -factor predictions, i.e.
1100 with kinematic measurements on many bright stars, which would strengthen the DM interpretation
1101 reliability of the observation outcome.

1102 This analysis combines data from multiple telescopes to produce strong constraints on astro-
1103 physical objects. From this perspective, these methods can be applied beyond just DM searches.
1104 Almost every astrophysical study can benefit from multi-telescope, multi-wavelength gamma-ray
1105 studies. We have enabled these telescopes to study the cosmos with greater precision and detail.
1106 Many astrophysical searches can benefit from multi-instrument gamma-ray studies, for which our
1107 analysis lays the foundation.

CHAPTER 7

MULTITHREADING HAWC ANALYSES FOR DARK MATTER SEARCHES

7.1 Introduction

HAWC's current software suite, plugins to 3ML, does not fully utilize computational advancements of recent decades. Said advancements include the proliferation of Graphical Processing Units (GPUs), and multithreading on multi-core processors. The analysis described in chapter 6 took up to 3 months of human time waiting for the full gambit of data analysis and simulation of background to run. Additionally, with the addition of a 2D binning scheme, f_{hit} and NN, the compute time is expected to grow. Although excessive computing time was, in part, from an intense use of a shared computing cluster, it was evident that there was room for improvement. In HAWC's next generation dSph DM search, I decided to develop codes that would utilize the multi-core processors on modern high performance computing clusters. The results of this work are featured in this chapter and brought a human timing improvement to computation that scales as $1/N$ where N is the number of threads.

7.2 Dataset and Background

This section enumerates the data and background methods used for HAWC's multi-threaded study of dSphs. Section 7.2.1 and Section 7.2.2 are most useful for fellow HAWC collaborators looking to replicate a multithreaded dSph DM search.

7.2.1 Itemized HAWC files

- Detector Resolution: `refit-Pass5-Final-NN-detRes-zenith-dependent.root`
- Data Map: `Pass5-Final-NN-maptree-ch103-ch1349-zenith-dependent.root`
- Spectral Dictionary: `HDMspectra_dict_gamma.npy`

7.2.2 Software Tools and Development

This analysis was performed using HAL and 3ML [42, 43] in Python version 3. I built software in collaboration with Michael Martin and Letrell Harris to implement the *Dark Matter Spectra from*

1132 *the Electroweak to the Planck Scale* (HDM) [64] and dSphs spatial model from [65] for HAWC
1133 analysis. A NumPy dictionary of HDM was made for Py3. The corresponding Python3 file is
1134 `HDMspectra_dict_gamma.npy`. These files can also be used for decay channels and tools are
1135 provided in HDM’s [git repository](#) [64]. The analysis was performed using the Neural Network
1136 energy estimator for Pass 5.F. A description of this estimator was provided in chapter 4. **TODO:**
1137 **define a subsection when it’s written**, and its key improvements are an improved energy estimation
1138 and improved sensitivities at higher zenith angles. All other software used for data analysis, DM
1139 profile generation, and job submission to SLURM are also kept in my sandbox in the [Dark Matter](#)
1140 [HAWC](#) project. The above repository also incorporates the model inputs used previously in Glory
1141 Duck, described in chapter 6

1142 **7.2.3 Data Set and Background Description**

1143 The HAWC data maps used for this analysis contain 2565 days of data between runs 2104 (
1144 **TODO: Day start**) and 7476 (**TODO: day end**). They were generated from pass 5.f reconstruction.
1145 The analysis is performed using the NN energy estimator with bin list:

1146 B1C0Ea, B1C0Eb, B1C0Ec, B1C0Ed, B1C0Ee, B2C0Ea, B2C0Eb, B2C0Ec, B2C0Ed, B2C0Ee,
1147 B3C0Ea, B3C0Eb, B3C0Ec, B3C0Ed, B3C0Ee, B3C0Ef, B4C0Eb, B4C0Ec, B4C0Ed, B4C0Ee,
1148 B4C0Ef, B5C0Ec, B5C0Ed, B5C0Ee, B5C0Ef, B5C0Eg, B6C0Ed, B6C0Ee, B6C0Ef, B6C0Eg,
1149 B6C0Eh, B7C0Ee, B7C0Ef, B7C0Eg, B7C0Eh, B7C0Ei, B8C0Ee, B8C0Ef, B8C0Eg, B8C0Eh,
1150 B8C0Ei, B8C0Ej, B9C0Ef, B9C0Eg, B9C0Eh, B9C0Ei, B9C0Ej, B10C0Eg, B10C0Eh,
1151 B10C0Ei, B10C0Ej, B10C0Ek, B10C0El

1152 Bin 0 was excluded as it has substantial hadronic contamination and poor angular resolution.

1153 Background considerations and source selection was identical to Section 6.2, and no additional
1154 arguments are provided here. Many of the HAWC systematics explored in Section 6.7 also apply
1155 for this DM search and are not added upon here.

1156 **7.3 Analysis**

1157 The analysis and its systematics are almost identical to Section 6.3. Importantly, we use the
1158 same Equation (6.1) and Equation (6.2) for estimating the gamma-ray flux at HAWC from our
1159 sources. We add on to the previous study with a search for DM decay. The flux equations for DM
1160 decay are

$$\frac{d\Phi_\gamma}{dE_\gamma} = \frac{1}{4\pi\tau m_\chi} \frac{dN_\gamma}{dE_\gamma} \times \int_{\text{source}} d\Omega \int_{l.o.s} \rho_\chi dl(r, \theta') \quad (7.1)$$

1161 with a new quantity, the D factor, defined as

$$D = \int d\Omega \int_{l.o.s} dl \rho_\chi(r, \theta') \quad (7.2)$$

1162 Software was written to accomodate DM decay from dSphs, however decay profiles were not
1163 received from $\mathcal{L}\mathcal{S}$ by the time of writing this tehsis.

1164 **7.3.1 $\frac{dN_\gamma}{dE_\gamma}$ - Particle Physics Component**

1165 For these spectra, we import HDM with Electroweak (EW) corrections and additional correc-
1166 tions for neutrinos above the EW scale [64]. The spectrum is implemented as a model script in
1167 astromodels for 3ML. A comprehensive description of EW corrections and neutrino considerations
1168 are provided later in **TODO: refeance MM nu duck.**

1169 Figure 7.1 demonstrates the impact of changes from HDM on DM annihilation to W bosons.
1170 A class in astromodels was developed to include HDM and is aptly named **HDMspectra** within
1171 **DM_models.py**. The SM DM annihilation channels studied here are $\chi\chi \rightarrow:$

1172 $e^+e^-, \mu^+\mu^-, \tau^+\tau^-, b\bar{b}, t\bar{t}, gg, W^+W^-, ZZ, c\bar{c}, u\bar{u}, d\bar{d}, s\bar{s}, \nu_e\bar{\nu}_e, \nu_\mu\bar{\nu}_\mu, \nu_\tau\bar{\nu}_\tau, \gamma\gamma, hh.$

1173 For $\gamma\gamma$ and ZZ , a substantial fraction of the signal photons are expected to have total energy equal
1174 m_χ [64]. This introduces a δ -function that is much narrower than the energy resolution of the
1175 HAWC detector. To ensure that this feature is not lost in the likelihood fits, the 'line' feature is
1176 convolved with a gaussian kernel with a 1σ width of $0.05 \cdot m_\chi$ and total kernel window of $\pm 4\sigma$.
1177 This difers from HAWC's previous line study where 30% of HAWC's energy resolution was used
1178 for the kernel [66]. The NN energy estimator's strength compared to f_{hit} at low gamma-ray energy

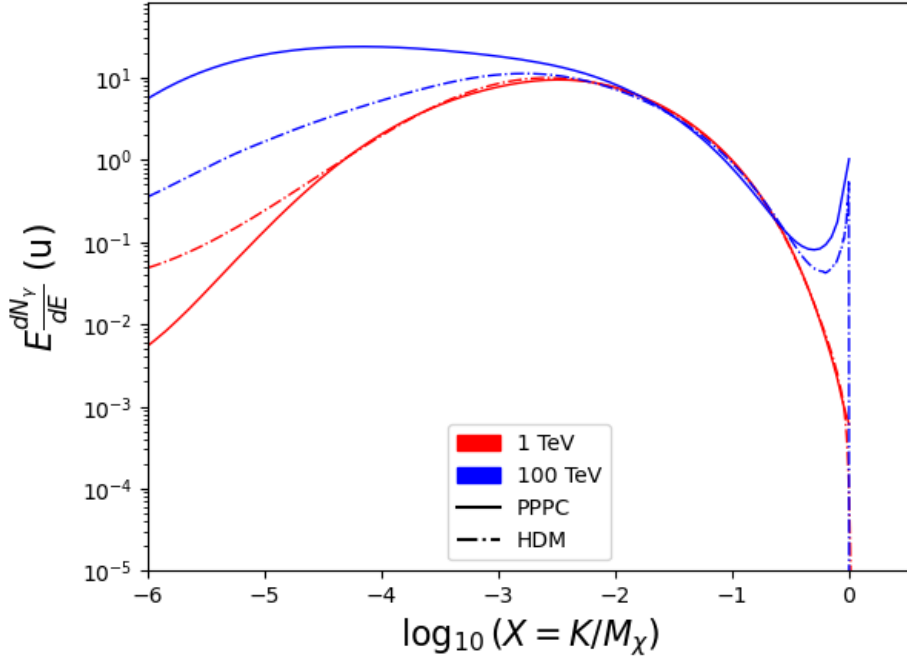


Figure 7.1 Difference between spectral hypotheses from PPPC [44] and HDM [64]. Shown is the expected DM annihilation spectrum for $\chi\chi \rightarrow W^-W^+$. Solid lines are spectral models with EW corrections from the PPPC. Dash-dot lines are spectral models from HDM. Red lines are models for $M_\chi = 1$ TeV. Blue lines represent models for $M_\chi = 100$ TeV.

enables smaller resolutions in addition to low energy tails in the spectral models [64]. $\chi\chi \rightarrow \gamma\gamma$ and ZZ spectral hypotheses are shown in Figure 7.2. Spectral models for the remaining annihilation channels are plotted for each m_χ in Figure B.1.

7.3.2 J and D- Astrophysical Components

The J-factor profiles for each source are imported from Louis Strigari et al. (referred to with \mathcal{LS}) [65]. Profiles in $\frac{dJ}{d\Omega}(\theta)$ up to $\theta = 0.5^\circ$ were provided directly from the authors. Map generation from these profiles were almost identical to Section 6.3.2 except that a higher order trapezoidal integral was used for the normalization of the square, uniformly-spaced map:

$$p^2 \cdot \sum_{i=0}^N \sum_{j=0}^M w_{i,j} \frac{d\mathcal{K}}{d\Omega}(\theta_{i,j}, \phi_{i,j}) \quad (7.3)$$

\mathcal{K} is either J or D for the spatial distributions of annihilation or decay respectively. p is the angular side of one pixel in the map. $w_{i,j}$ is a weight assigned the following ways:

$w_{i,j} = 1$ if $(\theta_{i,j}, \phi_{i,j})$ is fully within the region of integration

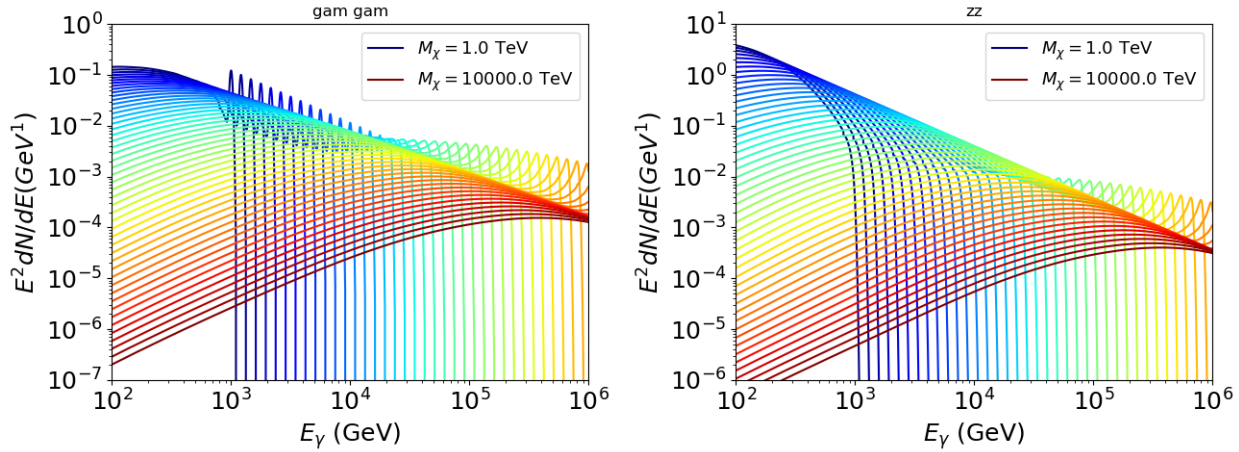


Figure 7.2 Photon spectra for $\chi\chi \rightarrow \gamma\gamma$ (left) and $\chi\chi \rightarrow ZZ$ (right) after gaussian convolution of line features. Both spectra have δ -features at photon energies equal to the DM mass. Bluer lines are annihilation spectra with lower DM mass. Redder lines are spectra from larger DM mass. All Spectral models are sourced from the Heavy Dark Matter models [64]. Axes are drawn roughly according to the energy sensitivity of HAWC.

1190 $w_{i,j} = 1/2$ if $(\theta_{i,j}, \phi_{i,j})$ is on an edge of the region of integration

1191 $w_{i,j} = 1/4$ if $(\theta_{i,j}, \phi_{i,j})$ is on a corner of the region of integration

1192 Figure 7.3 shows the median and $\pm 1\sigma$ maps used as input for DM annihilation studied by \mathcal{LS} .

1193 **7.3.3 Source Selection and Annihilation Channels**

1194 HAWC's sources for this multithreaded analysis include Coma Berenices, Draco, Segue 1, and

1195 Sextans \mathcal{LS} observes up to 43 sources in its publication, however only 4 of the best fit profiles were

1196 provided at the time this thesis was written. A full description of each source used in this analysis

1197 is found in Table 7.1.

1198 This analysis improves on chapter 6 in the following ways. Previously, the particle physics

1199 model used for gamma-ray spectra from DM annihilation was from the PPPC [44] which missed

1200 important considerations relevant for the neutrino sector. HDM is used to account for this shortfall

1201 [64]. HDM also models DM to the Planck scale which permits HAWC to probe PeV scale DM.

1202 For this study, we sample DM masses: 1 TeV - 10 PeV with 6 mass bins per decade in DM mass.

1203 In the case of line spectra ($\chi\chi \rightarrow \gamma\gamma$, or ZZ), we double the mass binning to 12 DM mass bins

1204 per decade in DM mass. A larger source catalog is used that uses a Navarro–Frenk–White (NFW)

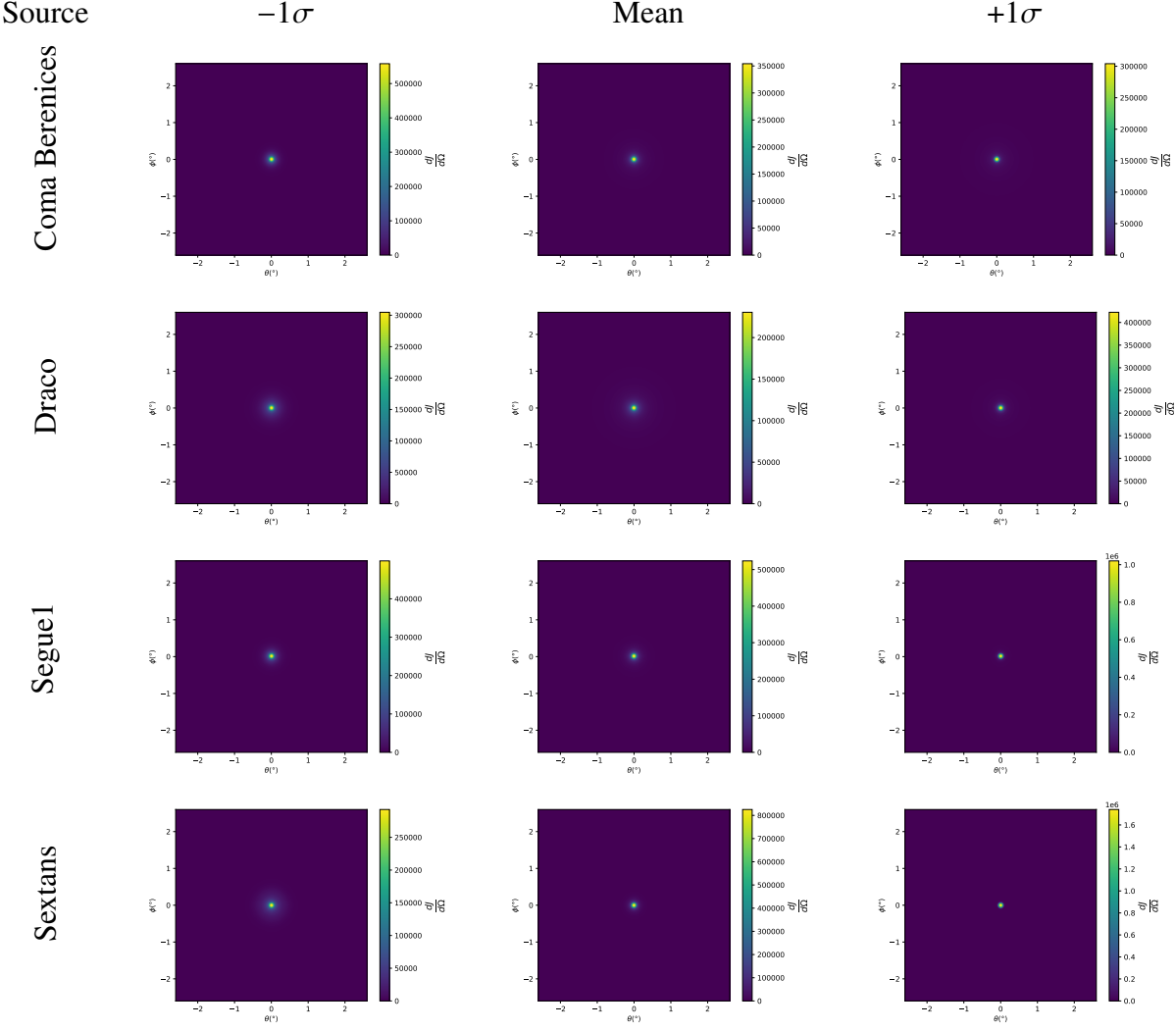


Figure 7.3 $\frac{dJ}{d\Omega}$ maps for Coma Berenices, Draco, Segue1, and Sextans. Columns are divided for the $\pm 1\sigma$ uncertainties in $dJ/d\Omega$ around the mean value from \mathcal{LS} [65]. Origin is centered on the specific dwarf spheroidal galaxies (dSph). θ and ϕ axes are the angular separation from the center of the dwarf

1205 spatial DM distribution from \mathcal{LS} [65]. Because NFW has fewer parameters than what is used
 1206 for \mathcal{GS} , \mathcal{LS} is able to fit ultra-faint dwarves, expanding the number of sources available for DM
 1207 searches. Finally, the gamma-ray ray dataset is much larger. The study performed here analyzes
 1208 2565 days of data compared to 1017 days analyzed in chapter 6.

1209 7.4 Likelihood Methods

1210 These are identical to Section 6.4.1 and no additional changes are made to the likelihood. Bins
 1211 in this analysis are expanded to include HAWC’s NN energy estimator.

1212 **7.5 Computational Methods: Multithreading**

1213 Previously, as in Section 6.3, the likelihood was minimized for one model at a time. One
 1214 model in this case representing a DM annihilation channel, DM mass, and dSph. In an effort
 1215 to conserve human and CPU time, jobs submitted for high performance computing contained a
 1216 list of DM masses to iterate over for likelihood fitting. Jobs were then trivially parallelized for
 1217 each permutation of the two lists: CHANS (SM annihilation channel) and SOURCES (dSph spatial
 1218 templates). The lists for CHANS and SOURCES are found in Section 7.3.1 and Table 7.1, respectively.
 1219 Initially, 11 DM mass bins were serially sampled for one job defined by a [SM channel, dSph] set.
 1220 Computing the likelihoods would take between 1.5 to 2 hrs, stocastically, for a job. We expect to
 1221 compute likelihoods for data and 300 Poisson background trials. The estimated CPU time based on
 1222 the above for all SM annihilation channels (17) and 25 sources (all \mathcal{LS} sources withing HAWC's
 1223 field of view) amounted to 127,925 jobs. In total, 1,407,175 likelihood fits and profiles would be
 1224 computed for the 11 mass bins we wished to study. The estimated CPU time ranged between 10k
 1225 CPU days - 8k CPU days. Human time is more challenging to estimate as job allocation is stochastic
 1226 and highly dependant on what other users are submitting, yet it is unlikely that all jobs would run
 1227 simultaneously. Therefore we can expect human time to be about as long as was seen in chapter 6
 1228 which was on the order of months to fully compute on a smaller analysis. A visual aid to describe
 1229 how jobs were organized is provided in Figure 7.4.

Name	Distance (kpc)	l, b ($^{\circ}$)	$\log_{10} J$ (\mathcal{LS} set) $\log_{10}(\text{GeV}^2\text{cm}^{-5}\text{sr})$
Coma Berenices	44	241.89, 83.61	$19.00^{+0.36}_{-0.35}$
Draco	76	86.37, 34.72	$18.83^{+0.12}_{-0.12}$
Segue I	23	220.48, 50.43	$19.12^{+0.49}_{-0.58}$
Sextans	86	243.50, 42.27	$17.73^{+0.13}_{-0.12}$

Table 7.1 Summary of the relevant properties of the dSphs used in the present work. Column 1 lists the dSphs. Columns 2 and 3 present their heliocentric distance and galactic coordinates, respectively. Column 4 reports the J -factors of each source given from the \mathcal{LS} studies and estimated $\pm 1\sigma$ uncertainties. The values $\log_{10} J$ (\mathcal{LS} set) [65] correspond to the mean J -factor values for a source extension truncated at 0.5° .

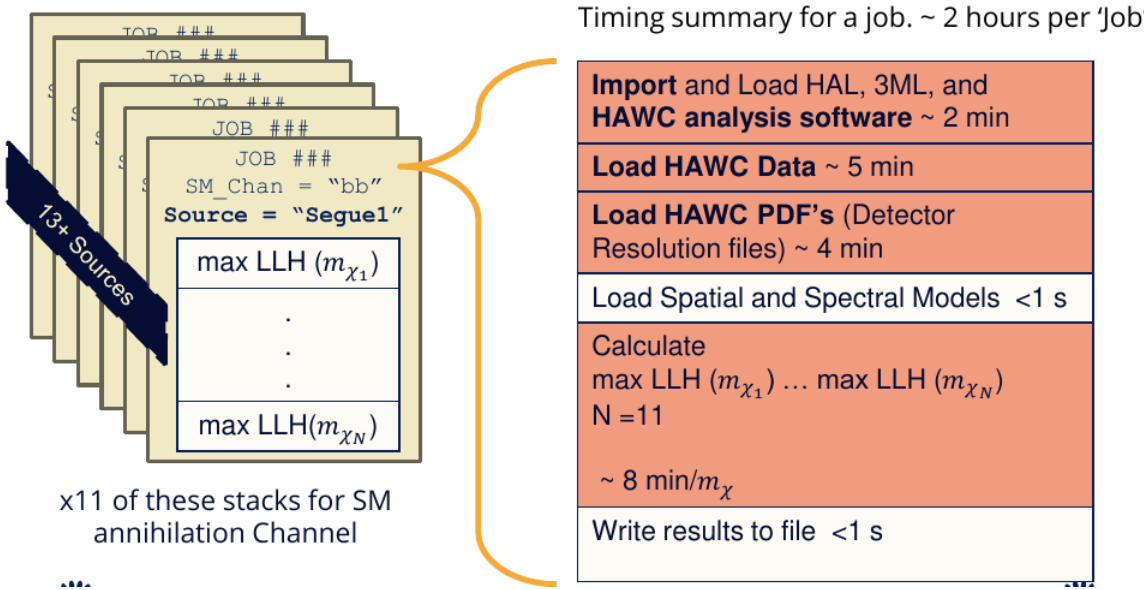


Figure 7.4 Infographic on how jobs and DM computation was organized in Section 6.3. Jobs were built for each permutation of CHANS and SOURCES shown by the left block in the figure. Each job, which took on the order 2 hrs to compute, had the following work flow: 1. Import HAWC analysis software, 2 min to run. 2. Load HAWC count maps, 5 min to run. 3. Load HAWC energy and spatial resolutions, 4 min. 5. Load DM spatial source templates and spectral models, less than 1 s. 6. Perform likelihood fit on data and model, about 8 min per DM mass. 7. Write results to file, less than 1s.

1230 The computational needs for this next generation DM analysis are extreme and is unlike other

1231 analyses performed on HAWC. It became clear that there was a lot to gain from optimzing how
1232 the likelihoods are computed. This section discusses how multi-threading was applied to solve and
1233 reduce HAWC's computing of likelihoods for large parameter spaces like in DM searches.

1234 7.5.1 Relevant Foundational Information

1235 The profiling of the likelihood for HAWC is done via gradient descent where the nomarilization

1236 of Equation (6.1) (linearly correlated with $\langle \sigma v \rangle$) is rescaled in the descent. Additionaly, we sample
1237 the likelihood space for a defined list of $\langle \sigma v \rangle$'s described in Section 6.4.2. The time to compute
1238 these values is not predictable or consistent because many variables can change across the full
1239 model-space. comprehensively, these variables are:

- 1240 • m_{χ} : DM rest mass

- 1241 • CHAN : DM SM annihilation channel.

1242 • SOURCE : dSph within HAWC's field of view. This involves a spatial template AND coordinate
1243 in HAWC data.

1244 • $\langle \sigma v \rangle$: Effectevly the flux normalization and free parameter in the likelihood fit.

1245 Therefore, we develop an asynchronous, functional-parallel coding pattern. Asynchronous meaning
1246 that the instructions and computing within a function are independent and permitted to be out of sync
1247 with sibling computations. Functional-parallel meaning that instructions are the subject of parral-
1248 lelization rather than threading the likelihood computation. This is close to trivial parametrization
1249 seen in Figure 7.4 except that we seek to consolidate the loading stages (software, data, and detector
1250 resolution loading). Reducing the total instances of loading stages and distributing access to the
1251 reduced loads across multiple asynchronous threads is expected to reduce serial processing time and
1252 the overhead implicit to each job in addition to saving human time.

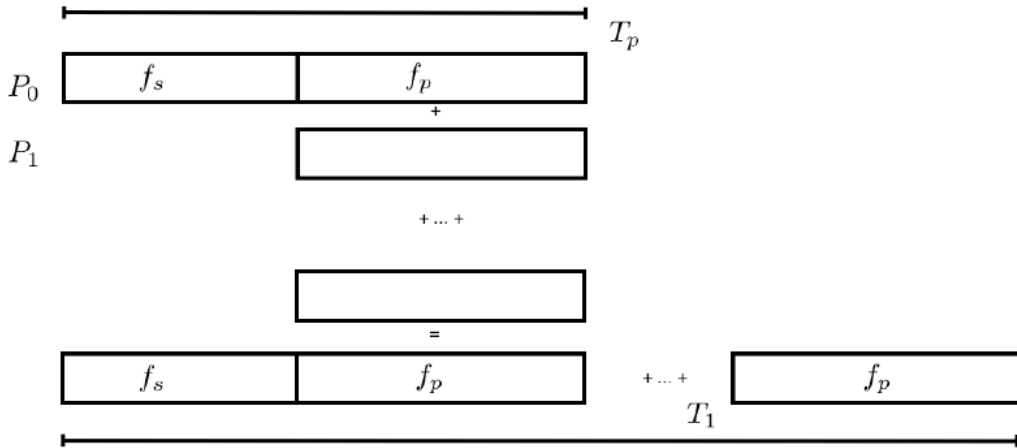


Figure 7.5 Graphic of Gustafson parallel coding pattern. f_s is the fraction of a program, in time, spent on serial computation. f_p is the fraction of computing time that is parallelizable. T_p is the total time for a parallel program to run. T_1 is the total time for a parallel program to run if only 1 processor is allocated. P_N is the N -th processor where it's row is the computation the processor performs. The Gustafson pattern is most similar to what is implemented for this analysis. Figure is pulled from [67].

1253 We need a way to measure and compare the expected speedup and efficiency gain for this
1254 asynchronous coding pattern. I pull inspiration for timing measurement from [67] and use *Amdahl's
1255 law with hybrid programming*. Hybrid programming meaning that the computation is a mix of

1256 distributed and shared memory programming. If we assume the code is fully parallelizable over p
1257 processors and c threads, the ideal speedup is simply pc and ideal run-time is $T_1/(pc)$. T_1 is the
1258 total time for a parallel program to run if only 1 processor is allocated. However, the coding pattern
1259 contains some amount of unavoidable serial computation, as shown in Figure 7.5. In our case, the
1260 run time is estimated to be

$$T_{p,c} = \frac{T_1}{pc} (1 + F_s(c - 1)). \quad (7.4)$$

1261 F_s is the fraction of CPU time dedicated to serial computation. The expected speedup is

$$S_{p,c} \equiv \frac{T_1}{T_{p,c}} = \frac{pc}{1 + F_s(c - 1)}. \quad (7.5)$$

1262 From Equation (7.5), we can see that the speed up scales with p/F_s . We are free to minimize
1263 F_s asymptotically by enlarging the total models that are submitted to the thread pool, thereby
1264 shrinking the CPU fraction dedicated to serial operation. We are also free to define exactly how
1265 many threads and processors we utilize, yet eventually hit a hard cap at the hardware available on
1266 our computing cluster. HAWC uses Intel Xeon processors with 48 cores and 96 threads. This
1267 means when N-threads (c) are defined, $N \bmod 2$ cores (p) are needed. We see that a successful
1268 code scales well as the expected speedup is inversely correlated with F_s . As the total number of
1269 models sampled grows, the speedup will also.

1270 7.5.2 Implementation

1271 The multithreaded code was written in Python3 and is documented in the `dark_matter_hawc`
1272 [repository](#) within the script named `mpu_analysis.py`. A version of the script as of April 25
1273 **TODO: make sure to update on this date** is also provided in Section B.1 It has many dependancies
1274 including the HAWC analysis software. Figure 7.6 displays the workflow of a job with 3 threads.
1275 Within a job, SOURCE is kept fixedh . CHAN(S) remains 17 elements long. More m_χ are sampled
1276 from 11 bins up to 49 (for $\gamma\gamma$ and ZZ) and 25 (for remaining CHANS) which amounts to 12 or 6
1277 mass bins per decade. The DM mass, m_χ , and SM annihilation channels, CHANS, are permuted into
1278 a 473 element list which is split evenly across N threads where N ranges between 5 - 16. Within a
1279 thread, for each m_χ -CHAN tuple, 1001 $\langle\sigma v\rangle$ values are sampled in the likelihood, and the value of

Timing summary for a multi-threaded job.

Import and Load HAL, 3ML, and HAWC analysis software ~ 2 min		
Load HAWC Data ~ 5 min		
Load HAWC PDF's (Detector Resolution files) ~ 4 min		
Load Spatial Model < 1s		
Load Spectra Models <1 s	Load Spectra Models <1 s	Load Spectra Models <1 s
Calculate max LLH (Chan_0, m_{χ_1}) ... max LLH (Chan_?, m_{χ_N}) N = TOTAL/N_THREADS ~ 8 min/Spec_model	Calculate max LLH (Chan_?, m_{χ_1}) ... max LLH (Chan_?, m_{χ_N}) N = TOTAL/N_THREADS ~ 8 min/Spec_model	Calculate max LLH (Chan_?, m_{χ_1}) ... max LLH (Chan_?, m_{χ_N}) N = TOTAL/N_THREADS ~ 8 min/Spec_model
Write results to file <1 s	Write results to file <1 s	Write results to file <1 s
Join Threads and terminate < 1s		

Figure 7.6 Task chart for one multi-threaded job developed for this project. Green blocks indicate a shared resource across the threads AND computation performed serially. Red blocks indicate functional parallel processing within each thread. 3 threads are represented here, yet many more can be employed during the full analysis. Jobs are defined by the SOURCE as these require unique maps to be loaded into the likelihood estimator. The m_{χ} , CHAN, and $\langle \sigma v \rangle$ variables are entered into the thread pool and allocated as evenly as possible across the threads.

1280 $\langle \sigma v \rangle$ that maximizes the likelihood is found. Although rare, fits that failed are handled on a case
1281 by case basis.

1282 7.5.3 Performance

M Tasks	$T_{p,c}$ (hr:min:s)			
	$T_{1,1}$	$T_{1,2}$	$T_{1,8}$	$T_{1,16}$
50	1:40:37.5	0:52:43.7	0:19:13.8	0:13:44.0
74	2:22:30.0	1:15::00.6	0:25:21.3	0:15:49.8
100	(3:07:51.9)		0:30:44.4	0:20:01.4
200	(6:02:20.6)	-		
473	(13:58:40.3)	-		1:09:42.9

Table 7.2 Timing summaries for analyses for serial and multithreaded processes. M tasks is the number of functional-parallel tasks ran for the computation. $T_{p,c}$ is a single run time in hours:minutes:seconds for runs utilizing p nodes and c threads. Runs are run interactively on the same computer to maximize consistency. Empty entries are indicated with '-'. (·) entries are estimated entries extrapolated from data earlier in the column.

1283 We see a tremendous reduction to human time waiting for our dSph analyses to run. Table 7.2

1284 shows the timing summaries for analyses of different sizes and thread counts. Additionally, the
 1285 efficiency gained when consolidating the serial loading of data is also apparent in our ability to
 1286 study many more tasks in about the same amount of wall time as a smaller serial computation. Trials
 1287 represented in the table were run on an AMD Opteron® processor 6344 with 48 cores, 2 threads
 1288 per core; 2.6 GHz clock. This is not the same architecture used for analysis on the computing
 1289 cluster however they are similar enough that results shown here are reasonably representative of
 1290 computing on the HAWC computing cluster. I use the Tab. 7.2 for the inferences and conclusions
 1291 in the following paragraphs.

1292 First, we want to find T_s , the time of serial computation. From Fig. 7.5, the timing for our
 1293 coding pattern can be written as

$$T_s + Mt_p = T_{1,1}^M. \quad (7.6)$$

1294 M is the number of functional-parallel tasks (represented as column 1 of Tab. 7.2), and t_p is the
 1295 average time to complete a single parallel task. $T_{1,1}^M$ is the total time for a parallel program to run if
 1296 only 1 processor is allocated for M parallel task. With two runs of different M ($M1$ and $M2$), we
 1297 can use a system of equations to derive

$$T_s = T_{1,1}^{M1} - M1 \left(\frac{T_{1,1}^{M1} - T_{1,1}^{M2}}{M1 - M2} \right). \quad (7.7)$$

1298 We also extract t_p using the same methods:

$$t_p = \frac{T_{1,1}^{M1} - T_{1,1}^{M2}}{M1 - M2}. \quad (7.8)$$

1299 From Tab. 7.2, we set $M1 = 50$ and $M2 = 74$ and take their corresponding $T_{1,1}$ from the table to
 1300 calculate T_s and t_p .

$$T_s = 803.1\text{s} \text{ and } t_p = 104.6\text{s} \quad (7.9)$$

1301 Now, we have specific estimation for the fraction of serial computing time, F_s :

$$F_s = \frac{803.1}{803.1 + 104.6 \cdot M}. \quad (7.10)$$

1302 The maximum M for this study is 473 which evaluates Eq. (7.10): $F_s = 0.016$ or 1.6% of computing
 1303 time. Table 7.3 shows the resulting speedups.

M Tasks	$S_{p,c}$		
	$S_{1,2}$	$S_{1,8}$	$T_{1,16}$
50	1.90 [1.76]	5.23 [4.14]	6.35 [5.34]
74	1.90 [1.83]	5.62 [4.82]	9.00 [6.64]
100			
200	-		
473	-		1:09:42.9

Table 7.3 Speed up summaries for analyses for serial and multithreaded processes. M tasks is the number of functional-parallel tasks ran for the computation. $S_{p,c}$ is a single speedup comparison for runs utilizing p nodes and c threads. $[\cdot]$ are the estimated speedups calculated from Tab. 7.2, Eq. (7.10), and Eq. (7.5). Empty entries are indicated with '-'.

1304 We see a speedup that exceeds expectations from Eq. (7.5) for real trail runs. **TODO: reflect**

1305 **on results when the tables are totally filled in.** We also see that there are diminishing returns as
 1306 the number of threads increases. For small jobs with large c , both the expected and observed
 1307 speedup are significantly smaller than c . One thing not considered in Eq. (7.5) is the time incurred
 1308 via communication latency. Communication latency increases with the number of threads and
 1309 contributes to diminishing returns. Therefor, these results are not conclusive. Each entry in
 1310 Tab. 7.2 represent only one run of the script and therefore the data are not precise and lacks the
 1311 full scope of timing costs. Yet, they do give us a good idea of what HAWC gains in multithreading
 1312 analysis software. We see very clearly that there is a lot to gain, and this new coding pattern will
 1313 expand HAWC's analysis capabilities.

1314 7.6 Analysis Results

1315 **TODO: talk about the results**

1316 We were not able to generate background trials in time of writing this thesis. These are not
 1317 shown and are an immediate next step for this analysis before publication.

1318 We did not see DM, but we did see some interesting excesses in the 10 Tev range at order 2σ .

1319 Draco was not included as the PDF of some of our analysis bins were wider than what is reasonable
 1320 for a point source analysis. Draco is at a high zenith for HAWC, so the effort required to include it
 1321 was not justified by the benefits.

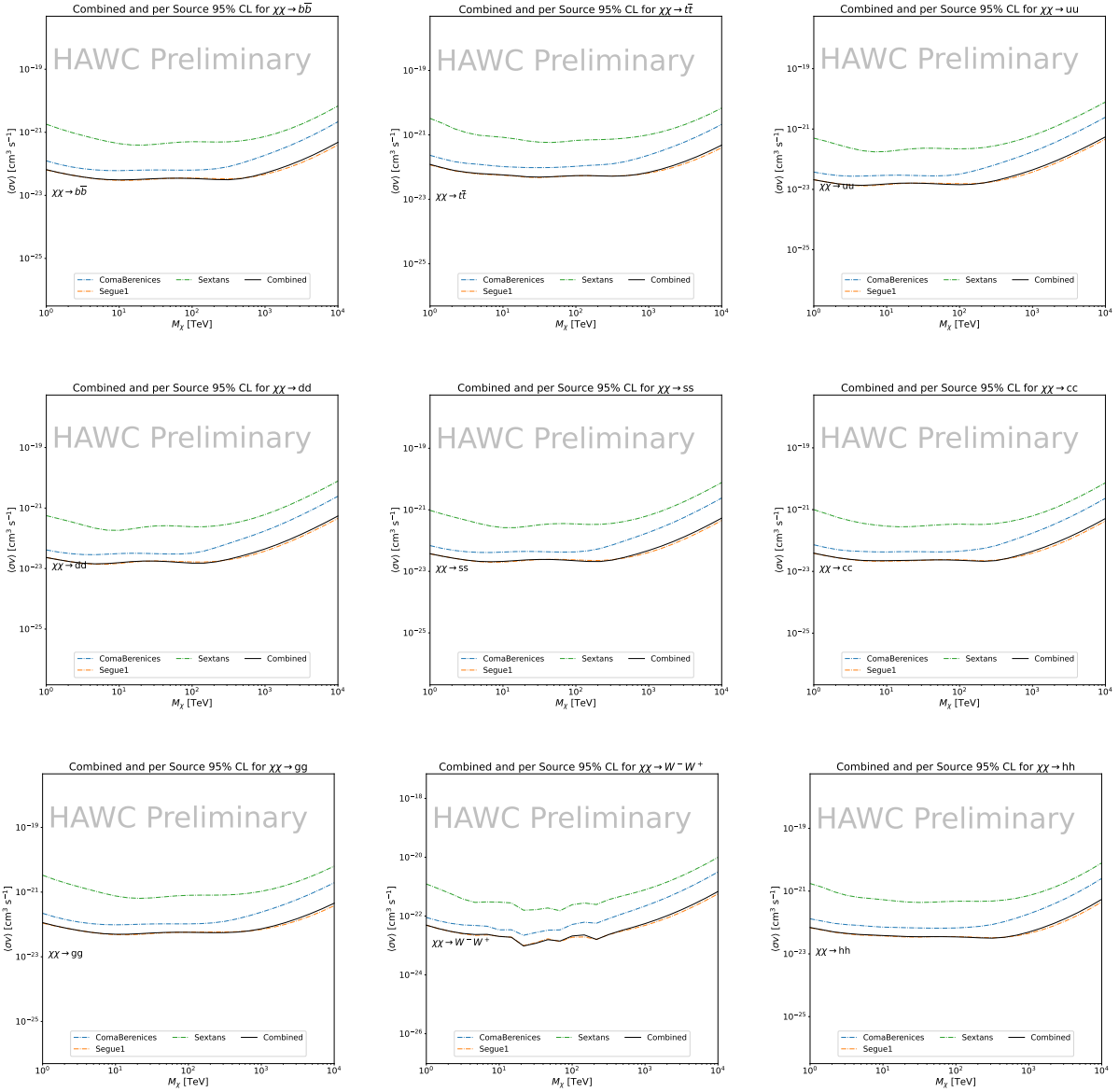


Figure 7.7 TODO: fill this out

1322 7.7 Systematics

1323 These are identical to what was performed earlier in Glory Duck, Section 6.7. We are also
 1324 sensitive to the choice in spatial template, and this was explored in Section 6.7.2 and Section 6.8.2.
 1325 \mathcal{LS} also provided the uncertainty on their mean spatial models. We perform a study on the
 1326 $\pm 1\sigma$ spatial templates and show corresponding confidence limits in TODO: link to figure

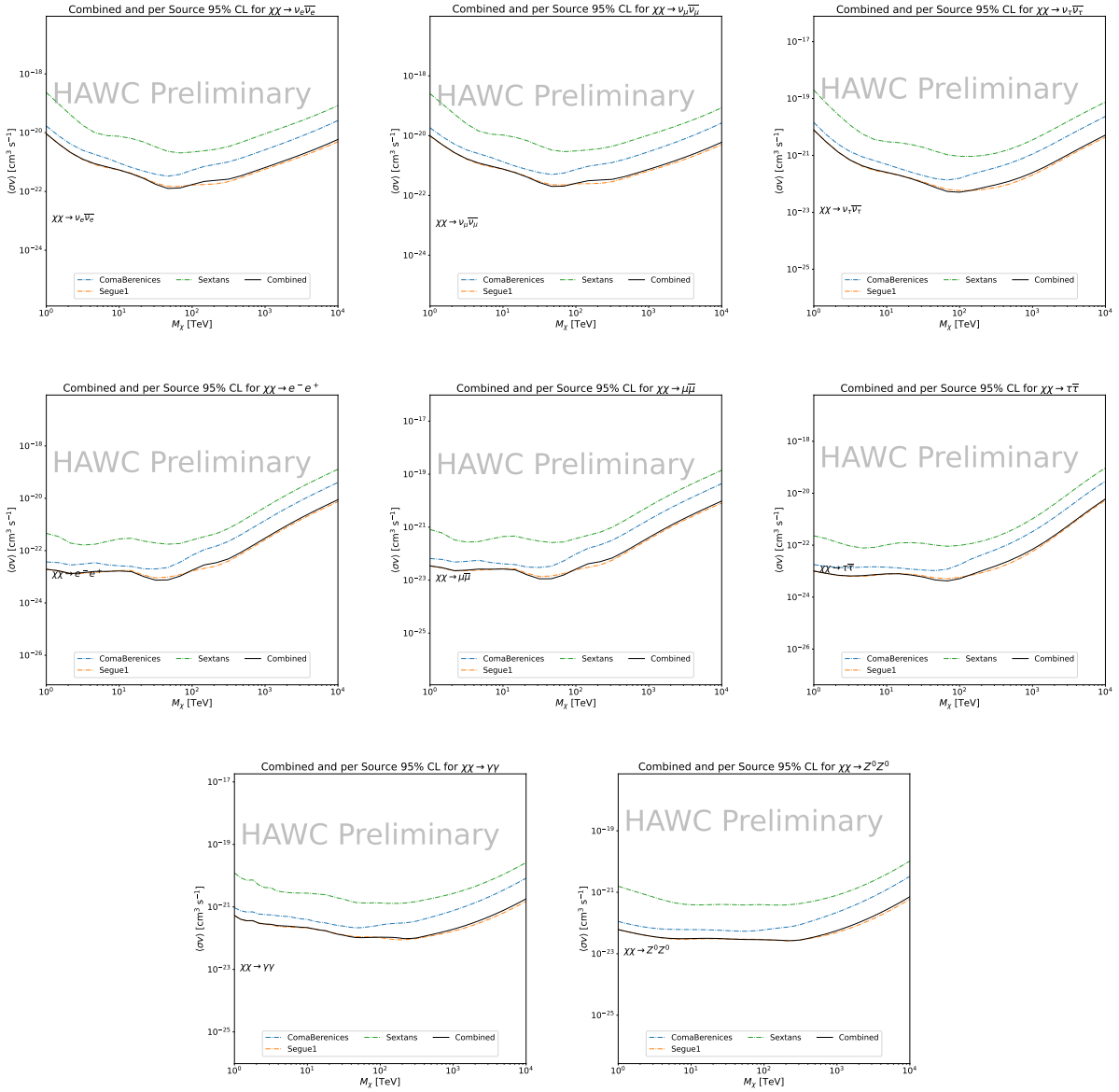


Figure 7.8 TODO: fill this out

1327 7.8 Conclusion and Discussion

1328 We want to include the remaining dSph and DM decay from the dSphs. We saw an improvement
 1329 of TODO: value compared to Glory Duck which had many more dSphs. TODO: copy some text
 1330 from earlier section.

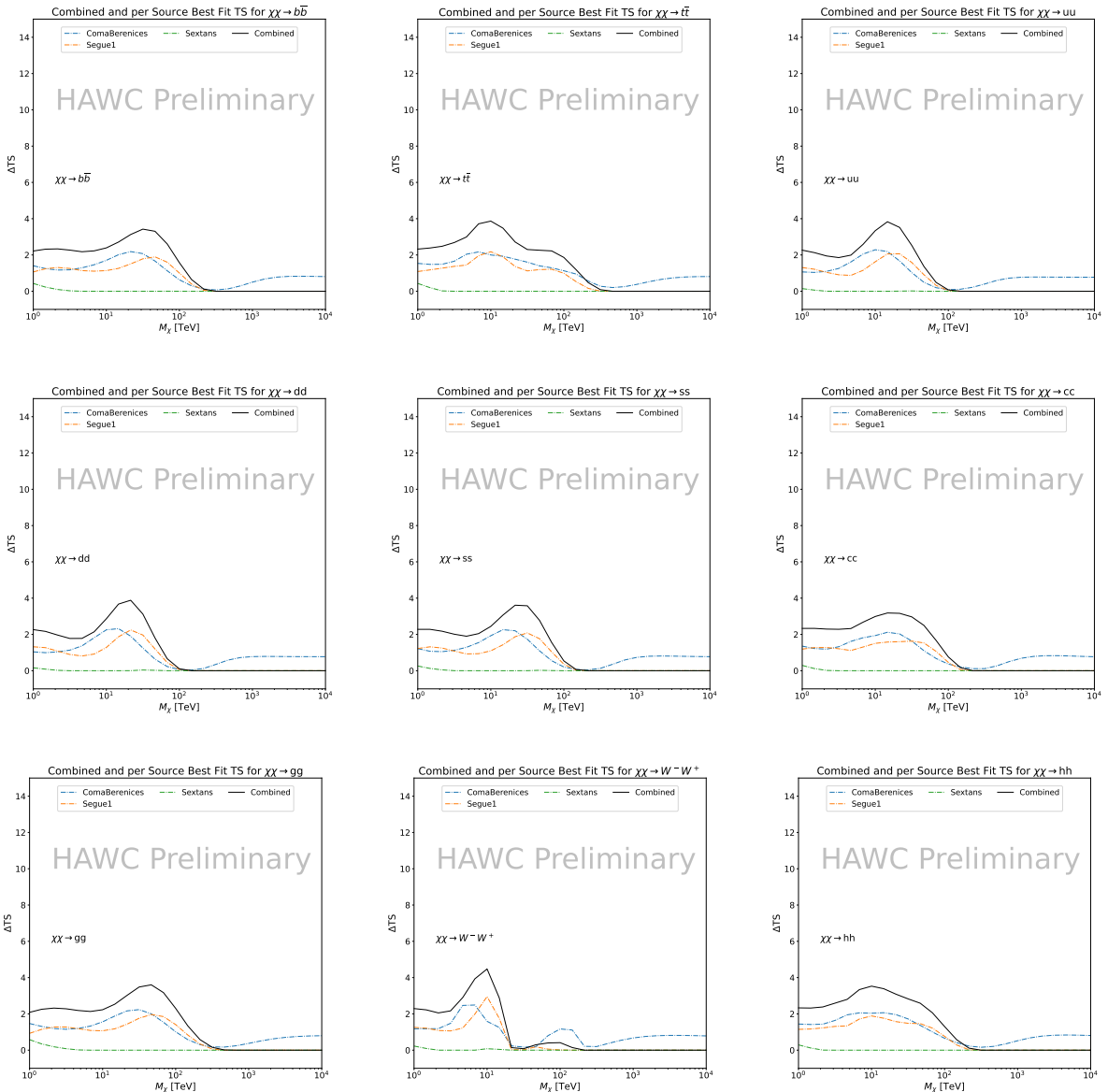


Figure 7.9 TODO: fill this out

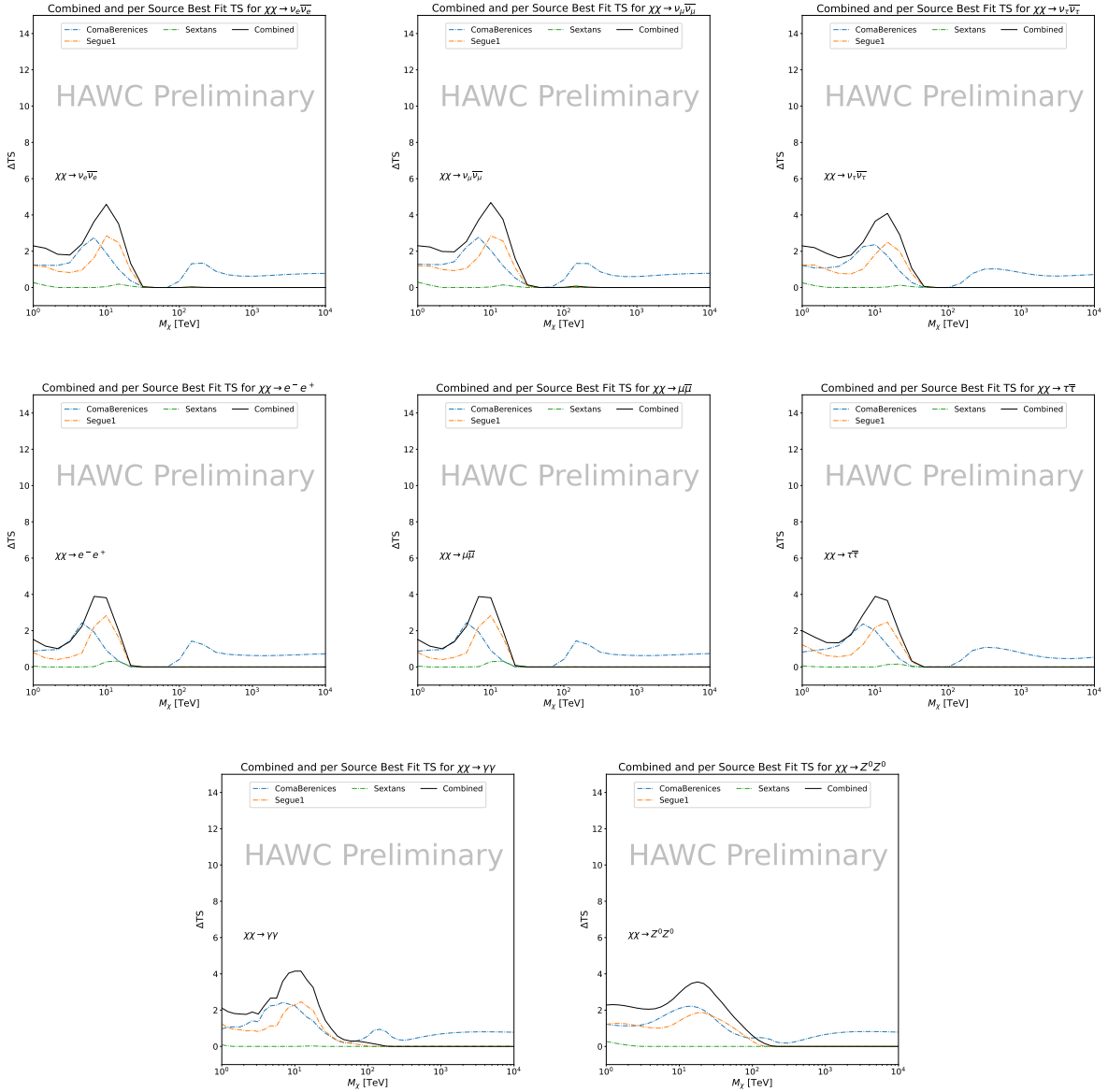


Figure 7.10 TODO: fill this out



Figure 7.11 TODO: Comparison of channels with GD combined results.[NEEDS A SOURCE][FACT CHECK THIS]

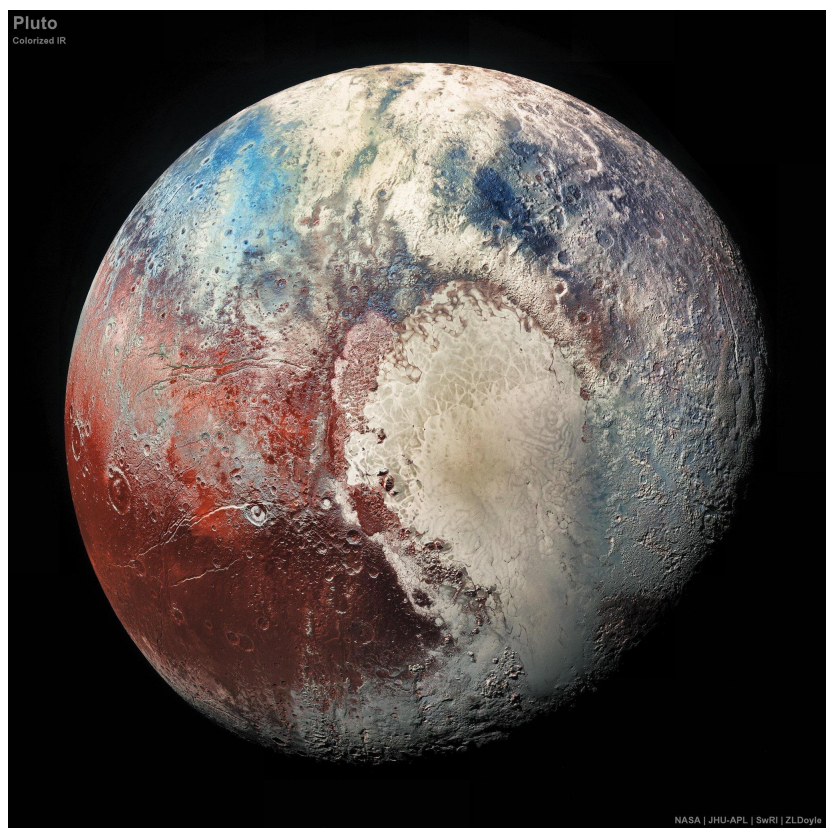


Figure 7.12 TODO: show p1 and m1 limits around[NEEDS A SOURCE][FACT CHECK THIS]



Figure 7.13 TODO: there will be 2[NEEDS A SOURCE][FACT CHECK THIS]

CHAPTER 8

**1331 HEAVY DARK MATTER ANNIHILATION SEARCH WITH ICECUBE'S NORTH SKY
1332 TRACK DATA**

1333

CHAPTER 9

NU DUCK

MULTI-EXPERIMENT SUPPLEMENTARY FIGURES

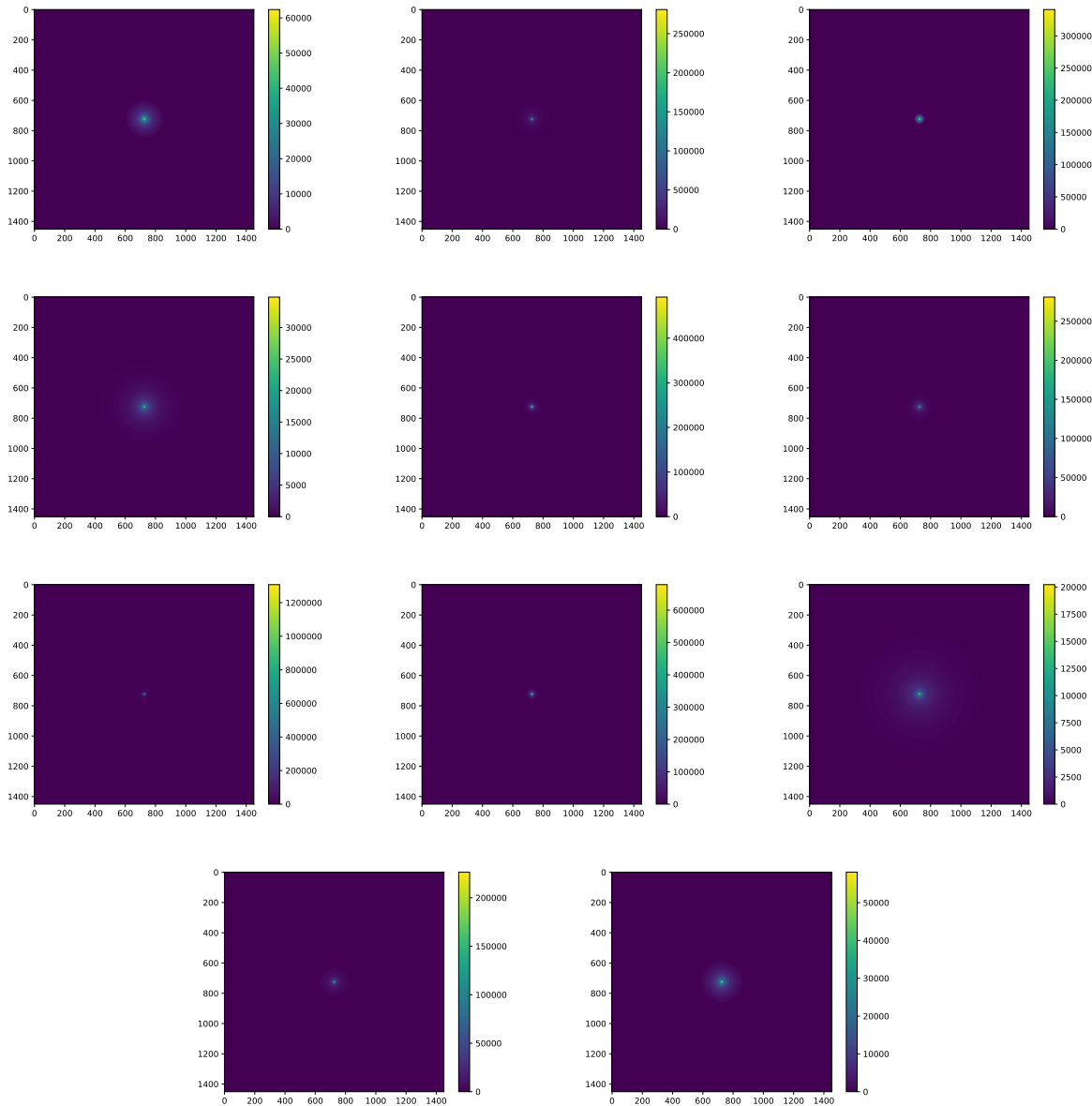


Figure A.1 Sister figure to Figure 6.3. Sources in the first row from left to right: Bootes I, Canes Venatici I, II. In second row: Draco, Hercules, Leo I. In the first row: Leo II, Leo IV, Sextans. In the final row: Ursa Major I, Ursa Major II.

APPENDIX B

1335

MULTITHREADING SUPPLEMENTARY FIGURES

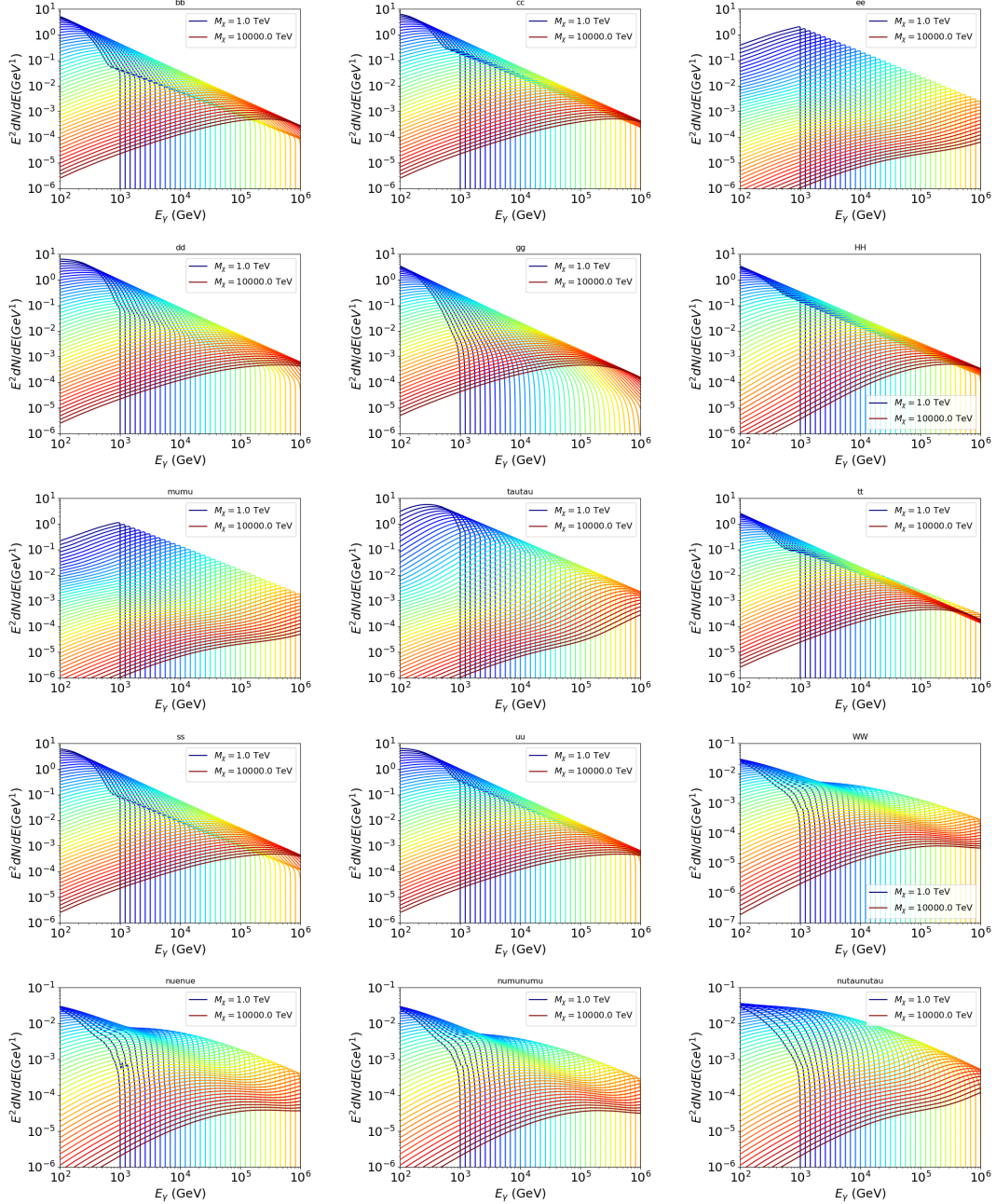


Figure B.1 Sister figure to Figure 7.2 for remaining SM primary annihilation channels studied for this thesis. These did not require any post generation smoothing and so are directly pulled from [64] with a binning scheme most helpful for a HAWC analysis.

1336 **B.1 mpu_analysis.py**

```
13371 import warnings
13382 with warnings.catch_warnings():
13393     warnings.simplefilter("ignore")
13404 # Python base libraries
13415 import os
13426 import sys
13437 import time
13448 # Import general libraries with namespace
13459 import matplotlib
13460 # Necessary for computing on cluster
13471 matplotlib.use("agg")
13482 import numpy as np
13493 import multiprocessing as mp
13504 # Import HAWC software
13515 sys.path.insert(1, os.path.join(os.environ['HOME'], 'hawc_software', 'threeML-
1352     analysis-scripts', 'fitModel'))
13536 from analysis_modules import *
13547 from threeML import *
13558 from hawc_hal import HAL, HealpixConeROI
13569 from threeML.minimizer.minimization import FitFailed
13570 # Import Dark Matter HAWC Libraries
13581 import analysis_utils as au
13592 import spectra as spec
13603 import sources as srcs
13614
13625 #* READ ONLY PATHS This block will change eventually
13636 MASS_LIST = './plotting/studies/nd/masses.txt'
13647 CHAN_LIST = './plotting/studies/nd/chans.txt'
13658
13669 #* WRITE PATHS, default location is to scratch
13670 OUT_PATH = os.path.join(os.environ["SCRATCH"], os.environ["USER"], 'New_duck')
```

```

13681 print('Our out path is going to be {}'.format(OUT_PATH))
13692
13703 # Define parallel Function. Can also be run serially
13714 def some_mass_fit(sigVs, datalist, shape, dSph, jfactor, mass_chan,
13725                 progress=None, log_file='', queue=None, i_job=0):
13736
13747     if progress is None:
13758         progress = [0]
13769     else: # Create log files for each thread
13770         log_file = log_file.replace('.log', '_ThreadNo_')
13781         log_file = log_file + str(i_job) + ".log"
13792         sys.stdout = open(log_file, "w")
13803
13814     fits = []
13825
13836     try:
13847         for m_c in mass_chan:
13858             print(f'Mass chan tuple: {m_c}')
13869             mass = int(m_c[0])
13870             ch = m_c[1]
13881             # Build path to output files
13892             outPath = os.path.join(OUT_PATH, ch, dSph)
13903             au.ut.ensure_dir(outPath)
13914
13925             if progress[i_job] < 0:
13936                 # If the master gets a Keyboard interrupt, commit suicide.
13947                 break
13958
13969                 ### Start Model Building for DM mass and SM channel #####
13970                 spectrum = spec.DM_models.HDMSpectra()
13981                 spectrum.set_channel(ch)
13992
14003                 myDwarf = ExtendedSource(dSph, spatial_shape=shape,

```

```

14014                     spectral_shape=spectrum)
14025
14036             spectrum.J = jfactor * u.GeV**2 / u.cm**5
14047             spectrum.sigmav = 1e-24 * u.cm**3 / u.s
14058             spectrum.set_dm_mass(mass * u.GeV)
14069
14070             spectrum.sigmav.bounds = (1e-30, 1e-12)
14081             model = Model(myDwarf)
14092             ##### End model Building #####
14103
14114             jl = JointLikelihood(model, datalist, verbose=False)
14125
14136             try:
14147                 result, lhdf = jl.fit(compute_covariance=False)
14158                 ts = -2.* (jl.minus_log_like_profile(1e-30) - jl.
1416                 _current_minimum)
14179                 # Also profile the LLH vs sv
14180                 ll = jl.get_contours(spectrum.sigmav, sigVs[0],
14191                               sigVs[-1], len(sigVs),
14202                               progress=False, log=['False'])
14213
14224                 sigv_ll = au.ut.calc_95_from_profile(ll[0], ll[2])
14235                 # Write results to file
14246                 outFileLL = outPath+f"/LL_{dSph}_{ch}_mass{int(mass)}_GD.txt"
14257                 np.savetxt(outFileLL, (sigVs, ll[2]),
14268                               delimiter='\t', header='sigV\tLL\n')
14279
14280                 with open(outPath+f"/results_{dSph}_{ch}_mass{int(mass)}_GD.
1429 txt", "w") as results_file:
14301                     results_file.write("mDM [GeV]\tsigV_95\tsigV_B.F.\n")
14312
14323                     results_file.write("%i\t%.5E\t%.5E\t%.5E"%(mass, sigv_ll,
14334                                         ts, result.value[0]))

```

```

14345         # End write to file
14356     except FitFailed: # Don't kill all threads if a fit fails
14367         print("Fit failed. Go back and calculate this spectral model
1437         later")
14388             fits.append((ch, mass, -1, -1))
14399             with open(log_file+'.fail', 'w') as f_file:
14400                 f_file.write(f'{ch}, {mass}\n')
14411
14422                     progress[i_job] += 1
14433                     matplotlib.pyplot.close() # Prevent leaky memory
14444
14455                     fits.append((ch, mass, result.value[0], ts))
14466                     progress[i_job] += 1
14477                     matplotlib.pyplot.close()
14488     except KeyboardInterrupt:
14499             progress[i_job] = -1
14500
14511             fits = np.array(fits)
14522             if queue is None:
14533                 return fits
14544             else:
14555                 queue.put((i_job, fits))
14566
14577 def main(args):
14588     masses = np.loadtxt(MASS_LIST, dtype=int)
14599     chans = np.loadtxt(CHAN_LIST, delimiter=',', dtype=str)
14600     mass_chan = au.ut.permute_lists(chans, masses)
14611
14622     print(f"DM masses for this study are: {masses}")
14633     print(f"SM Channels for this study are XX -> {chans}")
14644     print(mass_chan)
14655
14666     # extract information from input argument

```

```

14677 dSph = args.dSph
14688 data_mngr = au.ut.Data_Selector('P5_NN_2D')
14699 dm_profile = srcts.Spatial_DM(args.catalog, dSph, args.sigma, args.decay)
14700
14711 ##### Extract Source Information #####
14722 if dm_profile.get_dec() < -22.0 or dm_profile.get_dec() > 62.0:
14733     raise ValueError("HAWC can't see this source D: Exitting now...")
14744
14755 print(f'{dSph} information')
14766 print(f'jfac: {dm_profile.get_factor()}\tRA: {dm_profile.get_ra()}\tDec: {dm_profile.get_dec()}\n')
14777
14798 shape = SpatialTemplate_2D(fits_file=dm_profile.get_src_fits())
14809 ##### Finish Extract Source Information #####
14810
14821 ##### LOAD HAWC DATA #####
14832 roi = HealpixConeROI(data_radius=2.0, model_radius=8.0,
14843                         ra=dm_profile.get_ra(), dec=dm_profile.get_dec())
14854 bins = choose_bins.analysis_bins(args, dec=dm_profile.get_dec())
14865
14876 hawc = HAL(dSph, data_mngr.get_datmap(), data_mngr.get_detres(), roi)
14887 hawc.set_active_measurements(bin_list=bins)
14898 datalist = DataList(hawc)
14909 ##### FINISH LOAD HAWC DATA #####
14910
14921 # set up SigV sampling. This sample is somewhat standardized
14932 sigVs = np.logspace(-28,-18, 1001, endpoint=True) # NOTE This will change
1494 with HDM
14953
14964 if args.n_threads == 1:
14975     # No need to start || programming just iterate over the masses
14986     kw_arg = dict(sigVs=sigVs, datalist=datalist, shape=shape, dSph=dSph,
14997                     jfactor=dm_profile.get_factor(), mass_chan=mass_chan,

```

```

15008                 log_file=args.log)
15019             some_mass_fit(**kw_arg)
15020         else:
15031             # I Really want to suppress TQMD output
15042             from tqdm import tqdm
15053             from functools import partialmethod
15064             tqdm.__init__ = partialmethod(tqdm.__init__, disable=True)
15075
15086             x = np.array_split(mass_chan, args.n_threads)
15097             n_jobs = len(x)
15108
15119             print("Thread jobs summary by mass and SM channel")
15120             for xi in x:
15131                 print(f'{xi}')
15142
15153             queue = mp.Queue()
15164             progress = mp.Array('i', np.zeros(n_jobs, dtype=int))
15175
15186             # Define task pool that will be split amongsts threads
15197             kw_args = [dict(sigVs=sigVs, datalist=datalist, shape=shape,
15208                             dSph=dSph, jfactor=dm_profile.get_factor(),
15219                             mass_chan=mass_chan, progress=progress,
15220                             queue=queue, i_job=i, log_file=args.log)
15231                 for i, mass_chan in enumerate(x)]
15242
15253             # Define each process
15264             procs = [mp.Process(target=some_mass_fit, kwargs=kw_args[i]) \
15275                 for i in range(n_jobs)]
15286
15297             ### Start MASTER Thread only code block ###
15308             # Begin running all child threads
15319             for proc in procs: proc.start()
15320

```

```

15331     try:
15342         # In this case, the master does nothing except monitor progress of
1535         the threads
15363         # In an ideal world, the master thread also does some computation.
15374         n_complete = np.sum(progress)
15385         while_count = 0
15396
15407         while n_complete < len(mass_chan):
15418
15429             if np.any(np.asarray(progress) < 0):
15430                 # This was no threads are stranded when killing the script
15441                 raise KeyboardInterrupt()
15452             if while_count%1000 == 0:
15463                 print(f"{np.sum(progress)} of {len(mass_chan)} finished")
15474
15485             n_complete = np.sum(progress)
15496             time.sleep(.25)
15507             while_count += 1
15518
15529         except KeyboardInterrupt:
15530             # signal to jobs that it's time to stop
15541                 for i in range(n_jobs):
15552                     progress[i] = -2
15563                     print('\nKeyboardInterrupt: terminating early.')
15574                 ### End MASTER Thread only code block ###
15585
15596                 fitss = [queue.get() for proc in procs]
15607                 print(fitss)
15618                 print(f'Thread statuses: {progress[:]}')
15629
15630                 # putting results in a file
15641
15652                 print("QUACK! All Done!")

```

```

15663
15674
15685 if __name__ == '__main__':
15696     import argparse
15707
15718     p = argparse.ArgumentParser(description="Run a DM annihilation analysis on
1572         a dwarf spheroidal for a specific SM channel for DM masses [1 TeV to 10
1573         PeV]")
15749
15750     # Dwarf spatial modeling arguements
15761     p.add_argument("-ds", "--dSph", type=str,
15772             help="dwarf spheroidal galaxy to be studied", required=
1578     True)
15793     p.add_argument("-cat", "--catalog", type=str, choices=['GS15', 'LS20'],
15804             default='LS20', help="source catalog used")
15815     p.add_argument("-sig", "--sigma", type=int, choices=[-1, 0, 1], default=0,
15826             help="Spatial model uncertainty. 0 corresponds to the
1583 median. +/-1 correspond to the +/-1sigma uncertainty respectively.")
15847
15858     # Arguements for the energy estimators
15869     p.add_argument("-e", "--estimator", type=str,
15870             choices=['P5_NHIT', 'P5_NN_2D'],
15881             default="P5_NN_2D", required=False,
15892             help="The energy estimator choice. Options are: P5_NHIT,
1590 P5_NN_2D. GP not supported (yet).")
15913     p.add_argument("--use-bins", default=None, nargs="*",
15924             help="Bins to use for the analysis", dest="use_bins")
15935     p.add_argument('--select_bins_by_energy', default=None, nargs="*",
15946             help="Does nothing. May fill in later once better
1595 understood")
15967     p.add_argument('--select_bins_by_fhit', default=None, nargs="*",
15978             help="Also does nothing see above")
15989     p.add_argument( '-ex', "--exclude", default=None, nargs="*",

```

```

15990         help="Exclude Bins", dest="exclude")

16001

16012 # Computing and logging arguements.

16023 p.add_argument('-nt', '--n_threads', type=int, default=1,
16034                         help='Maximum number of threads spawned by script. Default
1604                         is 4')

16055 p.add_argument('-log', '--log', type=str, required=True,
16066                         help='Name for log files. Especially needed for threads')

16077

16088 p.add_argument('--decay', action="store_true",
16099                         help='Set spectral DM hypothesis to decay')

16100

16111 args = p.parse_args()

16122 print(args.decay)

16133 if args.exclude is None: # default exclude bins 0 and 1
16144     args.exclude = ['B0C0Ea', 'B0C0Eb', 'B0C0Ec', 'B0C0Ed', 'B0C0Ee']

16155

16166 if args.decay: OUT_PATH += '_dec'
16177 else: OUT_PATH += '_ann'

16188

16199 OUT_PATH = OUT_PATH + '_' + args.catalog
16200 if args.sigma != 0: OUT_PATH += f'_{args.sigma}sig'

16211

16222 main(args)

```

BIBLIOGRAPHY

- 1624 [1] Anne M. Green. “Dark matter in astrophysics/cosmology”. In: *SciPost Phys. Lect.*
 1625 *Notes* (2022), p. 37. doi: [10.21468/SciPostPhysLectNotes.37](https://doi.org/10.21468/SciPostPhysLectNotes.37). URL: <https://scipost.org/10.21468/SciPostPhysLectNotes.37>.
- 1627 [2] Bing-Lin Young. “A survey of dark matter and related topics in cosmology”. In: *Frontiers*
 1628 *of Physics* 12 (Oct. 2016). doi: <https://doi.org/10.1007/s11467-016-0583-4>.
 1629 URL: <https://doi.org/10.1007/s11467-016-0583-4>.
- 1630 [3] Gianfranco Bertone, Dan Hooper, and Joseph Silk. “Particle dark matter: evidence,
 1631 candidates and constraints”. In: *Physics Reports* 405.5 (2005), pp. 279–390. ISSN:
 1632 0370-1573. doi: <https://doi.org/10.1016/j.physrep.2004.08.031>. URL:
 1633 <https://www.sciencedirect.com/science/article/pii/S0370157304003515>.
- 1634 [4] Gianfranco Bertone and Dan Hooper. “History of dark matter”. In: *Rev. Mod. Phys.*
 1635 90 (4 Aug. 2018), p. 045002. doi: [10.1103/RevModPhys.90.045002](https://doi.org/10.1103/RevModPhys.90.045002). URL: <https://link.aps.org/doi/10.1103/RevModPhys.90.045002>.
- 1637 [5] Fritz Zwicky. “The Redshift of Extragalactic Nebulae”. In: *Helvetica Physica Acta* 6.
 1638 (1933), pp. 110–127. doi: [10.5169/seals-110267](https://doi.org/10.5169/seals-110267).
- 1639 [6] Vera C. Rubin and Jr. Ford W. Kent. “Rotation of the Andromeda Nebula from a
 1640 Spectroscopic Survey of Emission Regions”. In: *ApJ* 159 (Feb. 1970), p. 379. doi:
 1641 [10.1086/150317](https://doi.org/10.1086/150317).
- 1642 [7] K. G. Begeman, A. H. Broeils, and R. H. Sanders. “Extended rotation curves of spiral galax-
 1643 ies: dark haloes and modified dynamics”. In: *Monthly Notices of the Royal Astronomical So-*
 1644 *ciety* 249.3 (Apr. 1991), pp. 523–537. ISSN: 0035-8711. doi: [10.1093/mnras/249.3.523](https://doi.org/10.1093/mnras/249.3.523).
 1645 eprint: <https://academic.oup.com/mnras/article-pdf/249/3/523/18160929/mnras249-0523.pdf>. URL: <https://doi.org/10.1093/mnras/249.3.523>.
- 1647 [8] *Different types of gravitational lenses*. website. Feb. 2004. URL: <https://esahubble.org/images/heic0404b/>.
- 1649 [9] Douglas Clowe et al. “A Direct Empirical Proof of the Existence of Dark Matter”. In: *apjl*
 1650 648.2 (Sept. 2006), pp. L109–L113. doi: [10.1086/508162](https://doi.org/10.1086/508162). arXiv: [astro-ph/0608407](https://arxiv.org/abs/astro-ph/0608407)
 1651 [*astro-ph*].
- 1652 [10] Planck Collaboration and N. et. al. Aghanim. “Planck 2018 results I. Overview and the
 1653 cosmological legacy of Planck”. In: *A&A* 641 (2020). doi: [10.1051/0004-6361/201833880](https://doi.org/10.1051/0004-6361/201833880). URL: <https://doi.org/10.1051/0004-6361/201833880>.
- 1655 [11] Wayne Hu. *Matter Density Animation*. web. 2024. URL: <http://background.uchicago.edu/~whu/animbut/anim2.html>.

- 1657 [12] Wenlong Yuan et al. “A First Look at Cepheids in a Type Ia Supernova Host with JWST”. in:
1658 *The Astrophysical Journal Letters* 940.1 (Nov. 2022). doi: [10.3847/2041-8213/ac9b27](https://doi.org/10.3847/2041-8213/ac9b27).
1659 URL: <https://dx.doi.org/10.3847/2041-8213/ac9b27>.
- 1660 [13] Wendy L. Freedman. “Measurements of the Hubble Constant: Tensions in Perspective”. In:
1661 *The Astrophysical Journal* 919.1 (Sept. 2021), p. 16. doi: [10.3847/1538-4357/ac0e95](https://doi.org/10.3847/1538-4357/ac0e95).
1662 URL: <https://dx.doi.org/10.3847/1538-4357/ac0e95>.
- 1663 [14] Jodi Cooley. “Dark Matter direct detection of classical WIMPs”. In: *SciPost Phys. Lect.
1664 Notes* (2022), p. 55. doi: [10.21468/SciPostPhysLectNotes.55](https://doi.org/10.21468/SciPostPhysLectNotes.55). URL: <https://scipost.org/10.21468/SciPostPhysLectNotes.55>.
- 1666 [15] “Search for new phenomena in events with an energetic jet and missing transverse momentum
1667 in pp collisions at $\sqrt{s} = 13$ TeV with the ATLAS detector”. In: *Phys. Rev. D* 103
1668 (11 July 2021), p. 112006. doi: [10.1103/PhysRevD.103.112006](https://doi.org/10.1103/PhysRevD.103.112006). URL: <https://link.aps.org/doi/10.1103/PhysRevD.103.112006>.
- 1670 [16] *Jetting into the dark side: a precision search for dark matter*. website. July 2020. URL:
1671 <https://atlas.cern/updates/briefing/precision-search-dark-matter>.
- 1672 [17] Celine Armand et. al. “Combined dark matter searches towards dwarf spheroidal galaxies
1673 with Fermi-LAT, HAWC, H.E.S.S., MAGIC, and VERITAS”. in: *Proceedings of Science*.
1674 Vol. 395. Mar. 2022. doi: <https://doi.org/10.22323/1.395.0528>.
- 1675 [18] Tracy R. Slatyer. “Les Houches Lectures on Indirect Detection of Dark Matter”. In: *SciPost
1676 Phys. Lect. Notes* (2022), p. 53. doi: [10.21468/SciPostPhysLectNotes.53](https://doi.org/10.21468/SciPostPhysLectNotes.53). URL:
1677 <https://scipost.org/10.21468/SciPostPhysLectNotes.53>.
- 1678 [19] Christian W Bauer, Nicholas L. Rodd, and Bryan R. Webber. “Dark matter spectra from
1679 the electroweak to the Planck scale”. In: *Journal of High Energy Physics* 2021.1029-8479
1680 (June 2021). doi: [https://doi.org/10.1007/JHEP06\(2021\)121](https://doi.org/10.1007/JHEP06(2021)121).
- 1681 [20] Riccardo Catena and Piero Ullio. “A novel determination of the local dark matter density”.
1682 In: *Journal of Cosmology and Astroparticle Physics* 2010.08 (Aug. 2010), p. 004. doi:
1683 [10.1088/1475-7516/2010/08/004](https://doi.org/10.1088/1475-7516/2010/08/004). URL: <https://dx.doi.org/10.1088/1475-7516/2010/08/004>.
- 1685 [21] B. P. Abbott et al. “Observation of Gravitational Waves from a Binary Black Hole Merger”.
1686 In: *Phys. Rev. Lett.* 116 (6 Feb. 2016), p. 061102. doi: [10.1103/PhysRevLett.116.061102](https://doi.org/10.1103/PhysRevLett.116.061102). URL: <https://link.aps.org/doi/10.1103/PhysRevLett.116.061102>.
- 1688 [22] R. Abbasi et. al. “Observation of high-energy neutrinos from the Galactic plane”. In: *Science*
1689 380.6652 (June 2023), pp. 1338–1343.

- 1690 [23] NASA Goddard Space Flight Center. *Fermi's 12-year view of the gamma-ray sky*. website.
1691 2022. URL: <https://svs.gsfc.nasa.gov/14090>.
- 1692 [24] Marco Cirelli et al. "PPPC 4 DM ID: a poor particle physicist cookbook for dark matter
1693 indirect detection". In: *Journal of Cosmology and Astroparticle Physics* 2011.03 (Mar.
1694 2011), p. 051. doi: [10.1088/1475-7516/2011/03/051](https://doi.org/10.1088/1475-7516/2011/03/051). URL: <https://dx.doi.org/10.1088/1475-7516/2011/03/051>.
- 1696 [25] Javier Rico. "Gamma-Ray Dark Matter Searches in Milky Way Satellites—A Comparative
1697 Review of Data Analysis Methods and Current Results". In: *Galaxies* 8.1 (Mar. 2020), p. 25.
1698 doi: [10.3390/galaxies8010025](https://doi.org/10.3390/galaxies8010025). arXiv: [2003.13482 \[astro-ph.HE\]](https://arxiv.org/abs/2003.13482).
- 1699 [26] W. B. Atwood et al. "The Large Area Telescope on the Fermi Gamma-Ray Space Telescope
1700 Mission". In: *apj* 697.2 (June 2009), pp. 1071–1102. doi: [10.1088/0004-637X/697/2/1071](https://doi.org/10.1088/0004-637X/697/2/1071). arXiv: [0902.1089 \[astro-ph.IM\]](https://arxiv.org/abs/0902.1089).
- 1702 [27] M. Ackermann et al. "Searching for Dark Matter Annihilation from Milky Way Dwarf
1703 Spheroidal Galaxies with Six Years of Fermi Large Area Telescope Data". In: *prl* 115.23,
1704 231301 (Dec. 2015), p. 231301. doi: [10.1103/PhysRevLett.115.231301](https://doi.org/10.1103/PhysRevLett.115.231301). arXiv:
1705 [1503.02641 \[astro-ph.HE\]](https://arxiv.org/abs/1503.02641).
- 1706 [28] Mattia Di Mauro, Martin Stref, and Francesca Calore. "Investigating the effect of Milky
1707 Way dwarf spheroidal galaxies extension on dark matter searches with Fermi-LAT data".
1708 In: *Phys. Rev. D* 106 (12 Dec. 2022), p. 123032. doi: [10.1103/PhysRevD.106.123032](https://doi.org/10.1103/PhysRevD.106.123032).
1709 URL: <https://link.aps.org/doi/10.1103/PhysRevD.106.123032>.
- 1710 [29] F. et al. Aharonian. "Observations of the Crab Nebula with H.E.S.S.". In: *Astron. Astrophys.*
1711 457 (2006), pp. 899–915. doi: [10.1051/0004-6361:20065351](https://doi.org/10.1051/0004-6361:20065351). arXiv: [astro-ph/0607333](https://arxiv.org/abs/astro-ph/0607333).
- 1713 [30] J. Albert et al. "VHE γ -Ray Observation of the Crab Nebula and its Pulsar with the MAGIC
1714 Telescope". In: *The Astrophysical Journal* 674.2 (Feb. 2008), p. 1037. doi: [10.1086/525270](https://doi.org/10.1086/525270). URL: <https://dx.doi.org/10.1086/525270>.
- 1716 [31] N. Park. "Performance of the VERITAS experiment". In: *Proceedings, 34th International
1717 Cosmic Ray Conference (ICRC2015): The Hague, The Netherlands, July, 30th July - 6th
1718 August*. Vol. 34. 2015, p. 771. arXiv: [1508.07070 \[astro-ph.IM\]](https://arxiv.org/abs/1508.07070).
- 1719 [32] A. Abramowski et al. "H.E.S.S. constraints on Dark Matter annihilations towards the Sculptor
1720 and Carina Dwarf Galaxies". In: *Astropart. Phys.* 34 (2011), pp. 608–616. doi: [10.1016/j.astropartphys.2010.12.006](https://doi.org/10.1016/j.astropartphys.2010.12.006). arXiv: [1012.5602 \[astro-ph.HE\]](https://arxiv.org/abs/1012.5602).
- 1722 [33] A. Abramowski et al. "Search for dark matter annihilation signatures in H.E.S.S. observations
1723 of Dwarf Spheroidal Galaxies". In: *Phys. Rev. D* 90 (2014), p. 112012. doi: [10.1103/PhysRevD.90.112012](https://doi.org/10.1103/PhysRevD.90.112012). arXiv: [1410.2589 \[astro-ph.HE\]](https://arxiv.org/abs/1410.2589).

- 1725 [34] H. Abdalla et al. “Searches for gamma-ray lines and ‘pure WIMP’ spectra from Dark
1726 Matter annihilations in dwarf galaxies with H.E.S.S”. in: *JCAP* 11 (2018), p. 037. doi:
1727 [10.1088/1475-7516/2018/11/037](https://doi.org/10.1088/1475-7516/2018/11/037). arXiv: [1810.00995 \[astro-ph.HE\]](https://arxiv.org/abs/1810.00995).
- 1728 [35] J. Aleksić et al. “Optimized dark matter searches in deep observations of Segue 1 with
1729 MAGIC”. in: *JCAP* 1402 (2014), p. 008. doi: [10.1088/1475-7516/2014/02/008](https://doi.org/10.1088/1475-7516/2014/02/008).
1730 arXiv: [1312.1535 \[hep-ph\]](https://arxiv.org/abs/1312.1535).
- 1731 [36] V.A. Acciari et al. “Combined searches for dark matter in dwarf spheroidal galaxies observed
1732 with the MAGIC telescopes, including new data from Coma Berenices and Draco”. In: *Physics of the Dark Universe* (2021), p. 100912. issn: 2212-6864. doi: <https://doi.org/10.1016/j.dark.2021.100912>. URL: <https://www.sciencedirect.com/science/article/pii/S2212686421001370>.
- 1736 [37] M. L. Ahnen et al. “Indirect dark matter searches in the dwarf satellite galaxy Ursa Major II
1737 with the MAGIC Telescopes”. In: *JCAP* 1803.03 (2018), p. 009. doi: [10.1088/1475-7516/2018/03/009](https://doi.org/10.1088/1475-7516/2018/03/009). arXiv: [1712.03095 \[astro-ph.HE\]](https://arxiv.org/abs/1712.03095).
- 1739 [38] S. et al. Archambault. “Dark matter constraints from a joint analysis of dwarf Spheroidal
1740 galaxy observations with VERITAS”. in: *prd* 95.8 (Apr. 2017). doi: [10.1103/PhysRevD.95.082001](https://doi.org/10.1103/PhysRevD.95.082001). arXiv: [1703.04937 \[astro-ph.HE\]](https://arxiv.org/abs/1703.04937).
- 1742 [39] Louise Oakes et al. “Combined Dark Matter searches towards dwarf spheroidal galaxies with
1743 Fermi-LAT, HAWC, HESS, MAGIC and VERITAS”. in: *Proceedings of Science*. 2019.
- 1744 [40] Celine Armand et al. on behalf of the Fermi-LAT, HAWC, HESS, MAGIC, VERITAS.
1745 “Combined Dark Matter searches towards dwarf spheroidal galaxies with Fermi-LAT,
1746 HAWC, HESS, MAGIC and VERITAS”. in: *Proceedings of Science*. 2021.
- 1747 [41] Daniel Kerszberg et al. on behalf of the Fermi-LAT, HAWC, HESS, MAGIC, and VER-
1748 TIAS collaborations. “Search for dark matter annihilation with a combined analysis of
1749 dwarf spheroidal galaxies from Fermi-LAT, HAWC, H.E.S.S., MAGIC and VERITAS”. in:
1750 *Proceedings of Science*. 2023.
- 1751 [42] A. U. Abeysekara et al. “Observation of the Crab Nebula with the HAWC Gamma-Ray
1752 Observatory”. In: *The Astrophysical Journal* 843.1 (June 2017), p. 39. doi: [10.3847/1538-4357/aa7555](https://doi.org/10.3847/1538-4357/aa7555). URL: <https://doi.org/10.3847/1538-4357/aa7555>.
- 1754 [43] Giacomo Vianello et al. *The Multi-Mission Maximum Likelihood framework (3ML)*. 2015.
1755 arXiv: [1507.08343 \[astro-ph.HE\]](https://arxiv.org/abs/1507.08343).
- 1756 [44] Marco Cirelli et al. “PPPC 4 DM ID: a poor particle physicist cookbook for dark matter
1757 indirect detection”. In: *Journal of Cosmology and Astroparticle Physics* 2011.03 (Mar.
1758 2011). issn: 1475-7516. doi: [10.1088/1475-7516/2011/03/051](https://doi.org/10.1088/1475-7516/2011/03/051). URL: <http://dx.doi.org/10.1088/1475-7516/2011/03/051>.

- 1760 [45] Alex Geringer-Sameth, Savvas M. Koushiappas, and Matthew Walker. “DWARF GALAXY
1761 ANNIHILATION AND DECAY EMISSION PROFILES FOR DARK MATTER EXPERI-
1762 MENTS”. in: *The Astrophysical Journal* 801.2 (Mar. 2015), p. 74. ISSN: 1538-4357. doi:
1763 [10.1088/0004-637x/801/2/74](https://doi.org/10.1088/0004-637x/801/2/74). URL: <http://dx.doi.org/10.1088/0004-637X/801/2/74>.
- 1765 [46] A. Albert et al. “Dark Matter Limits from Dwarf Spheroidal Galaxies with the HAWC
1766 Gamma-Ray Observatory”. In: *The Astrophysical Journal* 853.2 (Feb. 2018), p. 154. ISSN:
1767 1538-4357. doi: [10.3847/1538-4357/aaa6d8](https://doi.org/10.3847/1538-4357/aaa6d8). URL: <http://dx.doi.org/10.3847/1538-4357/aaa6d8>.
- 1769 [47] V. Bonnivard et al. “Spherical Jeans analysis for dark matter indirect detection in dwarf
1770 spheroidal galaxies - Impact of physical parameters and triaxiality”. In: *Mon. Not. Roy.
1771 Astron. Soc.* 446 (2015), pp. 3002–3021. doi: [10.1093/mnras/stu2296](https://doi.org/10.1093/mnras/stu2296). arXiv:
1772 [1407.7822 \[astro-ph.HE\]](https://arxiv.org/abs/1407.7822).
- 1773 [48] M. Ackermann et al. “Searching for Dark Matter Annihilation from Milky Way Dwarf
1774 Spheroidal Galaxies with Six Years of Fermi Large Area Telescope Data”. In: *prl* 115.23,
1775 231301 (Dec. 2015), p. 231301. doi: [10.1103/PhysRevLett.115.231301](https://doi.org/10.1103/PhysRevLett.115.231301). arXiv:
1776 [1503.02641 \[astro-ph.HE\]](https://arxiv.org/abs/1503.02641).
- 1777 [49] M. L. Ahnen et al. “Limits to Dark Matter Annihilation Cross-Section from a Combined
1778 Analysis of MAGIC and Fermi-LAT Observations of Dwarf Satellite Galaxies”. In: *JCAP*
1779 1602.02 (2016), p. 039. doi: [10.1088/1475-7516/2016/02/039](https://doi.org/10.1088/1475-7516/2016/02/039). arXiv: [1601.06590](https://arxiv.org/abs/1601.06590)
1780 [astro-ph.HE].
- 1781 [50] Javier Rico et al. *gLike: numerical maximization of heterogeneous joint
1782 likelihood functions of a common free parameter plus nuisance parameters*.
1783 <https://doi.org/10.5281/zenodo.4601451>. Version v00.09.03. Mar. 2021. doi: [10.5281/zenodo.4601451](https://doi.org/10.5281/zenodo.4601451). URL: <https://doi.org/10.5281/zenodo.4601451>.
- 1785 [51] Tjark Miener and Daniel Nieto. *LklCom: Combining likelihoods from different experiments*.
1786 <https://doi.org/10.5281/zenodo.4597500>. Version v0.5.3. Mar. 2021. doi: [10.5281/zenodo.4597500](https://doi.org/10.5281/zenodo.4597500). URL: <https://doi.org/10.5281/zenodo.4597500>.
- 1788 [52] T. Miener et al. “Open-source Analysis Tools for Multi-instrument Dark Matter Searches”.
1789 In: *arXiv e-prints*, arXiv:2112.01818 (Dec. 2021), arXiv:2112.01818. arXiv: [2112.01818](https://arxiv.org/abs/2112.01818)
1790 [astro-ph.IM].
- 1791 [53] Alex Geringer-Sameth and Matthew Koushiappas Savvas M. and Walker. “Dwarf galaxy
1792 annihilation and decay emission profiles for dark matter experiments”. In: *Astrophys.
1793 J.* 801.2 (2015), p. 74. doi: [10.1088/0004-637X/801/2/74](https://doi.org/10.1088/0004-637X/801/2/74). arXiv: [1408.0002](https://arxiv.org/abs/1408.0002)
1794 [astro-ph.CO].

- 1795 [54] Gianfranco Bertone, Dan Hooper, and Joseph Silk. “Particle dark matter: evidence, can-
1796 didates and constraints”. In: *Physics Reports* 405.5-6 (Jan. 2005), pp. 279–390. ISSN:
1797 0370-1573. doi: [10.1016/j.physrep.2004.08.031](https://doi.org/10.1016/j.physrep.2004.08.031). URL: <http://dx.doi.org/10.1016/j.physrep.2004.08.031>.
- 1799 [55] V. Bonnivard et al. “Dark matter annihilation and decay in dwarf spheroidal galaxies: The
1800 classical and ultrafaint dSphs”. In: *Mon. Not. Roy. Astron. Soc.* 453.1 (2015), pp. 849–867.
1801 doi: [10.1093/mnras/stv1601](https://doi.org/10.1093/mnras/stv1601). arXiv: [1504.02048 \[astro-ph.HE\]](https://arxiv.org/abs/1504.02048).
- 1802 [56] A. et al. Albert. “Searching for Dark Matter Annihilation in Recently Discovered Milky Way
1803 Satellites with Fermi-LAT”. in: *Astrophys. J.* 834.2 (2017), p. 110. doi: [10.3847/1538-4357/834/2/110](https://doi.org/10.3847/1538-4357/834/2/110). arXiv: [1611.03184 \[astro-ph.HE\]](https://arxiv.org/abs/1611.03184).
- 1805 [57] Mattia Di Mauro and Martin Wolfgang Winkler. “Multimessenger constraints on the dark
1806 matter interpretation of the Fermi-LAT Galactic Center excess”. In: *prd* 103.12, 123005
1807 (June 2021), p. 123005. doi: [10.1103/PhysRevD.103.123005](https://doi.org/10.1103/PhysRevD.103.123005). arXiv: [2101.11027 \[astro-ph.HE\]](https://arxiv.org/abs/2101.11027).
- 1809 [58] HongSheng Zhao. “Analytical models for galactic nuclei”. In: *Mon. Not. Roy. Astron. Soc.*
1810 278 (1996), pp. 488–496. doi: [10.1093/mnras/278.2.488](https://doi.org/10.1093/mnras/278.2.488). arXiv: [astro-ph/9509122 \[astro-ph\]](https://arxiv.org/abs/astro-ph/9509122).
- 1812 [59] H. C. Plummer. “On the Problem of Distribution in Globular Star Clusters: (Plate 8.)”
1813 In: *Monthly Notices of the Royal Astronomical Society* 71.5 (Mar. 1911), pp. 460–470.
1814 ISSN: 0035-8711. doi: [10.1093/mnras/71.5.460](https://doi.org/10.1093/mnras/71.5.460). eprint: <https://academic.oup.com/mnras/article-pdf/71/5/460/2937497/mnras71-0460.pdf>. URL:
1816 <https://doi.org/10.1093/mnras/71.5.460>.
- 1817 [60] Daniel R. Hunter. “Derivation of the anisotropy profile, constraints on the local velocity
1818 dispersion, and implications for direct detection”. In: *JCAP* 02 (2014), p. 023. doi:
1819 [10.1088/1475-7516/2014/02/023](https://doi.org/10.1088/1475-7516/2014/02/023). arXiv: [1311.0256 \[astro-ph.CO\]](https://arxiv.org/abs/1311.0256).
- 1820 [61] Barun Kumar Dhar and Liliya L. R. Williams. “Surface mass density of the Einasto family
1821 of dark matter haloes: are they Sersic-like?” In: *Mon. Not. Roy. Astron. Soc.* (2010). doi:
1822 [10.1111/j.1365-2966.2010.16446.x](https://doi.org/10.1111/j.1365-2966.2010.16446.x).
- 1823 [62] M. Baes and E. Van Hese. “Dynamical models with a general anisotropy profile”. In:
1824 *Astron. Astrophys.* 471 (2007), p. 419. doi: [10.1051/0004-6361:20077672](https://doi.org/10.1051/0004-6361:20077672). arXiv:
1825 [0705.4109 \[astro-ph\]](https://arxiv.org/abs/0705.4109).
- 1826 [63] Matthew G. Walker, Edward W. Olszewski, and Mario Mateo. “Bayesian analysis of re-
1827 solved stellar spectra: application to MMT/Hectochelle observations of the Draco dwarf
1828 spheroidal”. In: *mnras* 448.3 (Apr. 2015), pp. 2717–2732. doi: [10.1093/mnras/stv099](https://doi.org/10.1093/mnras/stv099).
1829 arXiv: [1503.02589 \[astro-ph.GA\]](https://arxiv.org/abs/1503.02589).

- 1830 [64] Nicholas L. Rodd et al. “Dark matter spectra from the electroweak to the Planck scale”. In:
1831 *J. High Energy Physics* 121.10.1007 (June 2021).
- 1832 [65] Pace, Andrew B and Strigari, Louis E. “Scaling relations for dark matter annihilation and
1833 decay profiles in dwarf spheroidal galaxies”. In: *Monthly Notices of the Royal Astronomical
1834 Society* 482.3 (Oct. 2018), pp. 3480–3496. ISSN: 0035-8711. doi: [10.1093/mnras/sty2839](https://doi.org/10.1093/mnras/sty2839).
- 1836 [66] Albert, A. et al. “Search for gamma-ray spectral lines from dark matter annihilation in
1837 dwarf galaxies with the High-Altitude Water Cherenkov observatory”. In: *Phys. Rev. D* 101 (10 May 2020), p. 103001. doi: [10.1103/PhysRevD.101.103001](https://doi.org/10.1103/PhysRevD.101.103001). URL:
1839 <https://link.aps.org/doi/10.1103/PhysRevD.101.103001>.
- 1840 [67] Victor Eijkhout and Edmund Show and Robert van de Geijn. *The Science of Computing.
1841 The Art of High Performance Computing*. Vol. 3. Open Copy published under CC-BY 4.0
1842 license, 2023, pp. 63–66.